

**ANALYSIS, DESIGN AND DEVELOPMENT
OF ENERGY STORAGE SYSTEM FOR
ELECTRIC VEHICLES**

A Thesis Submitted

**In Partial Fulfillment of the Requirements
for the Degree of**

DOCTOR OF PHILOSOPHY

by

DEEPAK KUMAR
(Roll No. 2K21/PHDEE/509)



Under the Supervision of

Prof. M. Rizwan
Professor
DTU, Delhi

Dr. Amrish K. Panwar
Associate Professor
DTU, Delhi

Department of Electrical Engineering
DELHI TECHNOLOGICAL UNIVERSITY
(Formerly Delhi College of Engineering)
Shahbad Daulatpur, Main Bawana Road, Delhi-110042, India

April, 2026

ACKNOWLEDGEMENTS

First and foremost, I sincerely acknowledge my most sincere gratitude to my supervisors, Prof. M. Rizwan and Dr. Amrish K. Panwar, for their valuable guidance, support, and motivation during this research work. They have been outstanding mentors, and working with them has been a remarkable experience. The valuable hours of discussion, I had with them undoubtedly helped to supplement my thoughts in the right direction for attaining the desired objectives. I consider it my proud privilege to have worked with them, ever ready to lend a helping hand. I am forever thankful to them for all their wise words and inspiring thoughts.

I am also grateful to my Head of Department, Prof. Rachana Garg, Prof. Madhusudan Singh (Former Registrar, DTU), and all faculty members for their moral support in completing this thesis. Additionally, I would like to thank the CoE for EVRT in the Department of Electrical Engineering, and Lithium-Ion Battery Technology Research Laboratory in the Department of Applied Physics at Delhi Technological University for providing the necessary facilities within the department to support my research work.

I extend my thanks to my seniors and colleagues, especially Dr. Astitva Kumar, Dr. Bilal, Dr. Rahma Aman, Dr. Mrityunjay Kumar Singh, Dr. Prateek Sharma, Dr. Abhishek Bhardwaj, Dr. Mukesh K. Sahu, Dr. Abdul Azeem, Mr. Ganesh Kumar, Dr. Meghana Shrivastava, Ms Arpana Singh, Ms Apoorva Choumal, Ms Urmila Sheron, and LIBT Lab colleagues for their constant motivation and for reminding me to complete my work at the earliest.

The assistance of the valuable staff in the Renewable Energy Research Facility of Delhi Technological University is gratefully acknowledged. I am especially thankful to Mr Vickey Kumar Prasad and Mr Ankit Kumar for their substantial assistance during my research.

I would like to take this opportunity to express my heartfelt gratitude to my parents, Shri Diwakar Prasad and Smt. Radhika Devi and my grandparents, for everything they have done and continue to do for me. They never lost their faith in me and sacrificed a great deal in their lives to help me come this far. I am also deeply thankful to my siblings, Mr Rajoo Kumar (FTII), Ms Arti, Ms Rachana and Ms Neeloo, and Prof. Hari Prasad with

family, for being constant sources of support. Special thanks to my grandfather, Hari Nandan (Indian Army), for his unwavering support and blessings throughout my journey.

This acknowledgment would not be complete without mentioning my supervisors and seniors. They have been my core support system throughout this journey. Words cannot fully articulate my admiration for them. They provided unconditional support and continued to be constant sources of inspiration throughout my research journey. My heartfelt thanks to all those who supported me indirectly through their encouragement, care, and belief in me.

I am wholly indebted to the ALMIGHTY, who is omnipotent and the superpower of the universe.

Place: Delhi

(Deepak Kumar)

Date: 29.04.2026

CANDIDATE’S DECLARATION

I Deepak Kumar hereby certify that the work which is being presented in the thesis entitled “**Analysis, Design and Development of Energy Storage Systems for Electric Vehicles**” in partial fulfillment of the requirements for the award of the Degree of Doctor of Philosophy, submitted in the Department of Electrical Engineering, Delhi Technological University is an authentic record of my own work carried out during the period from 11.01.2022 to 30.03.2026 under supervision of Prof. M. Rizwan and Dr. Amrish K. Panwar. The matter presented in the thesis has not been submitted by me for the award of any other degree of this or any other Institute.

Place: Delhi

(Deepak Kumar)

Date: 29.04.2026

This is to certify that the student has incorporated all the corrections suggested by the examiners in the thesis, and the statement made by the candidate is correct to the best of our knowledge.

Signature of Supervisor(s)

Signature of External Examiner

CERTIFICATE BY THE SUPERVISOR(s)

Certified that **Deepak Kumar** (2K21/PhDEE/509) has carried out his research work presented in this thesis entitled “**Analysis, Design and Development of Energy Storage System for Electric Vehicles**” for the award of Doctor of Philosophy from the Department of Electrical Engineering, Delhi Technological University, Delhi, under our supervision. The thesis embodies results of original work, and studies are carried out by the student himself, and the contents of the thesis do not form the basis for the award of any other degree to the candidate or to anybody else from this or any other University/Institution.

(Prof. M. Rizwan)

Supervisor

Department of Electrical Engineering

Delhi Technological University

Delhi, India

(Dr. Amrish K. Panwar)

Co-Supervisor

Department of Applied Physics

Delhi Technological University

Delhi, India

Date: 29.04.2026

ABSTRACT

The rapid adoption of electric vehicles requires the development of energy storage systems with high energy density, enhanced safety, and long cycle life. However, the performance of lithium-ion batteries in electric vehicle applications is significantly influenced by operating and environmental conditions, including material degradation, temperature variations, charge/discharge rates, dynamic drive profiles, and thermal stresses. These factors introduce nonlinear electrochemical behaviour that accelerates battery aging and hinders the accurate estimation of critical battery states, such as state of charge, state of energy, and state of health.

To address these challenges, this thesis aims to develop advanced artificial intelligence-driven frameworks combining advanced cathode material development, AI-based state estimation, and Green AI-based control strategies. to address the challenges of nonlinear battery behaviour, ageing, and safety. The proposed approach significantly improves the accuracy, reliability and sustainability of lithium-ion battery systems in electric vehicle applications.

A Ni-rich layered NMC811 cathode was synthesised through a solid-state reaction route and characterized through thermogravimetric analysis, Fourier transform infrared spectroscopy, X-ray diffraction, scanning electron microscopy and energy dispersive x-ray spectroscopy analysis. These results confirmed a hexagonal α -NaFeO₂ phase (R-3m space group), crystallite size \sim 22 nm. Thermal and structural analyses confirmed phase formation, while scanning electron microscopy and energy dispersive x-ray spectroscopy revealed homogeneous morphology and elemental composition, validating its suitability for high-energy-density EV batteries.

To address battery monitoring challenges, advanced AI-based algorithms were developed for accurate estimation of state of charge and state of energy. A novel filtering technique was proposed to reduce redundant data by maintaining original critical patterns. The method achieved up to 80% reduction in dataset size, and 79-80% memory consumption, 59-66% computational efficiency, and 61-82% energy consumption without losing critical lithium-ion battery dynamic information. The filter technique with convolutional neural network and bidirectional long short-term memory model achieved significantly higher

estimation accuracy compared to traditional models for battery states estimation under different dynamic drive cycles, improving RMSE, MSE, and MAE by up to 99.98%, 99.97%, and 99.96%, respectively. However, the filter technique with gated recurrent unit model improved state of health estimation accuracy by over 93% in RMSE and maintained R^2 values above 0.999 across multiple aging datasets. These findings validate the proposed energy efficient AI frameworks for battery health monitoring. This research introduces a Green AI framework for accurate, scalable, and efficient battery state estimation and health monitoring under dynamic conditions.

Further, the impact of the environmental and operational influences, such as temperature variations and dynamic load profiles, was systematically investigated. Condition-aware AI-driven control strategies were developed for adaptive charging behaviour, thermal management, and degradation mitigation. The proposed models were tested across $-10\text{ }^{\circ}\text{C}$ to $40\text{ }^{\circ}\text{C}$, confirmed by the convolutional neural network, which achieved superior accuracy i.e. RMSE of 0.0043 and 67% faster computation, while long short-term memory performed best at $25\text{--}40\text{ }^{\circ}\text{C}$ and showed higher error at $-10\text{ }^{\circ}\text{C}$ due to electrochemical limitations. CNN based SOH and SOC estimation frameworks outperform long short-term memory and gated recurrent unit in terms of accuracy, flexibility, and efficiency under diverse thermal conditions.

This interdisciplinary research contributes a unified framework that integrates materials engineering, Green AI-driven modelling, condition-aware architecture and sustainable computational techniques. The proposed methodology significantly improves battery states prediction accuracy, computational efficiency, and operational reliability. The outcomes of this research deliver strong foundation for the development of intelligent, energy-efficient, condition-aware BMS for the next generation of electric mobility and energy storage applications. Furthermore, the incorporation of Green AI principles ensures reduction in computational and energy demands, improved resource efficiency. This development supports sustainable and energy-efficient energy storage technologies for greener EVs aligned with global decarbonization goals.

LIST OF PUBLICATION

- **List of papers (s) published in Peer Reviewed Referred International Journals**
 1. D. Kumar, M. Rizwan, and A. K. Panwar, “Towards Green AI: A Novel Hybrid Filter Based AI Approach for Energy-Efficient State of Charge and Energy Estimation in Li-Ion Batteries Under Various Drive Cycles,” *IEEE Trans Ind Appl*, vol. 61, no. 5, pp. 7633–7645, 2025, doi: 10.1109/TIA.2025.3550108. IF- 4.5, (SCIE-Q1)
 2. D. Kumar, M. Rizwan, and A. K. Panwar, “Advanced Intelligent approach for state of charge estimation of lithium-ion battery,” *Energy Sources, Part A: Recovery, Utilization, and Environmental Effects*, vol. 45, no. 4, pp. 10661–10681, Oct. 2023, doi: 10.1080/15567036.2023.2249427. IF- 2.4, (SCIE-Q1)
 3. D. Kumar, M. Rizwan, and A. K. Panwar, “Recent Advancements, Challenges, and Future Directions of Lithium-Sulfur Battery,” *Ionic*, pp. 1–24, Feb. 2026, doi: 10.1007/s11581-026-06993-3. IF. 2.6 (SCIE-Q2)
 4. D. Kumar, M. Rizwan, and A. K. Panwar, “Robust State Of Health Estimation Of Commercial Lithium-Ion Batteries Based on Enhanced Hybrid Machine Learning Model for Electrified Transportation,” *Electrical Engineering*, vol. 107, no. 4, pp. 5053–5070, Apr. 2025, <https://doi.org/10.1007/s00202-024-02808-8>. IF- 1.7, (SCIE-Q2)
- **List of Paper(s) Published in Peer Reviewed International Conference**
 1. D. Kumar, M. Rizwan, and A. K. Panwar, “Advanced Intelligent Hybrid Approach for State of Charge Estimation of Li-Ion Batteries in Electric Vehicles under Various Drive Cycles,” *2023 IEEE International Conference on Power Electronics, Smart Grid, and Renewable Energy (PESGRE-2023)*, pp. 1–6, Dec. 2023, doi: 10.1109/PESGRE58662.2023.10404810.
 2. M. Rizwan, D. Kumar, and A. K. Panwar, “New Filter-based Supervised Learning Approach for State of Charge Estimation of Li-Ion Battery for EV Applications,” *2023 International Conference on Modeling, Simulation & Intelligent Computing (MoSICom-2023)*, pp. 213–218, Dec. 2023, doi: 10.1109/MOSICOM59118.2023.10458745.

• **List of other publications**

1. D. Kumar, M. Ahmed, M. Jamil, M. Rizwan, and A. K. Panwar, "Towards Green AI: Energy-Efficient State of Health Estimation and Degradation Analysis of Commercial Lithium-Ion Batteries Based on Deep Learning and Filter Technique Approach," *IEEE Trans Ind Appl*, 2025, <https://doi.org/10.1109/TIA.2025.3604739>. IF- 4.5, (SCIE-Q1)
2. D. Kumar, R. Nasimov, A. Singh, A. Jha, A. Jha, and M. Rizwan, "Artificial Intelligence Approaches for SOH Estimation in Lithium-Ion Batteries: A Comprehensive Review of Progress, Critical Evaluations, Challenges, and Toward Future Outlooks," *Applied Computational Intelligence and Soft Computing*, vol. 2025, no. 1, p. 5516151, Jan. 2025, doi: 10.1155/ACIS/5516151. IF-2.9 (ESCI-Q1)
3. R. Nasimov, D. Kumar et al., "A Novel Approach for State of Health Estimation of Lithium-Ion Batteries Based on Improved PSO Neural Network Model," *Processes* 2024, vol. 12, no. 9, p. 1806, 2024, doi: 10.3390/PR12091806. IF- 2.8 (SCIE-Q2)
4. Amritanshu Jha, Anand Jha, Akshat Singh, D. Kumar, Prof. M. Rizwan, "EV Battery Thermal Management System Simulation Modelling and Analysis," 2nd International Conference on Sustainable Power and Energy Research (ICSPER), (11-12- July – 2025), (Accepted).
5. D. Kumar, A. K. Ranjan, H. Raj, A. Kumar, M. Rizwan, and S.A. Khan, "A Comprehensive Review on Thermal Runaway in Lithium-Ion Batteries: Triggers, Gas Emissions, and Safety Implications," 2nd International Conference on Sustainable Power and Energy Research (ICSPER), (11-12- July – 2025), (Accepted).
6. D. Kumar, H. Raj, A. Kumar, A. Ranjan, M. Rizwan, and A. K. Panwar, "Exploration of Range Estimation and Energy Consumption of Electric Vehicle for Different Real-Time Drive Modes," *IEEE 5th International Conference on Sustainable Energy and Future Electric Transportation (SEFET)*, (09 - 12 July-2025) <https://doi.org/10.1109/SEFET65155.2025.11254979>.
7. D. Kumar, H. Raj, A. Kumar, A. Kumar Ranjan, M. Rizwan, and A. K. Panwar, "Robust State of Charge Estimation of Lithium-Ion Batteries Based on Hybrid Deep Learning Approach," *Conference Record - IAS Annual Meeting (IEEE Industry Applications Society)*, 2025, doi: 10.1109/IAS62731.2025.11061708.

8. M. Ahmed, D. Kumar, and M. Jamil, “Deep Learning Based Modelling for Degradation Analysis and SOH Estimation of Commercial Lithium-Ion Batteries,” Proceedings of the 3rd IEEE International Conference on Power Electronics, Intelligent Control and Energy Systems, (ICPEICES-2024), pp. 1139–1144, 2024, doi: 10.1109/ICPEICES62430.2024.10719198.
9. D. Kumar, M. Rizwan, and A. K. Panwar, “A Mini Review on Recent Developments, Limitations, and Future Scenarios of Lithium-Sulfur Battery,” International Meeting on Energy Storage Devices 2023 (IMESD-2023) at Department of Physics, Indian Institute of Technology Roorkee, India during 07-10 December-2023.
10. D. Kumar, M. Rizwan, and A. K. Panwar, “Synthesis, Structural and Electrochemical Analysis of Li-rich NMC Cathode for Lithium-ion Batteries.” International Meeting on Energy Storage Devices 2023 (IMESD-2023) at the Department of Physics, Indian Institute of Technology Roorkee, India, during 07-10 December 2023.

LIST OF PATENTS

1. D. Kumar, A. K. Ranjan, M. Rizwan, M. Singh, and A. K. Panwar, “Design of a Thermal Runaway Chamber for Testing and Investigation of Hazardous Gases and Safety of Li-ion Batteries,” (2025), Application No. 202611009870
2. D. Kumar, M. Rizwan, and A. K. Panwar, “Energy-Efficient State of Health Estimation of Lithium-Ion Batteries Using Green AI and Data Filtering Technique,” (2025), Status: Application No. 202611050980
3. D. Kumar, M. Rizwan, and A. K. Panwar, “Method for Energy-Efficient State of Charge (SOC) and State of Energy (SOE) Estimation of Lithium-Ion Batteries based on Green Artificial Intelligence (Green-AI),” (2025), Status: Under Examination
4. R. Aman, A. Azeem, D. Kumar, A. Kumar, and M. Rizwan, “Novel and Energy-Efficient IoT-Based Self-Dust Cleaning Mechanisms for Solar PV Module,” (2025), Status: Under Examination

TABLE OF CONTENTS

ACKNOWLEDGEMENTS	I
CANDIDATE’S DECLARATION.....	III
CERTIFICATE BY THE SUPERVISOR(S).....	IV
ABSTRACT.....	V
LIST OF PUBLICATION.....	VII
LIST OF PATENTS	X
LIST OF TABLES	XX
LIST OF FIGURES	XXII
LIST OF SYMBOLS AND ABBREVIATION	XIII
LIST OF ABBREVIATIONS	XIV
CHAPTER 1	1
INTRODUCTION.....	1
1.1 GENERAL BACKGROUND.....	1
1.1.1 Renewable Energy and Global Energy Transition.....	1
1.1.2 Electric Vehicle Energy Storage Systems and Their Significance	3
1.1.3 Challenges in Lithium-Ion Battery Systems	4
1.2 RESEARCH MOTIVATION	6
1.2.1 Need for Advanced Cathode Materials.....	6
1.2.2 Limitations of Conventional Modelling and AI Approaches.....	6
1.2.3 Importance of Operating and Environmental Conditions.....	6
1.2.4 Green AI Perspective for Sustainable Energy Storage	7
1.3 PROBLEM FORMULATION	7
1.4 THESIS ORGANIZATION	8

CHAPTER 2	10
LITERATURE REVIEW	10
2.1 INTRODUCTION	10
2.2 ENERGY STORAGE SYSTEMS FOR EVS: AN OVERVIEW	10
2.2.1 Evolution of Rechargeable Battery Generations	11
2.2.2 Role of LIBs in EVs Applications	12
2.3 LIBs CATHODE MATERIALS	13
2.3.2 Lithium Nickel Manganese Cobalt Oxide (LiNiMnCoO ₂).....	14
2.4 BATTERY MANAGEMENT SYSTEMS	15
2.4.1 Role of BMS in EVs	16
2.4.2 Functional Components of BMS	17
2.5 BATTERY STATES AND THEIR ESTIMATION TECHNIQUES	17
2.5.1 State of Charge, State of Energy, and State of Health	19
2.5.2 Conventional and Model-based Approaches	21
2.5.3 Data-driven and AI-based methods.....	22
2.5.4 Challenges in Estimation Accuracy and Efficiency.....	23
2.6 ARTIFICIAL INTELLIGENCE IN BMS.....	24
2.6.1 Green AI and Energy-Efficient Approaches.....	25
2.7 EFFECT OF ENVIRONMENTAL AND OPERATING CONDITIONS	26
2.7.1 Temperature variations	27
2.7.2 Dynamic load profiles and drive cycles.....	28
2.7.3 Aging and Degradation Mechanisms.....	30
2.7.4 Strategies for Condition-Aware AI Estimation.....	31
2.8 SUMMARY RESEARCH GAPS AND CONTRIBUTIONS.....	32
2.9 OBJECTIVE OF THESIS	34

CHAPTER 3.....	35
SYNTHESIS AND CHARAECTERIZATION OF NI-RICH NMC 811	
CATHODE MATERIAL	35
3.1 INTRODUCTION	35
3.2 LITERATURE REVIEW OF CATHODE MATERIALS	35
3.2.1 Ni-Rich Cathode Materials NMC811	35
3.3 MATERIALS AND METHODS.....	37
3.3.1 Selection of NMC811 as a Layered Cathode.....	37
3.3.2 Solid-State Reaction Route for Synthesis	37
3.3.3 Experimental Procedure and Process Flow	37
3.4 CHARACTERIZATION TECHNIQUES.....	39
3.5 RESULTS AND DISCUSSION	39
3.5.1 Thermal Stability and Phase Formation Analysis.....	39
3.5.2 Structural Properties	40
3.5.3 X-ray Diffraction (XRD) Analysis	41
3.5.4 Morphological and Elemental Analysis.....	44
3.6 CONCLUSION.....	46
CHAPTER 4.....	47
DESIGN AND MODELLING OF AI-BASED APPROACH FOR STATE	
ESTIMATION OF LITHIUM-ION BATTERY.....	47
4.1 INTRODUCTION	47
4.2 DATA-DRIVEN APPROACHES FOR STATE ESTIMATION OF LIBs ..	47
4.2.1 Convolutional Neural Network Architecture.....	47
4.2.2 Long Short-Term Memory Architecture.....	48
4.2.3 Bidirectional Long Short-Term Memory Architecture.....	50
4.2.4 Stacked Bidirectional LSTM Network	52

4.2.5 Challenges in Accurate SOC/SOE Estimation	53
4.2.6 Green AI Perspective in Battery State Estimation.....	54
4.3 DESIGN AND MODELING PROPOSED HYBRID FILTER TECHNIQUE FRAMEWORK	55
4.3.1 Mathematical Modelling of FT, Supervised Learning and Sliding Window Approach.....	56
4.4 EXPERIMENTAL SETUP AND DATASET DESCRIPTION.....	60
4.4.1 18650 Battery Specifications and Testing Conditions.....	61
4.4.2 Dynamic Drive Cycles.....	62
4.4.3 Battery Data Diversity Analysis	63
4.4.4 Model Evaluation Metrics	64
4.5 RESULTS AND DISCUSSION	65
4.5.1 Model Performance without FT in different Drive Cycles.....	65
4.1.1.1 HWFET Drive Cycle	65
4.1.1.2 LA92 Drive Cycle.....	65
4.1.1.3 UDDS Drive Cycle	66
4.1.1.4 US06 Drive Cycle.....	67
4.5.2 Model Performance with FT in different Drive Cycles.....	67
4.5.2.1 HWFET Drive Cycle	69
4.5.2.2LA92 Drive Cycle.....	69
4.5.2.3 UDDS Drive Cycle	69
4.5.2.4 US06 Drive Cycle.....	70
4.5.2.5 Computational Efficiency and Energy Consumption Analysis	70
4.5.3 Filtering Technique and Its Role in BMS.....	71
4.6 CONCLUSION.....	72

CHAPTER 5.....	73
DEVELOPMENT OF AI-BASED ALGORITHM FOR BATTERY HEALTH MONITORING IN BMS.....	73
5.1 INTRODUCTION	73
5.2 NEED of AI-BASED ALGORITHM FOR BATTERY HEALTH MONITORING.....	75
5.3 PROPOSED RESEARCH METHODOLOGY	75
5.3.1 Mathematical modelling of Filter Technique Approach.....	76
5.3.2 Proposed Techniques	81
5.3.2.1 Recurrent Neural Networks	81
5.3.2.2 Gated Recurrent Unit Architecture	83
5.3.2.3 Bidirectional Gated Recurrent Unit Architecture	84
5.4 EXPERIMENTAL SETUP AND DATASET.....	86
5.4.1 Battery Data Diversity Analysis	88
5.5 RESULTS AND DISCUSSIONS.....	89
5.5.1 Performance Analysis of Each Dataset with the Filtering Technique ..	89
5.5.1.1 Performance on B1-B2 and B05-B018 Dataset.....	90
5.5.2 Performance Analysis of Each Dataset without Filtering Technique...	92
5.5.2.1 Performance on B1 Dataset	92
5.5.3 Energy Efficiency and Computational Cost Evaluation	94
5.5.4 Comparison and Discussion of Different Approaches with and Without FT	95
5.5.5 Analysis of DL Model Reliability in Terms of Energy & Efficiency ..	97
5.5.6 Key Findings and Contributions	98
5.5.7 Limitations of Proposed Approach.....	99
5.6 ROLE OF PROPOSED FT IN BMS	99
5.6.1 Real-Time Applicability of Proposed Algorithm	99

5.6.2 Deployment Considerations in Embedded Platforms	100
5.6.3 Advantages over Conventional Monitoring Methods.....	100
5.7 CONCLUSION.....	100
CHAPTER 6.....	101
AI-DRIVEN CONTROL STRATEGIES AND ANALYSIS OF OPERATING AND ENVIRONMENTAL CONDITIONS IN BATTERY STATE ESTIMATION	101
6.1 INTRODUCTION	101
6.2 AGING EFFECTS AND DEGRADATION UNDER DIFFERENT OPERATING STRESS.....	101
6.3 Process of Machine Learning based SOH Estimation.....	102
6.3.1 Experimental Setup and Dataset Description	103
6.3.2 Results and Discussion	104
6.3.3 Validation Across Different Battery Chemistries.....	105
6.3.4 NASA Dataset Generalization Validation	108
6.3.5 Performance Validation on Computational Efficiency.....	111
6.4 IMPACT OF TEMPERATURE VARIATIONS.....	113
6.4.1 AI-based SOC Estimation Under Different Thermal Profiles	113
6.4.2 Proposed Work	113
6.4.2.1 Data Processing.....	114
6.4.2.1 Model Training and Hyperparameter Tuning.....	115
6.4.2.2 Analysis and Discussion on Impact of Temperatures on LIBs Performance	116
6.5 CONCLUSION.....	126
CHAPTER 7.....	127
CONCLUSIONS, FUTURE SCOPE, AND SOCIETAL IMPACT	127
7.1 CONCLUSION.....	127

7.2 FUTURE SCOPE OF RESEARCH	128
7.3 SOCIETAL IMPACT	129
7.3.1 Linking Research Objectives with SDGs for Societal Impact.....	130
REFERENCES.....	132

LIST OF TABLES

Table 4. 1 Data description with and without filter techniques	60
Table 4. 2 The battery technical information.....	62
Table 4. 3 The statistical performances of proposed models without FT.....	67
Table 4. 4 The statistical performances of proposed models with FT	69
Table 4. 5 Energy consumption and computational time comparisons of all models	72
Table 5. 1 Literature related to SOH estimations	73
Table 5. 2 Data description with and without filter techniques	81
Table 5. 3 Technical Specification of LIBs	88
Table 5. 4 The statistical performances of proposed models with FT	91
Table 5. 5 The statistical performances of proposed models without FT.....	94
Table 5. 6 Energy consumption and computational time comparisons of all models during the different datasets	96
Table 5. 7 Energy consumption and computational time comparisons of all models during the different datasets	98
Table 6. 1 Lithium-ion batteries technical specifications.	104
Table 6. 2 Li-ion batteries characteristics	115
Table 6. 3 LSTM estimation accuracy results of the LA92 test driving cycle at different temperatures.....	119
Table 6. 4 GRU Estimation results of the LA92 test driving cycle at different temperatures	119
Table 6. 5 CNN Estimation results of the LA92 test driving cycle at different temperatures	122

Table 6. 6 CNN Estimation results of the LA92 test driving cycle at different temperatures 125

Table 6. 7 Comparison of the accuracy performances of different reports for SOC estimation 125

LIST OF FIGURES

Figure 1.1 Global ACC battery demand by application and chemistries (a-b). India's ACC battery demand by application and chemistries(c-d).	2
Figure 1.2 Different types of electric vehicle energy storage systems	4
Figure 1.3 Schematic diagram of charge-discharge configurations of a LIBs.	4
Figure 2.1 Different types EVs and their power sources	13
Figure 2.2 Components of a typical BMS architecture.....	16
Figure 2.3 Cell monitoring block diagram of BMS.....	17
Figure 2.4 Different types of battery states estimation techniques.....	18
Figure 2.5 A classification of SOC estimation techniques	20
Figure 2.6 Classification of approaches for SOH estimation	20
Figure 2.7 AI application in various areas of EVs.....	25
Figure 3.1 Schematic synthesis diagram of NMC811 via solid state reaction route	38
Figure 3.2 Thermogravimetric analysis of synthesized NMC811 sample.....	40
Figure 3.3 FTIR spectra of the synthesized NMC811	41
Figure 3.4 X-ray diffraction of pattern of NMC811 sample.....	42
Figure 3.5 SEM images and EDX spectra of NMC811 sample	45
Figure 4.1 1D-CNN model structure for feature extraction.....	48
Figure 4.2 The internal structure of an LSTM unit.....	49
Figure 4.3 Bidirectional LSTM model structure.....	51
Figure 4.4 Stacked bidirectional LSTM model structure.....	53
Figure 4.5 The proposed SOC and SOE estimation framework with filter technique	56
Figure 4.6 The proposed filter technique with the supervised learning model.....	57

Figure 4.7 Actual datasets of the four different drive cycles without the filter techniques	59
Figure 4.8 Actual datasets of the different four cycles with the filter techniques	59
Figure 4.9 Schematic diagram of the experimental test bench and data logging system .	62
Figure 4.10 The four drive cycles for tested the LIBs	63
Figure 4.11 The correlation matrix of four different EV drive cycles.....	64
Figure 4.12 The SOC/SOE estimation result (a-d) and estimation errors (e-h) without FT (a) HWFET; (b) LA92; (c) UDDS; (d) US06; drive cycles.....	66
Figure 4.13 SOC/SOE estimation result (a-d) and estimation errors with FT (e-h), (a) HWFET (b) LA92; (c) UDDS; (d) US06; drive cycles	68
Figure 5.1 The proposed SOH estimation framework with filter technique.....	76
Figure 5.2 The proposed filter technique	79
Figure 5.3 Actual datasets (a, c, e, and g) and datasets with the filter techniques (b, d, f, and h).	80
Figure 5.4 Structure of the RNN.....	82
Figure 5.5 Structure of the GRU.....	84
Figure 5.6 Structure of the BiGRU	85
Figure 5.7 Experimental setup for lithium-ion battery testing.....	87
Figure 5.8 The correlation matrix of four different SOH datasets: B1, B2, B05, B06, B07, and B18	89
Figure 5.9 SOH estimation result (a-f) and estimation errors with the FT (g-l), (a) B1, (b) B2, (c) B05, (d) B06, (e) B07, (f) B018, datasets.	90
Figure 5.10 The SOH estimation result (a-f) and estimation errors without incorporation filter technique (g-l), (a) B1, (b) B2, (c) B05 (d) B06, (e) B07, (f) B018 datasets.....	93

Figure 6.1 The ML-based framework for SOH estimation of LIBs	102
Figure 6.2 The degradation trajectory of batteries; (a) CCCV process approach (b-b'), battery test bench setup, (c-c') NASA battery and experimental battery dataset	103
Figure 6.3 SOH estimation results against the measurements of D1-D4 batteries (a-d).	105
Figure 6.4 SOH estimation errors (a-d), computational time (e), Maxerror (f), R^2 (g) across the D1-D4 batteries.	106
Figure 6.5 NASA batteries SOH estimation results of B5, B6, B7, and B18.....	109
Figure 6.6 SOH estimation errors (B5, B6, B7, and B18), computational time (e), Maxerror (f), R^2 (g) across the NASA batteries B5, B6, B7, and B18	110
Figure 6.7 Computational efficiency (a) D1, D2, D3, and D4, (b) B5, B6, B7, and B18	112
Figure 6.8 The flow chart of the proposed work	114
Figure 6.9 The "Multi-time input" structure of the network.....	115
Figure 6.10 Actual and estimated performances and errors with LSTM under different temperatures.....	117
Figure 6.11 Actual and estimated performances and errors with LSTM under different temperatures.....	118
Figure 6.12 Actual and estimated performances and errors with GRU under different temperatures.....	120
Figure 6.13 Actual and estimated performances and errors with GRU under different temperatures.....	121
Figure 6.14 Actual and estimated performances and errors with CNN under different temperatures.....	123

Figure 6.15 Actual and estimated performances and errors with CNN under different temperatures..... 124

Figure 7.1 Integration of Sustainable Development Goals with the thesis objectives.... 131

LIST OF SYMBOLS AND ABBREVIATION

SOC_t and SOC_0	SOC at time t, and initial SOC;
SOE_t and SOE_0	SOE at time t, and initial SOE;
C_n and E_n	Nominal capacity and total available energy;
$p(\xi)$, $i(\xi)$, $u(\xi)$, ξ	Power, current, and voltages at time ξ ;
N_i	Normalized sequence
x_i	Normalized value in the normalized datasets
n	Total number of elements in the sequence N_i
F	Filtered sequence
k	Number of duplicate numbers in each group
f_i	Average for each batch
$\frac{n}{k}$	Length of the filtered sequence
$X_i, (i=1, 2, 3 \dots n)$	Input sequence
n_steps	Subsequence of length in input sequence X_i
$pred_steps (p)$	Number of predicted steps
$mean_batch$	Grouping the sequence into smaller batches of size
$y_{i,t}$	Output/predicted values
C_{rated}	Rated capacity of the battery
C_{aged}	The current degraded capacity of the battery
D and d_i	Dataset, and i^{th} data point in the dataset
x_k	Each unique value in the dataset
G_k	Group of similar values corresponds to the value x_k .
δ	Filtered sequence the similarity threshold
R_k	The representative value of the group G_k
D_f	The filtered dataset
m	Number of groups formed after applying for the FT
$R_1, R_2, R_3 \dots R_m$	Representative values from each group
x_t , and \hat{x}_t	Measured battery parameter at time t, and Normalized feature value

LIST OF ABBREVIATIONS

ACT	Actual Computational Time
AI	Artificial Intelligence
ANN	Artificial Neural Network
ARMA	Auto regression moving average
Bi-LSTM	Bidirectional Long Short-Term Memory
BMS	Battery Management System
CCCV	Constant Current Constant Voltage
CE	Computational Efficiency (%)
CNN	Convolutional Neural Network
DC	Direct Current
DL	Deep Learning
DOD	Depth of Discharge
ECM	Equivalent Circuit model
EDS/EDX	Energy Dispersive X-ray Spectroscopy
EIS	Electrochemical Impedance Spectroscopy
ESS	Energy Storage System
EV	Electric Vehicles
FFNN	Feed Forward Neural Network
FT	Filtering Techniques
FTIR	Fourier Transform Infrared Spectroscopy
GRU	Gated Recurrent Unit
HWFET	Highway Fuel Economy Test Cycle
KF	Kalman Filter
LA92	California Unified Driving Cycle
LCO	Lithium Cobalt Oxide
LFP	Lithium Iron Phosphate
LIBs	Lithium-ion batteries
Li-S	Lithium-Sulphur Battery
LMO	Lithium Manganese Oxide
LSTM	Long Short-Term Memory

MAE	Mean Absolute Error
MAPE	Mean Absolute Percentage Error
ML	Machine Learning
MLP	Multi-Layer Perceptron
MSE	Mean Squared Error
NCA	Nickel Cobalt Aluminium Oxide
NMC	Nickel Manganese Cobalt Oxide
NN	Neural Networks
OCV	Open Circuit Voltage
PINNs	Physics-Informed Neural Networks
RCT	Reference Computational Time
RMSE	Root Mean Square Error
RNN	Recurrent Neural Network
RUL	Remaining Useful Life
SDG	Sustainable Development Goal
SEM	Scanning Electron Microscopy
SEI	Solid Electrolyte Interphase
SOC	State of Charge
SOE	State of Energy
SOF	State of Function
SOH	State of Health
SOP	State of Power
SOT	State of Temperature
SSB	Solid-State Battery
SVM	Support Vector Machine
TGA	Thermogravimetric Analysis
TL	Transfer Learning
UDDS	Urban Dynamometer Driving Schedule
UKF	Unscented Kalman Filter
US06	Supplemental Federal Test Cycle
V2G	Vehicle-to-Grid
WLTP	Worldwide Harmonized Light Vehicle Test Procedure
XRD	X-ray Diffraction

CHAPTER 1

INTRODUCTION

1.1 GENERAL BACKGROUND

1.1.1 Renewable Energy and Global Energy Transition

The global transition toward low-carbon economy has accelerated significantly following international climate commitments aimed at limiting global temperature rise. Currently, global warming has already reached approximately 1.1 °C above pre-industrial levels, highlighting the urgency for rapid decarbonization across major energy-consuming sectors [1], [2]. Power and transportation together emit nearly 40% of global greenhouse gas emissions, making them critical target for energy transition strategies. In this evolving landscape, batteries have emerged as a foundational technology supporting both the electrification of transportation and the integration of variable renewable energy sources such as solar and wind.

Electric vehicles (EVs) play a critical role in reducing emissions from the transportation sector. However, battery energy storage systems (BESS) are growing in demand for peak shifting, grid stability, renewable energy integration, and energy reliability. Advanced battery technologies, including lithium-ion batteries and emerging chemistries such as sodium-ion, solid-state batteries, are the framework of climate action, energy security, and industrial assets. The global demand for advanced chemistry cell (ACC) batteries reached ~1.6 TWh in 2025, growing around 28%, compared to 2024. However, EVs are the largest contributors to global battery demand, projected to increase significantly, reaching ~ 3.8 TWh by 2030 and ~5 TWh by 2035, as shown in Figure 1.1(a). This growth is primarily driven by rising EV sales and increasing battery pack capacity used in long-range and heavy-duty EVs.

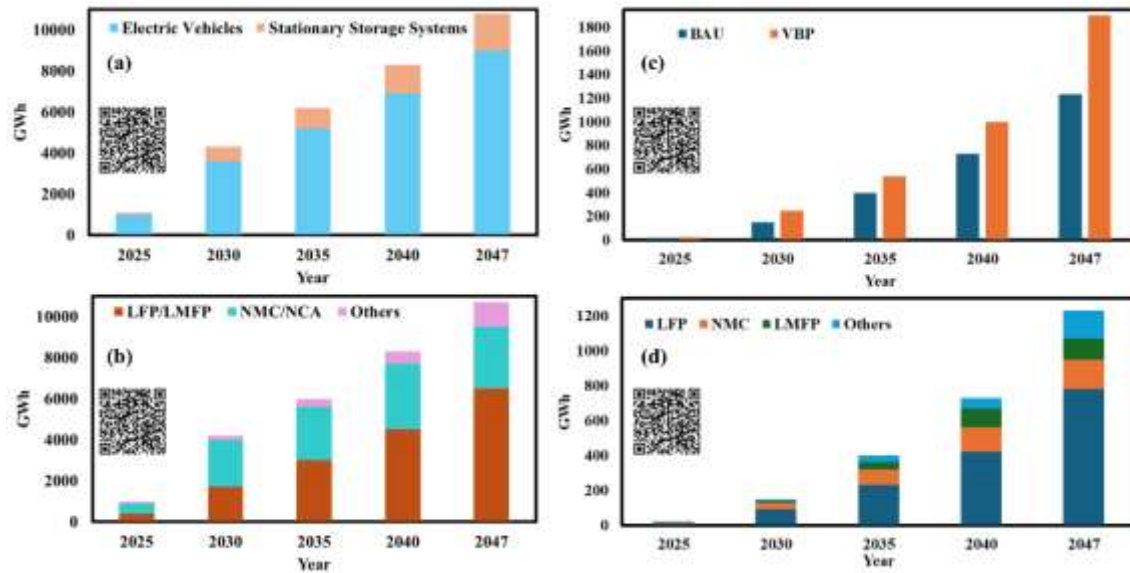


Figure 1.1 Global ACC battery demand by application and chemistries (a-b). India's ACC battery demand by application and chemistries(c-d) [1], [2].

As shown in Figure 1.1(b), advanced battery chemistries such as LFP/LMFP, NMC, and NCA account for the majority of demand from EV and stationary energy storage applications. The demand for stationary storage systems is expected to grow to ~ 600 GWh by 2030 and ~1 TWh by 2035. Overall, global EV battery demand is projected to reach approximately 7 TWh by 2040 and nearly 9 TWh by 2047, highlighting the dominant role of electric mobility in future battery demand. India's demand for ACC batteries was 28 GWh in 2025 and is projected to increase significantly in the coming decades. Under the business-as-usual (BAU) scenario, demand is expected to reach about 1.3 TWh by 2047, while under the Viksit Bharat Pathway (VBP) scenario, demand could reach nearly 1.9 TWh by 2047, as shown in Figure 1.1(c). However, the chemistry-wise distribution is shown in Figure 1.1(d). EVs are projected to remain the primary driver of battery demand, accounting 60% of total demand in 2025, increasing to approximately 74-77% by 2027. The stationary storage systems are expected to contribute around 35-38% of demand until 2035, declining to about 25% by 2047 as EV adoption accelerates. Lithium-based chemistries,

particularly LFP and LMFP, are expected to dominate the Indian ACC market, accounting for over 85% of total battery demand until 2035.

1.1.2 Electric Vehicle Energy Storage Systems and Their Significance

The global energy storage systems (ESSs) market is expected to exceed 200 GWh in installed capacity by 2024, with LIBs majority share due to their dual role in stationary storage and electric mobility applications. Beyond grid balancing, ESS play a central role in peak shaving, load shifting, frequency regulation, black-start capability, and renewable integration, making them necessary in modern smart grids and microgrids. The EVs use different types of ESSs to power their electric motors. The most common types of ESSs used in EVs are shown in Figure 1.2. However, some have been commercialised, while others are still under development with varying technology readiness levels (TRL). Nowadays, electrochemical storage, i.e., batteries, are commonly used. There are two types of batteries: primary (non-rechargeable) and secondary (rechargeable) [3], [4]. Primary batteries are disposable batteries and are used only once. They are typically used in low-power applications such as remote controls, flashlights, and calculators [5]. However, secondary batteries are rechargeable and used repeatedly, making them suitable for high-energy devices, including smartphones, laptops, and EVs [6]. The LIBs are most used in EVs due to their high energy and power density. They deliver high power output for rapid acceleration and continuous driving performance. The principal operation of a LIBs involves the movement of lithium ions between the cathode and anode during charging and discharging, as shown in Figure 1.3. Charging involves the insertion of lithium ions into the cathode, while discharging involves the release of lithium ions from the anode to generate an electric current. The efficiency of LIBs depends on various factors, such as anode and cathode materials designed and maintenance [7]. In EVs, batteries are the main power source for the electric motor, propulsion, and auxiliary systems.

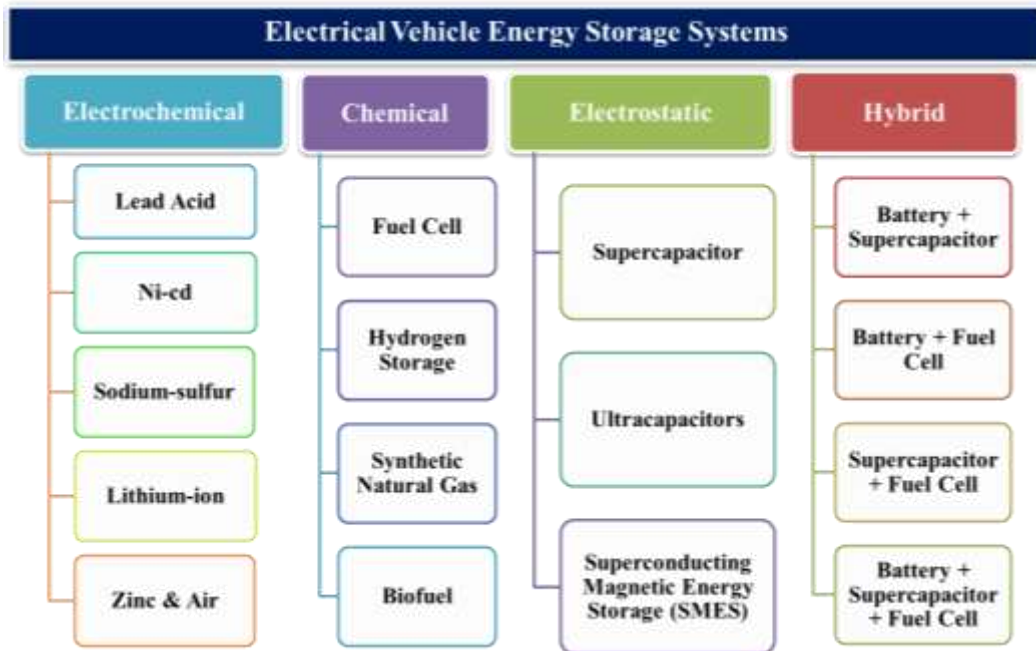


Figure 1.2 Different types of electric vehicle energy storage systems

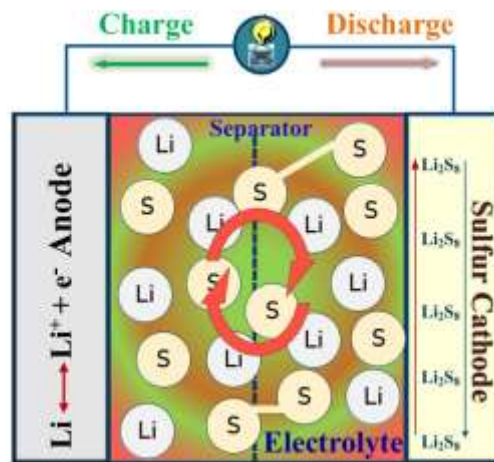


Figure 1.3 Schematic diagram of charge-discharge configurations of a LIBs.

1.1.3 Challenges in Lithium-Ion Battery Systems

Traditional LIBs suffer from technical and operational challenges. These include limited energy and power density, thermal runaway risk, rapid capacity degradation, high material cost, and sustainability [8]. In the view of cathode materials, they suffer from structural and morphological

issues, low energy and density, transition metal dissolution, and capacity degradation. These existing issues limited the performance, safety, and lifecycle of the LIBs [9].

The prediction of the battery states, such as state of charge (SOC), state of health (SOH), state of energy (SOE), state of power (SOP), and degradation patterns, has remained challenging due to nonlinear electrochemical dynamics, temperature sensitivity, and ageing effect. The conventional battery management system (BMS) still depends on the traditional techniques e.g., coulomb counting, electric circuit model (ECM), which suffer from cumulative errors and limited adaptability. This limits accurate health monitoring and early detection of faults [10].

LIBs performances strongly influenced by environmental factors such as temperature, humidity, and load variations. Conventional systems lack the advanced control strategies to mitigate environmental stress, leading to increased degradation, reduced safety, and shortened life cycles. These challenges highlighted the need for advanced material design, intelligent modeling, AI health monitoring, and adaptive control strategies for next generation ESSs.

Thermal runaway (TR), triggered by overcharging, mechanical abuse, and increase temperatures, remains a critical safety concern in traditional batteries. This arises at high SOC, operational stresses such as fast charging and deep discharging. From a materials perspective, high-energy density cathode materials such as NMC and NCA are constrained by supply and sustainability, whereas the LFP cathode materials deliver lower energy density [11].

These challenges highlighted, the need for the advanced cathode material synthesis, accurate battery modelling, AI based health monitoring with BMS, and advanced adaptive control strategies to manage environmental effects. Integrating these approached with Green AI framework enables the development of reliable, efficient and sustainable ESS for EVs.

1.2 RESEARCH MOTIVATION

1.2.1 Need for Advanced Cathode Materials

The rapid growth of EVs requires LIBs having higher energy and power densities, longer cycle life, and improved sustainable. Conventional cathode chemistries present significant limitations such as thermal stability, material shortage, and sustainability. For example, nickel and cobalt-rich layered oxides provide high capacity but suffer from thermal stability, rapid degradation under fast charging, and supply chain concerns related to nickel and cobalt [12], [13]. These limitations highlight the need to synthesize and characterize alternative advanced cathode materials, such as layered, spinel, olivine, and composite structures, to achieve a balance between performance, cost, and environmental impact.

1.2.2 Limitations of Conventional Modelling and AI Approaches

LIBs have non-linear, influenced by electrochemical dynamics, load variations, and environmental factors. Traditional AI models are computationally intensive and impractical for better accuracy in real-time applications [14]. However, many of AI-based computational approaches rely on large datasets and high computational power, which limits their applicability in embedded BMS. Moreover, black-box AI models often lack interpretability, which limits their adoption in safety critical EV applications [15]. To address these gaps, design efficient modeling frameworks and lightweight AI algorithms that estimate battery performance while minimizing computational overhead.

1.2.3 Importance of Operating and Environmental Conditions

The performance and durability of LIBs are significantly influenced by external factors, including ambient temperature, humidity, and charging conditions. The high temperatures increase electrolyte decomposition and induced TR, while low temperatures increase internal resistance and

reduce usable capacity due to slower electrochemical dynamics [16], [17]. Furthermore, the irregular charging and discharging cycles accelerate degradation. Neglecting these factors in the system design and modeling results in inaccurate performances prediction and increases risk of premature failure. Therefore, there is utmost need to develop an advanced adaptive control strategies algorithm that understand operational and environmental effects of LIBs and ensures improved safety of overall systems.

1.2.4 Green AI Perspective for Sustainable Energy Storage

As AI is integrated into battery modelling and management systems, its computational energy consumption must also be addressed. Recent studies on Green AI highlighted energy efficient model design through techniques such as pruning, quantization, and lightweight architectures, to reduce computational cost without losing estimation accuracy [18], [19]. Incorporating these principles into BMS algorithms not only ensures computational sustainability, while support broader goal of achieving eco-friendly and resource optimized battery ESSs. By embedding Green AI into battery behaviour prediction and health monitoring frameworks, this thesis aligns advanced energy storage research with global sustainability goals while enabling efficient real-time deployment in EV applications.

1.3 PROBLEM FORMULATION

Despite continuous advancements in the LIBs technologies, traditional systems still face interconnected challenges related to material limitations, safety risks, degradation under different operating conditions, and high computational cost in battery management. These existing challenges hinder the development of reliable, sustainable, and high performances ESS for EVs and other advanced applications. The research work is structures based the following key research objectives:

Enhancing cathode material performances through systematic synthesis and electrochemical analysis of layered/spinel/olivine/composite cathode material for rechargeable ESS.

Strengthening the battery behaviour prediction through advanced design and modelling frameworks under different operating conditions.

Improving the reliability by development of AI-based algorithms for battery health monitoring and prediction its degradation patterns within BMS.

Ensuring the safety by develop adaptive control strategies to understand the environmental and operational influence factors.

The main aim of the research is to bridge the gap between material advancements in LIBs cathodes and intelligent, energy efficient system level management strategies. The integration of the advanced cathode materials, predictive modelling, AI-driven health monitoring, and adaptive environmental control, the proposed framework aims to enhance safety, improve performance and increase life cycle. Finally, this research contributes to development of reliable, computational sustainable, and high-performance LIBs for EVs and advanced energy applications. The research methodology employed in this thesis integrates experimental synthesis, AI-driven modeling, and environmental analysis, forming a reliable approach to the design and development of sustainable energy storage systems for EVs. The methodology is structured into four major components:

1.4 THESIS ORGANIZATION

The thesis is comprises of seven chapters, providing a specific aspect of advanced ESSs and AI based battery management.

Chapter 1 represents the general background about ESSs challenges in conventional LIBs, defines research objectives and overall problem formulation. The overall research framework and motivation of the study toward AI approaches are also discussed, related to EV-ESSs.

Chapter 2 consist of reviews on fundamentals and limitations of energy storage technologies, LIBs materials, AI based BMS, state estimation techniques and environmental influences on battery performances. The theoretical concepts and existing research developments are discussed in detail and identifies research gaps and contributions of the present work.

Chapter 3 focuses on synthesis and characterization of Ni-rich layered, spinel, olivine, and composite cathode materials, including structural, thermal, morphological and compositional analysis. The experimental procedures, material properties and analytical findings discussed.

Chapter 4 discussed and developed an AI-based frameworks for SOC, SOH, and SOE estimation methods and introduced a novel filtering-based data optimization technique for improving computational efficiency and estimation accuracy. The implementation of models, as well as validate estimation performance are discussed in detail.

Chapter 5 presents the design and a novel lightweight Green AI-based algorithm for energy efficient battery health monitoring framework. The chapter examines redundant data filtering strategy, model compression techniques, and validation against benchmark methods and validated the results with existing work.

Chapter 6 investigate the effect of temperature, load variations, and environmental and operating condition on LIBs performance. Introduces condition-aware estimation and control strategies to mitigate risks and enhance battery safety. The experimental validations and performances evaluation under varying conditions are explored.

Chapter 7 summarizes the key findings, research contributions, societal and impacts. Proposes future research directions toward contributes to sustainable LIBs for EVs.

CHAPTER 2

LITERATURE REVIEW

2.1 INTRODUCTION

This chapter presents a comprehensive review of the existing limitations in LIBs, with a focus on cathode materials synthesis, battery state estimation techniques, AI applications in BMS, and their impact on environmental and operating conditions. The review identifies key advancements in synthesis, BMS real-time health monitoring, exploration of challenges, and the identification of research gaps.

2.2 ENERGY STORAGE SYSTEMS FOR EVS: AN OVERVIEW

The ESSs play a fundamental role in the transition toward sustainable mobility, mainly the operations and performance of EVs. Unlike the traditional ICE vehicles, EVs are fully powered by the electrical energy stored within the on-board battery systems [3]. Therefore, the overall efficiency, power delivery, cost, safety and driving range of EVs are directly determined by the performances of the ESSs [4]. An ESS for EVs must satisfy several criteria, such as high energy and power density for increasing driving range and regenerative braking and acceleration, fast charging, thermal stability, long cycle life, and operational safety [20]. The different types of energy storage technologies have been explored in EV applications, including batteries, supercapacitors, and hybrid storage configurations [21]. However, LIBs are still used as a dominant technology due to their overall efficiency compared to traditional batteries such as lead acid and nickel-based configurations. Despite their advantages, LIBs face challenges including material sustainability, TR, rapid degradations, state estimation issues and operational/environmental safety. These limitations motivate this research aim to enhance

advanced cathode material synthesis, accurate battery modelling, AI-based health monitoring with BMS, and advanced adaptive control strategies to manage environmental effects [22].

The ESSs for the EVs are broadly classified into the following categories: electrochemical, chemical, electrostatic and hybrid, as discussed in chapter 1. This section provides an overview of the role of batteries in this ecosystem and their historical evolution, background, and framework for advanced developments in cathode materials and AI-driven management of EV batteries.

2.2.1 Evolution of Rechargeable Battery Generations

LIBs still hold more than 90% of the market [23]. LFP chemistries now make up almost half of all EV sales around the world because they are cheaper. Current commercial cells have energy densities that range from 150 Wh/kg (LFP) to 250 Wh/kg (high-nickel NMC), which means they can support a wider range of vehicles. Also, the average price of battery packs has dropped by about 90% since 2010. In China, prices have recently dropped below the important \$100/kWh level, making EVs more competitive with vehicles that use ICEs [24].

The evolution of rechargeable batteries has been driven by the continuous demand for high energy and power density, improved safety, long cycle life and cost-effectiveness, EV applications. The first practical rechargeable battery, the lead-acid system developed by Gaston Planté's in 1859, with low specific energy 30-50 Wh/kg, which powered early EVs [25]. However, its heavy weight and limited energy density limit the driving range. This was followed by nickel-cadmium (NiCd) batteries in 1899, which have improved durability and moderate energy density, 40-60 Wh/kg, but suffer from the memory effects and environmental concern. In the 1980s, nickel-metal hydride (NiMH) batteries with energy density 60-120 Wh/kg, increased cycle life and were widely adopted in hybrid EVs such as the Toyota Prius [26]. However, these batteries remained a challenge for EVs to have long driving range. A major invention occurred in 1991 with the full

commercialization of LIBs having significantly high specific energy 150-250Wh/kg, nominal cell voltage 3.6-4.2 V, light weight and good efficiency [27]. These advantages boost the EVs overall efficiency and become a modern dominant energy storage technology. However, challenges such as rapid degradation, material unavailability, and thermal instability continue to drive the research for the next-generation systems.

2.2.2 Role of LIBs in EVs Applications

The EVs are broadly classified into battery electric vehicles (BEVs), Hybrid electric vehicles (HEVs), plug-in hybrid electric vehicles (PHEVs) and fuel cell electric vehicles (FCEVs) as shown in Figure 2.1. BEVs operate by using battery packs as power source [28]. HEVs are a combination of an ICE with an electric motor and battery packs. The PHEVs integrate both systems with the external charging capability. In contrast, the FCEVs generate the electricity onboard using the hydrogen fuel cells. However, these still incorporate a battery system to store recovered energy and support transit power demands. In all the configurations, the ESSs play a critical role in deciding the vehicle efficiency, acceleration performances, driving range and overall reliability. Among storage technologies, LIBs have dominant solutions. LIBs provide the power for propulsion, auxiliary loads, and regenerative braking energy storage, while maintaining high efficiency up to 90%, which enhances overall vehicle energy utilisation [29]. In modern EV architectures, LIBs packs are integrated with an advanced BMS that monitors critical parameters such as voltage, current, temperature, SOC, SOH, SOE and SOP. This integration ensures safe operation, enhances performance and protection against overcharge and deep discharge and TR [30].

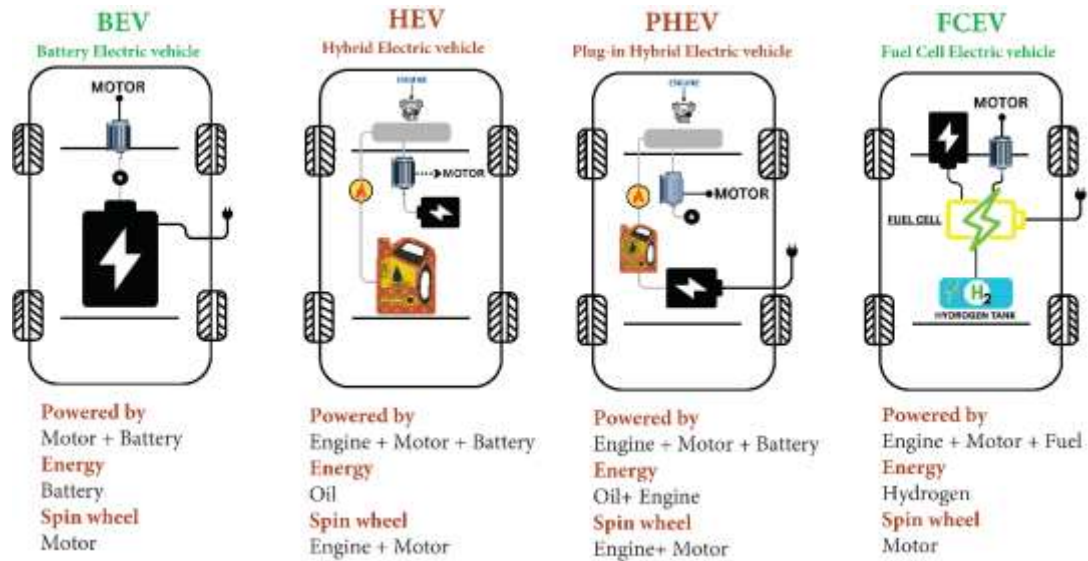


Figure 2.1 Different types EVs and their power sources

2.3 LIBs CATHODE MATERIALS

A LIBs consists of four main components: anode, cathode, electrolyte and separator [31]. The cathode act as lithium-ion source for discharging, the anode stores lithium ions during charging, the electrolyte enables ionic transport between electrodes, and the separator prevents electrical short circuits. However, cathode materials are the bottleneck for LIB performance in EVs, influencing energy density, cycle life, and safety. This section reviews layered, spinel, olivine, and composite types, emphasising synthesis and electrochemical analysis needs [32].

The cathode materials in the LIBs are generally classified into four major structural families, such as layered, spinel, olivine, and composite structures [33], [34]. Layered oxides such as lithium cobalt oxide LiCoO_2 (LCO), and mixed layered nickel manganese cobalt oxide (NMC)/nickel cobalt aluminum oxide (NCA) are widely described in the literature for their high specific energies and wide adoption in EVs [35]. However, the nickel and cobalt dependency remains a concern. Spinal cathodes, e.g., LiMn_2O_4 , introduced by Thackeray et al. (1983), provide 3D lithium-ion diffusion pathways, offering good rate capability and improved thermal stability, but with

moderate energy density [32]. The olivine cathodes, such as LFP, reported by Padhi et al. (1997), are known for their thermal stability, enhanced safety, and good cycle life, although with lower energy density [36]. Furthermore, composite and modified cathodes involve doping, coating, and gradient structures to enhance conductivity, cyclability, and structural stability. As reported in the recent literature review on advanced cathode engineering [37].

To improve the performance of the advanced cathode chemistries, such as LMO, NMC, and NCA, enhance energy density and power capability, and voltage output, thus increasing the EV driving range [38]. LFP and LTO-based systems are better because they are safer and last longer. Even though LIBs have the benefit of being recyclable, problems with the availability of raw materials and the cost per kWh continue to push research into new and long-lasting cathode materials [39].

2.3.2 Lithium Nickel Manganese Cobalt Oxide (LiNiMnCoO₂)

NMC is a layered-based cathode material that became commercially available around 2004 and is now widely adopted in EV batteries [40]. NMC cathodes combine nickel (Ni), manganese (Mn), and cobalt (Co) within a layered α -NaFeO₂ structure to achieve balance of energy density, cycle life, and cost. Nickel increases specific capacity and energy density, manganese improves thermal and structural stability, and cobalt enhances the layered framework, thereby increasing the electronic conductivity. The electrochemical performance of NMC depends on the compositions such as NMC111, NMC622, and NMC811. Increasing Ni content improves specific energy and driving range, while high Mn content improves specific power and safety characteristics. However, high-Ni contents are more susceptible to oxygen release, surface reconstruction, transition metal dissolution, and accelerated degradation under high voltage and fast charging conditions. In addition, the dependence on cobalt raises concerns about availability, cost, and sustainability. To address these issues, recent research focuses on low and cobalt-free NMC chemistries [39]. Ni-

rich layered cathodes with surface/interface engineering, doped nanostructures to suppress interfacial degradation and impedance growth. Safety and cost-sensitive EVs applications, LFP modified LFP composites are preferred, whereas NI-rich layered cathodes remain suitable for long driving range EVs requiring high energy density. Preventing oxygen release, surface reconstruction, and transition metal dissolution remains essential for Ni-rich and Li-rich layered oxides. Designing robust cathode-electrolyte interphases that suppress electrolyte oxidation, limit impedance growth, and tolerate high voltages is critical. Modern interface engineering has improved stability and performance, but large-scale manufacturing with consistent quality and lower costs is still a concern. Therefore, for next-generation EV-ESSs, it's still very important to enhance NMC cathodes by stabilizing their structure, controlling their structural stability, interfaces, and materials sustainability.

2.4 BATTERY MANAGEMENT SYSTEMS

The BMSs are embedded control systems that integrate mechanical, computational and electrical techniques to monitor, protect and regulate battery performance [41]. In EVs, BMS play a critical role in ensuring cycle life, safety, performance, and reliability of LIBs [42]. The primary function of the BMS is to extend battery lifespan and enhance system dependability through continuous monitoring and controlling key parameters. These include voltage, current, temperature, SOC, SOH, SOE and SOP. By analyzing these parameters in real time, the BMS prevent against overcharge, overheating, deep discharge, cell balancing, and TR [43]. It also employed multiple control strategies such as charge/discharge regulation, cell balancing, fault detection mechanism, and thermal management. These strategies ensure operation within the safe limits, mitigate safety risk, and increase energy utilisation. Figure 2.2 illustrates the essential components of a typical BMS architecture that are necessary for the efficient functioning of an EV.

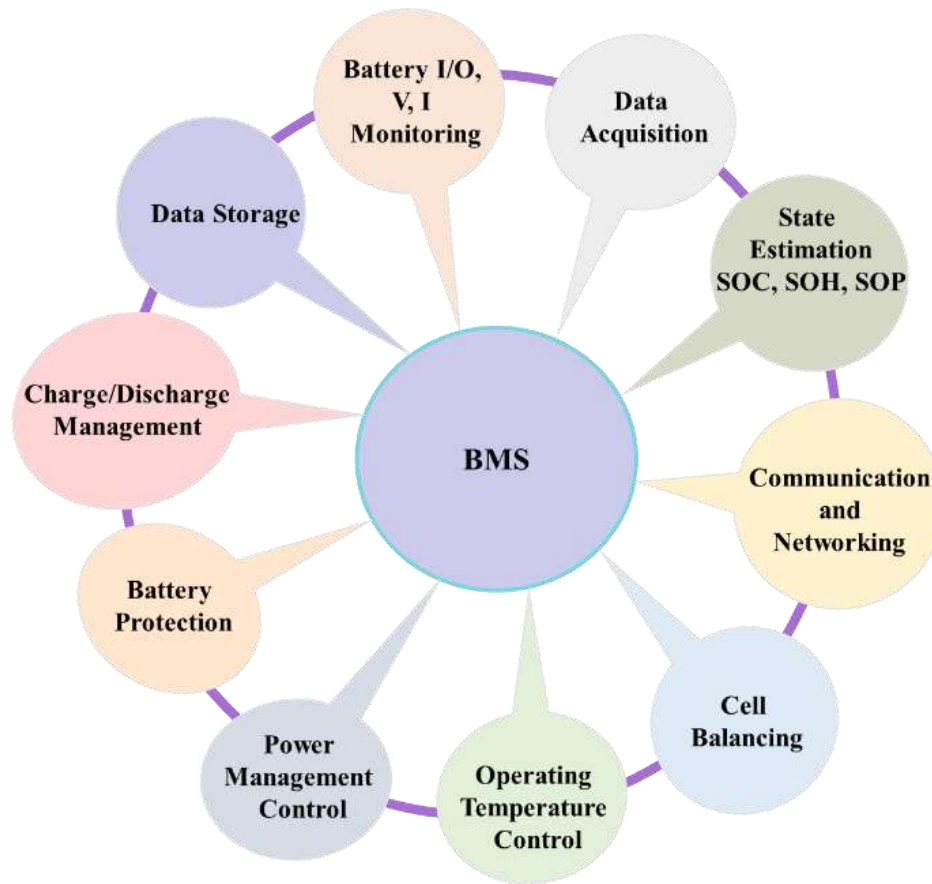


Figure 2.2 Components of a typical BMS architecture

2.4.1 Role of BMS in EVs

As shown in Figure 2.3, the BMS requires continuous access to critical information, including cell voltage, current, temperature, SOC, SOH, SOE, and SOP, to effectively perform its functions [44]. The cell may react in several ways while the battery is being charged and discharged. Therefore, it's critical to continuously monitor LIBs to understand their conditions and performance indicators better. The information obtained from battery cell monitoring can be used to manage, protect, balance, and control operations [45]. This integrated monitoring and control framework ensures safe operation, enhances performance and protection against overcharge and deep discharge and extends the battery life in EV applications.

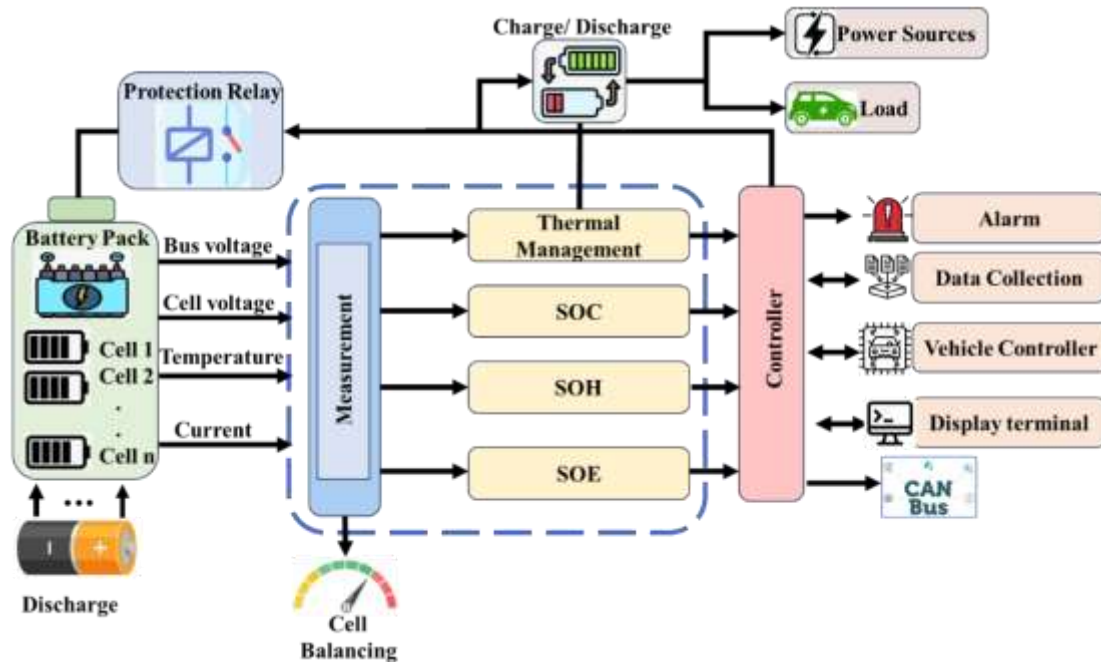


Figure 2.3 Cell monitoring block diagram of BMS

2.4.2 Functional Components of BMS

To ensure safe and reliable battery operation, BMS must estimate the battery key state variable that shows battery condition and performance. These include SOC, SOH, remaining useful life (RUL), SOF, SOP, SOE, state of safety (SOS), and state of temperature (SOT) [45]. This accurate estimation of these parameters is necessary for charge control, fault prevention, power management and lifetime prediction of LIBs in EVs [46].

2.5 BATTERY STATES AND THEIR ESTIMATION TECHNIQUES

The operational condition of a battery cell at any instant is described by the internal variables known as battery states, many of which are not directly measurable. As shown in Figure 2.4, different types of battery states estimation techniques are employed to estimate these states, including conventional, model-based, data-driven and hybrid approaches for SOC, SOE, and SOH under dynamic operating conditions.

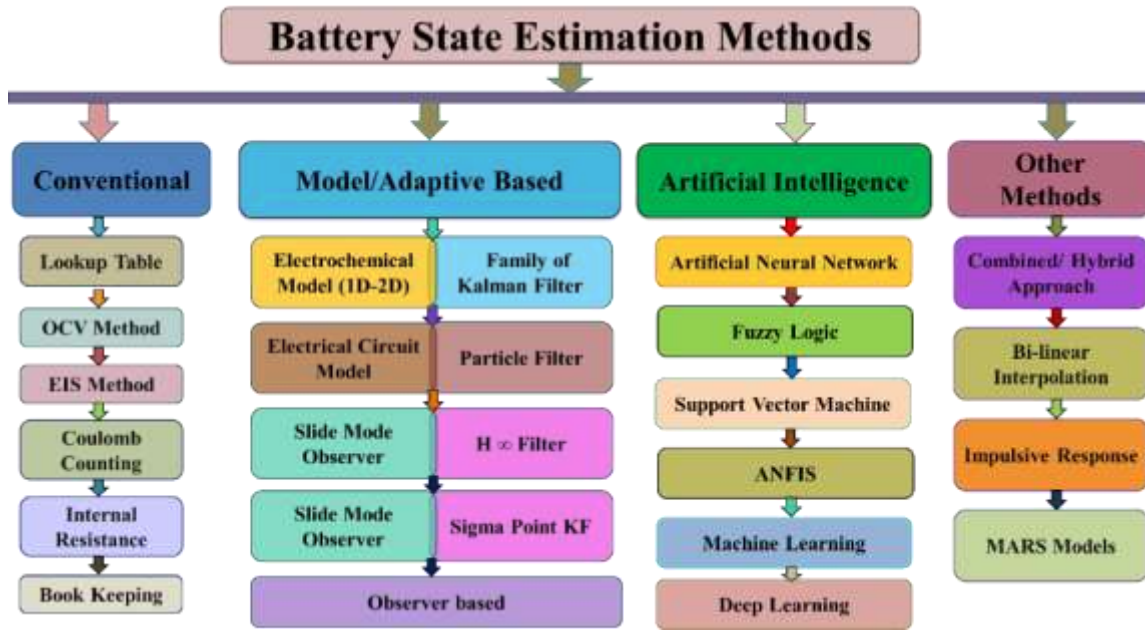


Figure 2.4 Different types of battery state estimation techniques

The most commonly state is the SOC, which indicates the available charge relative to nominal capacity [47]. In addition to SOC, internal states related to hysteresis behaviour and diffusion dynamics, which strongly influence open-circuit voltage and transient response of the battery [48]. In modeling term these are treated as state variables, representing the minimal set of parameters required to describe system behavior to predict future response under given inputs [49]. In practical BMS application, battery states broadly include health and performance indicators that support monitoring, control and safety managements. A notable example is SOH, which quantifies the gradual degradation of a battery cell by comparing its current performance with its initial condition [50]. Therefore, the battery state estimation (BSE) is a critical component for BMS, enabling the accurate assessment of these key battery states. These estimations are essential for improving battery performance, ensuring safety, and prolonging lifespan, in applications like EVs and renewable ESSs.

2.5.1 State of Charge, State of Energy, and State of Health

The accurate SOC/SOE estimation is essential for improving battery performance, ensuring safety, and prolonging the lifespan of EV batteries [51]. As shown in Figures 2.5 and 2.6, various battery state estimation techniques are employed, including model-based approaches e.g., electrochemical models and equivalent circuit models, data-driven techniques e.g., machine and deep learning methods, and hybrid approaches that combine physical modeling with data analytics for improved accuracy and robustness. to estimate these parameters. The classification of SOC and SOH estimation methods is shown in Figures 2.4 and 2.5. The SOC represent the ratio of the remaining capacity to nominal capacity.

$$SOC_t = SOC_0 - \frac{\int_0^t i(\xi) d\xi}{C_n} \quad (2.1)$$

Where the initial SOC is SOC_0 , SOC_t is SOC at time t, nominal capacity C_n , current $i(\xi)$. However, SOE is defined as the ratio of remaining battery energy to total nominal energy under specific operating circumstances.

$$\begin{aligned} SOE_t &= SOE_0 - \frac{\int_0^t p(\xi) d\xi}{E_n} \\ &= SOE_0 - \frac{\int_0^t i(\xi)u(\xi) d\xi}{E_n} \end{aligned} \quad (2.2)$$

SOE at time t is SOE_t , SOE_0 initial SOE, total available energy is E_n , current $i(\xi)$, power $p(\xi)$, and voltage $u(\xi)$ at time ξ , respectively. Battery SOE estimation was used to compute the available energy information of the battery. However, battery SOC refers to available capacity in ampere hour (Ah) rather than available energy in watt hour (Wh). The SOC and SOE can be represented by Eqs. 2.1 and 2.2 [52].

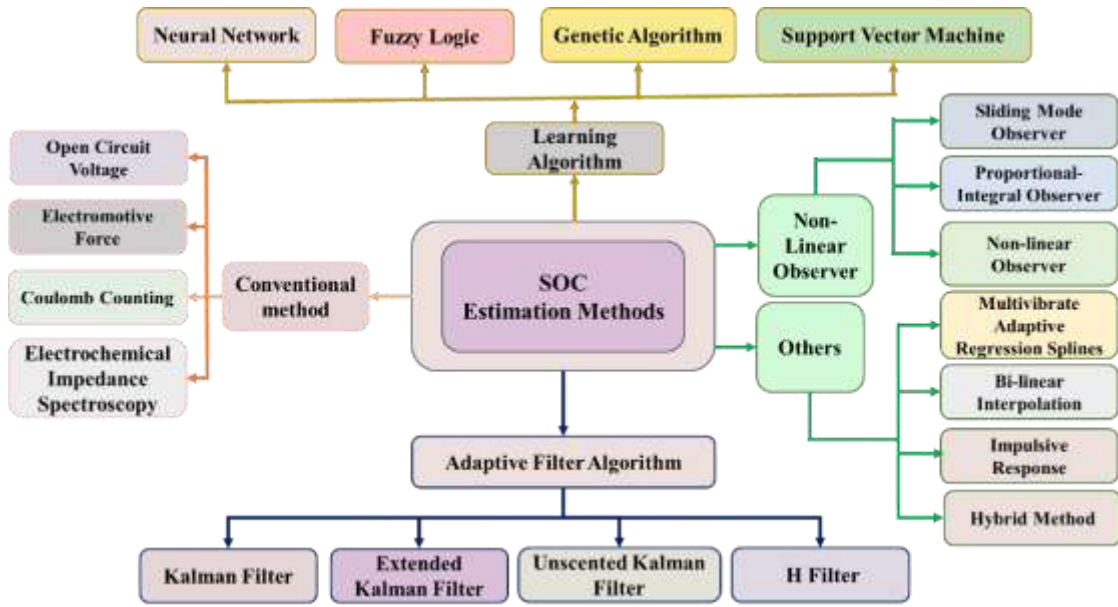


Figure 2.5 A classification of SOC estimation techniques

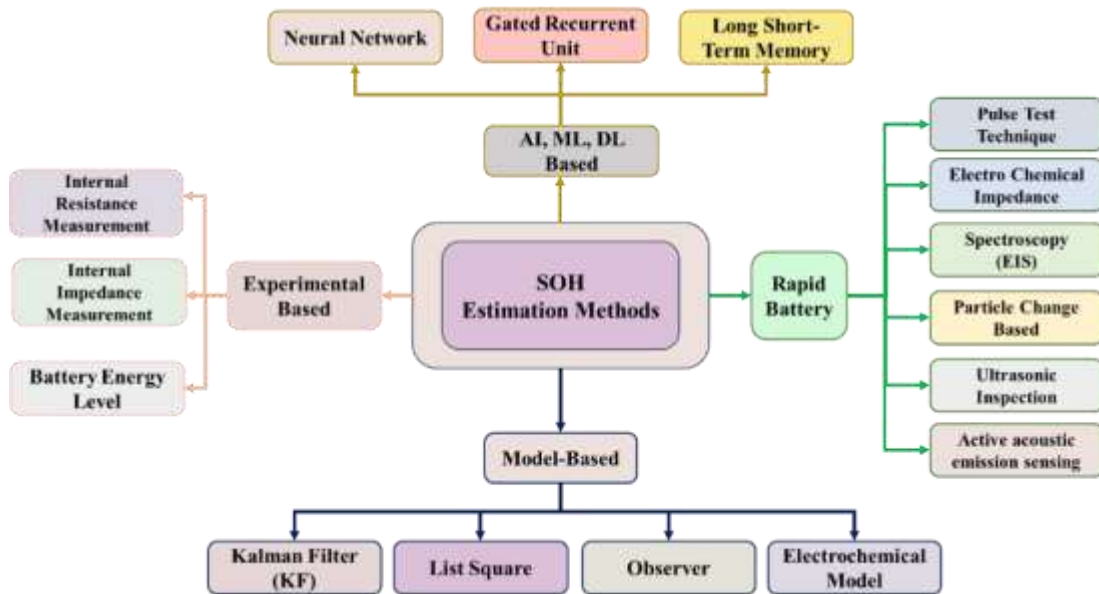


Figure 2.6 Classification of approaches for SOH estimation

The EVs safety and durability depend on the accurate SOH estimation of LIBs. SOH helps BMS to enhance charge/discharge processes and reduce deep cycling. This increases battery degradation by producing lithium plating, mechanical strain, and thermal growth, which may cause TR and

explosions. Reducing deep cycles, precise SOH estimation improves EV safety by reducing structural damage, internal short circuits, and TR. The SOH is defined as the ratio of the aged capacity to rated capacity. The SOH can be represented by Equation 2.3 [52].

$$SOH = \frac{C_{aged}}{C_{rated}} \times 100\% \quad (2.3)$$

Where C_{rated} initial rated/nominal capacity of the battery (specified by the manufacturer), C_{aged} the current degraded capacity of the battery at a specific point in its life cycle. The SOC typically ranges from 0% (fully discharged) to 100% (fully charged) and is crucial for predicting range in EVs. The SOE is known for the actual available energy output, considering voltage variations and efficiency losses, which is particularly relevant for dynamic EV drive cycles where power demands fluctuate [53]. SOH measures the battery's degradation relative to its initial condition, e.g., SOH = 80% at end-of-life, influencing both safety and economic viability in long-term ESS deployment. These states are interdependent; SOC and SOE degrade with SOH due to aging mechanisms, such as SEI growth, and environmental factors, e.g., temperature, can skew estimates by 10-20% [54].

2.5.2 Conventional and Model-based Approaches

Conventional and model-based approaches are widely used for the battery states estimation due to their simplicity and easy to implement in BMS [55]. The most common approaches are Coulomb counting (CC), open-circuit voltage (OCV) lookup tables, and estimation based on internal resistance. The CC calculates SOC by integrating the current over time, whereas the OCV-based methods calculate by using OCV-SOC relationships [56]. Although simple and computationally efficient, these methods suffer from the cumulative errors from sensors, sensitivity to initial conditions and reduced accuracy under dynamic conditions [57].

Model-based estimation techniques depend on mathematical representations to simulate battery behaviour under various operating conditions[58]. These include electrochemical, equivalent circuit, and physics-based models, it requires parameters such as voltage, current, and temperature as inputs. The ECMs approximates battery dynamics using the resistor and capacitor (RC) network and commonly combined with filtering algorithms such as family of Kalman Filters (KF) for improved estimation accuracy [59]. The KF is effective for the linear system with the Gaussian noise. The extended Kalman Filters (EKF) linearizes nonlinear models, making them applicable to a broader range of battery models. Unscented Kalman Filters (UKF) offer improved performance over EKF by better handling nonlinearities without the need for linearization [60]. Particle Filters (PF) utilize a set of particles to represent the probability distribution of the state, allowing for accurate estimation in highly nonlinear systems. These model-based methods are effective but require accurate parameter identification and are computationally intensive. It achieved SOC error of 0-10% under controlled conditions [59]. In contrast ECMs based on Butler-Volmer kinetics and porous electrode theory, provide deeper insights into ion diffusion and internal states. However, their computationally intensive limits direct real-time implementations in EV applications [61]. Overall, model-based methods are accurate and reliable, but they need precise parameter identification, reliable input data, and a lot of computing power, which may limit their deployment in embedded BMS platforms.

2.5.3 Data-driven and AI-based methods

Data-driven approaches estimate battery states using the historical and real time data without need of detailed physical models [62]. These methods are well suited for capturing highly complex and nonlinear battery behaviours under dynamic operating conditions. Machine learning (ML) techniques such as artificial neural networks (ANNs) are mostly used for the SOC and SOH

estimations by learning from historical data [63]. Support vector machines (SVMs) are applied for classification tasks, such as determining battery health state identification [64]. Advanced deep learning (DL) techniques like convolutional neural networks (CNNs) and long short-term memory (LSTM) networks have been employed for joint estimation of SOC, SOH, and SOE, offering high accuracy and robustness [65]. Reinforcement learning (RL) is emerging as a method for adaptive estimation and control in dynamic environments [66]. These AI-based methods can handle complex scenarios and provide real-time estimations. However, they require large, high quality training datasets, significant computational resources and may suffer from the limited interpretability compared to the physics models [67].

2.5.4 Challenges in Estimation Accuracy and Efficiency

Despite progress, maintaining the high estimation accuracy and computational efficiency under the real EV conditions remains challenging. Temperature variations can achieve 5-10% SOC error in model-based methods, whereas data-driven approaches are limited from overfitting and low accuracy as the battery ages below 80% [68]. EKF requires operations per cycle, limiting scalability in low power BMS, and DL models, such as BiLSTM, demand high training data volumes e.g., >10,000 cycles, which raises energy costs by 20-50% [69]. Nonlinear degradation and sensor noise further degrade efficiency, with fast-charging scenarios amplifying errors by 15% [70]. Recent literatures highlight hybrid estimation methods to balance accuracy below 2% RMSE and efficiency, with real-time latency less than 10 ms [71]. However, limitation remains in controlling environmental extremes, such as temperature and humidity variations, which can introduce drift. These gaps motivate proposed filter techniques and green AI integrations in this research work to enhancing predictive reliability for sustainable EV batteries. Data-driven approaches depend on historical data and ML algorithms to estimate battery states without relying

on explicit physical models [72]. These methods efficient in capturing the complex and nonlinear battery behaviours but require careful design to ensure accuracy, generalization, and real time feasibility.

2.6 ARTIFICIAL INTELLIGENCE IN BMS

AI technology has been integrated into EVs and has transformed the automotive sector [73]. It enhanced safer operation, improved driving experiences, increased energy utilization and overall system efficiency [74]. In BMS, AI improves battery state estimation, thermal management, fault detection, and lifetime predictions. Figure 2.7 illustrates the integration of AI across different EV domain. AI focus on developing intelligent machines with capable of learning behaviour, thought processes, and decision-making abilities [75]. ML techniques include reinforcement learning, supervised learning, and unsupervised learning to learn the complex pattern in EVs [76]. Whereas DL used neural networks such as CNNs and LSTM models to understand complex nonlinear battery state estimation tasks [77]. Beyond the battery application AI techniques such as natural language processing (NLP) and computer vision (CV) support vehicle communication, autonomous driving, intelligent human -machine interaction [78] [79] [80]. In Ev ecosystem, AI enhances battery performance, ensuring safety, and prolonging lifespan, in applications like EVs and renewable ESSs. Furthermore, it contributes in route optimization, range estimation, and vehicle to grid (V2G) energy management [81] [82] [83]. Overall, AI-driven BMS frameworks enable intelligent decision making, improved energy efficiency, enhanced operational safety in modern EVs

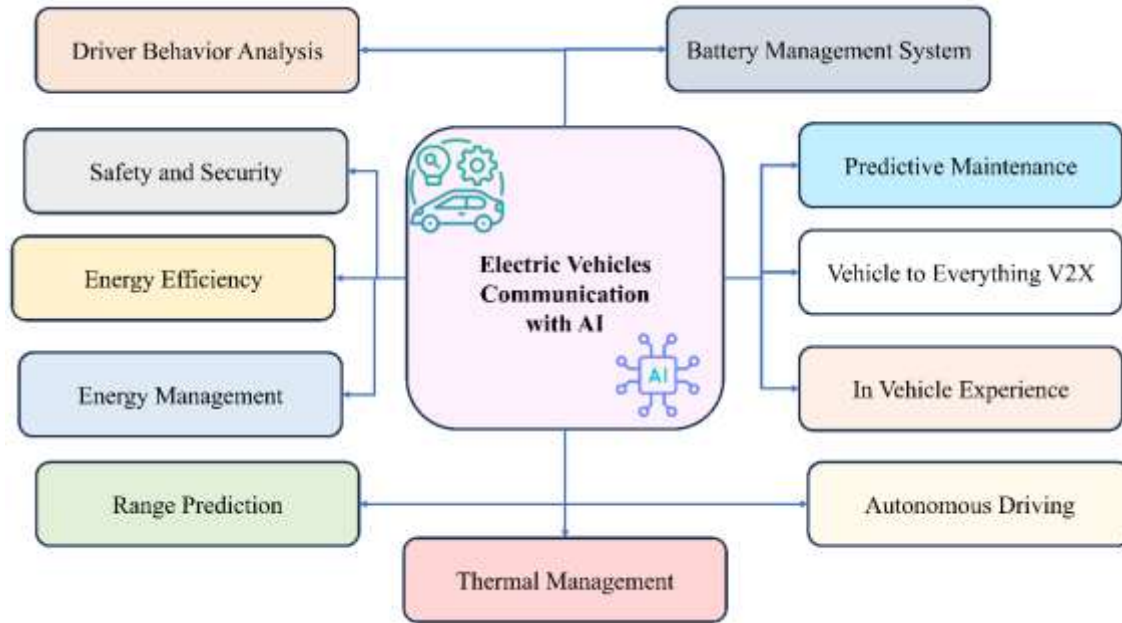


Figure 2.7 AI application in various areas of EVs

2.6.1 Green AI and Energy-Efficient Approaches

Recent AI research described under two contrasting paradigms: Red AI and Green AI. Red AI focuses on maximize performances such as accuracy and model capacity, by using large computational resources, big datasets, and extensive hyperparameter tuning[18], [84]. It often ignores energy costs, carbon emissions, and sustainability concerns related with heavy computational use. However, Green AI balance performance with efficiency by efficient model design, algorithms that achieve significant accuracy while reducing energy consumption, computational complexity, and environmental impact [19], [74]. In battery state estimation, including SOC, SOH, and SOE, Green AI approaches are relevant due to the need for real time implementation in embedded BMS platform. Traditional techniques, such as CC, ECMs, and family of KFs, often require strong physical modelling assumptions with high computational costs during capture complex nonlinearities, hysteresis, diffusion, and long-term degradation [85]. Adopting Green AI, it utilizes lightweight ML architectures, pruning, quantisation, compressed

models, and efficient hyperparameter optimisation to maintain accuracy while significantly reducing the computational and energy overhead [82], [86]. The advantages include reduced energy consumption in both training and inference, faster model execution suited for embedded systems in battery management, improved scalability for large deployments such as EV fleets and stationery ESSs, and alignment with sustainability goals. In conclusion, Green AI a well-balanced framework that aims to minimize energy consumption and computational complexity while preserving high estimation accuracy. It enhances rather than replaces conventional physics-based approaches, despite ongoing difficulties with model generalization, data accessibility, and realistic integration into embedded BMS platforms. It presents a workable route toward sustainable, scalable, and real-time BMS solutions for EV-ESSs by combining efficiency with reliable performance.

2.7 EFFECT OF ENVIRONMENTAL AND OPERATING CONDITIONS

Battery performance and state estimation accuracy are significantly influenced by external factors, including temperature variations, dynamic load profiles, and aging-related degradation. These factors influence electrochemical kinetics, internal resistance, and the OCV-SOC relationship, thereby posing significant challenges for model-based and AI-driven estimation frameworks. Environmental stressors accelerate degradation mechanisms, shorten lifetime and increase safety risk, especially in EVs applications where batteries experience wide ranges of thermal and operational conditions. Therefore, incorporation condition aware modelling and adaptive AI frameworks is essential to achieve reliable performance and accurate state estimation under real-world condition. This section examines the impact of key environmental and operating conditions on battery performance and estimation, highlighting strategies for condition-aware modelling and AI integration.

2.7.1 Temperature variations

Temperature variations significantly alter the electrochemical behaviour of LIBs, affecting ion mobility, reaction kinetics, and overall performance in EVs. High temperatures exceeding 40°C accelerate side reactions, such as SEI layer thickening and electrolyte decomposition, leading to 20-30% faster capacity loss and increased risks, including thermal runaway.

For example, P. Phogat et al. [87], examines that long exposure above 29°C degrades battery chemistry, reducing cycle life by up to 50% in hot climates. Conversely, low temperatures below 0°C increase internal resistance, slowing lithium-ion diffusion and reducing usable capacity by 20-30%, which manifests as a reduced EV range in winter conditions.

X. Zhang et al. [88] indicate that extreme temperatures exacerbate degradation in nickel-rich cathodes, e.g., NMC811, with cold weather causing up to 40% power drop due to viscosity increases in electrolytes. Optimal ranges 15-35°C minimise these effects, but real-world EV operation often deviates, highlighting the need for thermal management systems integrated with AI for adaptive state estimation [89].

Ma et al. [90] reviewed the impact of thermal stress and emphasised that operation above 45 °C accelerates parasitic reactions such as SEI growth, electrolyte decomposition, and transition-metal dissolution, while sub-zero operation increases lithium plating risk and irreversible capacity loss.

Leng et al. [91] experimentally investigated Li-ion cells under different temperatures and found that continuous cycling at 55 °C resulted in rapid capacity fade and internal resistance growth, while charging below 0 °C caused lithium plating, leading to permanent degradation. The authors quantified that cycle life could be reduced by more than 40% under prolonged high-temperature exposure compared to room temperature operation.

Wang et al. [92] analyzed thermal response under ambient variations (10–55 °C) and reported that at lower temperatures, the discharge capacity declined sharply due to sluggish lithium-ion

diffusion, whereas higher temperatures initially improved available capacity by reducing internal resistance but at the expense of faster aging. Their findings suggest that SOC and SOE estimation models must explicitly incorporate temperature dependencies for reliable performance.

Wang et al. [93] reviewed low-temperature effects on LIBs and highlighted that ionic conductivity and diffusion coefficients decline exponentially with decreasing temperature. They noted that charging below 0 °C increases the likelihood of metallic lithium deposition, which not only reduces SOH but also poses safety hazards. Such conditions complicate SOC estimation as the OCV–SOC relationship becomes distorted under polarization losses.

Schinagl et al. [94] studied impedance spectra at various temperatures and proposed Arrhenius-based compensation to account for the strong temperature sensitivity of EIS features. They concluded that using impedance without temperature correction can lead to significant estimation errors in SOH and internal resistance monitoring.

In summary, temperature significantly affects the performance, safety, and state estimation accuracy of LIBs. Low-temperature conditions limit ion transport, increase internal resistance, and induce lithium plating, while high-temperature environments accelerate degradation reactions, leading to rapid capacity fading and safety hazards. These thermal dependencies introduce significant challenges for accurately estimating SOC, SOE, and SOH in real-world EVs applications. Therefore, the development of temperature-aware modeling, thermal compensation strategies, and condition-aware AI frameworks is essential to ensure robust and reliable battery management under diverse operating environments.

2.7.2 Dynamic load profiles and drive cycles

Dynamic load profiles and standard drive cycles are used to replicate real-world driving conditions under controlled laboratory settings and battery research and EV testing. Unlike constant-current

(CC) cycling, drive cycles impose variable current profiles that reflect acceleration, deceleration, braking, and regenerative braking in actual EV operation. These transient conditions introduce polarization effect, voltage hysteresis, and impedance fluctuations, which not only accelerate certain degradation mechanisms but also complicate accurate estimation of SOC, SOE, and SOH. Common standardized cycles are the Urban Dynamometer Driving Schedule (UDDS), represents stop-and-go city driving with frequent accelerations and braking, causing shallow charge/discharge swings and SEI growth. Highway Fuel Economy Test (HWFET) reflects smoother highway driving with sustained discharge and thermal buildup under moderate current demand. Supplemental Federal Test Procedure (US06), represent stresses the battery with aggressive accelerations and high C-rate loads, it leading to lithium plating and reversible capacity losses. California Unified Cycle (LA92), which combines urban and suburban driving with more realistic dynamics than UDDS. Worldwide Harmonized Light Vehicles Test Procedure (WLTP), integrates urban, rural, and highway phases to provide a globally representative driving profile. Geslin et al. [95] demonstrated that dynamic discharge cycling can extend battery lifetime by up to 38% compared to constant-current cycling, as alternating current levels suppress lithium plating and distribute stresses more evenly across electrodes. However, aggressive cycles such as US06 generate sharp current peaks that increase reversible capacity loss (10–20%) due to impedance growth, although true structural degradation may remain limited under moderate dynamic conditions. The role of regenerative braking is also significant. Carefully managed regeneration can extend battery life by 10–15%, whereas uncontrolled high-current regeneration may accelerate lithium plating and SEI growth [96].

Fagihian et al. [97] reviewed advanced regenerative braking system architectures and emphasised that control strategies must be co-designed with BMS algorithms to ensure that short-term

efficiency gains do not compromise long-term cycle life. In a related study, a novel eco-regenerative braking system was proposed to adaptively regulate braking energy input, improving both energy efficiency and long-term durability of EV batteries [98].

The use of these cycles is important because they allow researchers to benchmark estimation algorithms for SOC, SOE, and SOH under controlled yet realistic operating conditions, to reveal degradation pathways such as SEI growth under urban stop-go driving, thermal buildup under highway operation, or lithium plating under aggressive cycles like US06. In summary, dynamic load profiles and drive cycles expose batteries to realistic stresses that accelerate certain degradation pathways while mitigating others. Condition-aware SOC/SOH estimation models must therefore integrate transient current responses, regenerative braking dynamics, and cycle-specific effects to remain robust in real-world EV applications.

2.7.3 Aging and Degradation Mechanisms

The LIBs undergo aging, which shows as capacity loss, increased impedance, and shortened cycle life. Aging is generally classified into calendar aging (during storage), and cycle aging (during charge/discharge operation), both are strongly influenced by temperature, depth of discharge (DoD), C-rate, and electrode chemistry. On the anode, degradation is mainly associated with solid electrolyte interphase (SEI) growth, which consumes active lithium and increases internal resistance.

Keil and Jossen [99] demonstrated that DoD and temperature, significantly accelerate SEI-related capacity fade in EV battery cells. At low temperatures, promote lithium plating, graphite anode, leading to irreversible capacity loss and safety risks.

Cathode degradation mechanisms depend on battery chemistry. Ni-rich layered cathodes (e.g., NMC811) suffer from microcrack formation, phase transitions, and oxygen release, which

accelerate impedance rise and transition-metal dissolution. Spinel (LMO) materials experience Mn dissolution, whereas olivine (LFP) materials offer better thermal stability but suffer from limited conductivity, which affects their long-term high-rate performance. Electrolyte decomposition, gas generation, and binder degradation further contribute to swelling, impedance growth, and capacity loss, particularly under dynamic load conditions. Han et al. [100] demonstrated that EV-representative cycling profiles (e.g., UDDS, WLTP) lead to faster degradation compared to simple constant-current cycling, underscoring the importance of drive cycle testing. Aging also alters the OCV-SOC relationship and impedance characteristics, reducing accuracy of models calibrated on fresh cells.

Bericibar et al. [101] emphasised that estimation models must adapt to parameter drift caused by aging, to maintain reliable SOC, SOE, and SOH prediction. In summary, degradation mechanism such as SEI growth, cathode microstructural instability, lithium plating, electrolyte decomposition, and dynamic cycling stresses reduces performance and complicate state estimation. Therefore, requirement of aging-aware and adaptive algorithms for reliable BMS operation are needed.

2.7.4 Strategies for Condition-Aware AI Estimation

As discussed in the previous subsections, environmental and operational variations such as temperature fluctuations, dynamic drive cycles, and aging-induced degradation significantly affect the accuracy of SOC, SOE, and SOH estimation. Conventional algorithms calibrated or trained under fixed operating conditions, often fail under temperature shifts, transient loads, and long-term degradation. To address this, condition-aware AI estimation strategies have been developed to improve robustness, while maintain the computational efficiency for BMS deployment. One approach is multi-condition training, where AI models are trained using datasets covering a wide range of temperatures, drive cycles, and operating profiles. Chemali et al. [102] demonstrated that

deep neural networks trained across multiple dynamic drive cycles outperformed conventional EKF methods for SOC estimation under transient loads.

Transfer learning (TL) and domain adaptation. These techniques allow models trained under one condition (e.g., room temperature or specific drive cycle) to adapt quickly to new conditions with minimal retraining. Tan et al. [103] demonstrated that TL significantly reduces the data requirement for accurate SOH prediction across different ambient temperatures.

Hybrid physics-AI framework combines ECMs with neural network for the residual learning, improved SOC estimation under variable temperatures and load conditions. Physics-informed machine learning (PIML) embeds electrochemical constraint into AI models for interpretability and reliability [104]. Finally, Green AI strategies are being explored to minimise the computational and energy costs of AI algorithms. Lightweight DL models, pruning, and quantisation techniques allow SOC and SOH estimators to be deployed efficiently on embedded BMS platforms without sacrificing accuracy. In summary, integrating multi-condition training, TL, hybrid modeling, and Green AI facilitate robust, adaptive, and energy-efficient battery state estimation for next-generation EV-BMS [105].

2.8 SUMMARY RESEARCH GAPS AND CONTRIBUTIONS

- Despite significant progress in LIBs materials, modeling, and AI-based BMS, several critical limitations remain. Most existing cathodes optimization studies focus on electrochemical performances improvements but insufficiently address scalable implementation and linked between material degradation mechanism (e.g., microcracks, lithium plating, impedance growth) and state estimation accuracy.

- Ni-rich layered cathodes such as NMC811, have high-energy density, however, their long-term structural instability and safety concerns are not adequately integrated into predictive state estimation framework.
- Model-based battery states estimation methods are validated only under traditional constant-current cycling and insignificant dynamic profiles, and their accuracy deteriorates under real-world conditions such as high temperature, high C-rates, and aggressive and real-time drive cycles. Limited studies have designed and modelled condition-aware, adaptive frameworks capable of maintaining robust performance across these scenarios.
- The traditional AI model in battery health estimations suffers from a limited dataset, especially under extreme conditions, poor generalisation across chemistries, high computational demand, and uncertain data privacy/security concerns. EV batteries operate under wide variations in temperature, drive cycles, and load conditions that accelerate degradation, yet most existing traditional models insufficiently capture these effects, limiting their accuracy and practical applicability in BMS.
- Recent studies rarely integrate AI-driven control strategies that consider environmental and operational factors such as temperature, dynamic drive cycles, and rapid battery degradation. Existing models often lack real-time drive cycle validation, highlighted the need for condition-aware frameworks that combine real-time monitoring with predictive control to enhance safety, reliability, and battery life.
- The energy, computational, and memory cost of AI-based estimators are not insufficiently addressed in the current literature. In EV BMS, lightweight and efficient algorithms are essential, but Green AI approaches, such as model simplification, parameters reduction, and lightweight architectures are still not yet fully explored for the embedded deployment.

2.9 OBJECTIVE OF THESIS

Based on the identified research and problem statement, the following objectives have been formulated for this research work:

- Synthesis and electrochemical analysis of layered/spinel/olivine/composite cathode material for rechargeable energy storage systems.
- To perform design and modelling for predicting the behaviour of energy storage systems.
- Development of an AI-based algorithm for battery health monitoring in BMS.
- To develop appropriate control strategies for analysing environmental factors for the future energy storage system.

CHAPTER 3

SYNTHESIS AND CHARACTERIZATION OF Ni-Rich NMC 811 CATHODE MATERIAL

3.1 INTRODUCTION

The LIBs are the dominant energy storage technology for EVs due to their high energy density, long cycle life, and efficiency. Among various cathode chemistries, Ni-rich layered oxides such as $\text{LiNi}_{0.8}\text{Mn}_{0.1}\text{Co}_{0.1}\text{O}_2$ (NMC811) are considered next-generation materials for EV applications due to their high specific capacity ($>200 \text{ mAh g}^{-1}$) and reduced dependence on cobalt. However, NMC811 poses significant challenges, including surface degradation, structural instability, cation mixing, and poor thermal stability, which limit its commercial adoption. To overcome these issues, researchers have investigated surface coatings, bulk doping, particle morphology control, and synthesis optimization to improve performance. This chapter focuses on the solid-state route synthesis of NMC811, its structural and morphological characterization.

3.2 LITERATURE REVIEW OF CATHODE MATERIALS

3.2.1 Ni-Rich Cathode Materials NMC811

Layered transition-metal oxides such as $\text{LiNi}_x\text{Mn}_y\text{Co}_z\text{O}_2$ (NMC) and $\text{LiNi}_x\text{Co}_y\text{Al}_z\text{O}_2$ (NCA) dominate current EV batteries due to their high capacity and voltage. Ni-rich variants (NMC811) offer superior capacity but are prone to structural degradation, micro-crack formation, and side reactions with electrolytes. LCO, although historically important, suffers from cobalt cost and safety issues, which limit large-scale EV applications.

Wang et al. [106] conformal nano- Li_2S coatings on NMC811 particles significantly enhance cycle life and interfacial stability by forming a protective sulphur-rich interface that reduces parasitic

electrolyte reactions. It improves in capacity retention and rate capability for coated materials compared to bare NMC811. The scalability, thermal stability, and manufacturing compatibility of sulphur-based coating require further investigation.

Colalongo et al. [13] used operando XRD and XAS to study low-level Zr doping in NMC811 and found that it suppresses harmful phase transition, reduces transition-metal dissolution, and improves cycling stability. However, the impact of dopant distribution on to pack-level performances and BMS diagnosis remains unexplored.

Laakso et al. [107] identified microcracking, transition-metal dissolution, and coupled electrolyte decomposition as key degradation mechanisms in NMC811/Si-graphite pouch cells with strong temperature dependence. However, it did not link these findings to predictive BMS control strategies.

Qu et al. [108] demonstrated that a fast-charging profile accelerates nanoscale crack formation and impedance growth in NMC811. This work links specific charge rates and SOC windows of nonlinear increases during mechanical damage and impedance rise. These degradation maps are not yet integrated into system-level thermal/design models and AI predictors for real-time BMS interventions, precisely the combination of synthesis-aware testing and modelling.

Si et al. [109] studies developed machine-learning models to predict cycle life for NMC-based cells using laboratory time-series and early cycling features, demonstrating that data-driven approaches can give robust cycle-life forecasts when sufficiently rich datasets are available. Most ML models are trained on limited, homogeneous datasets and rarely incorporate mechanistic features.

In summary, significant development has been made in understanding the degradation mechanism and developing a data-driven prediction model for Ni-rich cathodes. This critical gap remains in

linking material level insights with system level modeling and real-time BMS diagnostics. Integrating mechanistic understanding, advanced modeling, and AI-based estimation is therefore essential to enable reliable predictive and condition-aware BMS for next-generation EV-ESSs.

3.3 MATERIALS AND METHODS

Lithium hydroxide monohydrate ($\text{LiOH}\cdot\text{H}_2\text{O}$, $\geq 99\%$), nickel sulfate heptahydrate ($\text{NiSO}_4\cdot 7\text{H}_2\text{O}$, 98%), manganese sulfate monohydrate ($\text{MnSO}_4\cdot\text{H}_2\text{O}$, 98%), cobalt sulfate heptahydrate ($\text{CoSO}_4\cdot 7\text{H}_2\text{O}$, 98%), citric acid ($\text{C}_6\text{H}_8\text{O}_7$, $\geq 99\%$), sodium hydroxide (NaOH, pellets), and ethylene glycol (EG, $\geq 99.5\%$) were used as starting materials. All chemicals were of analytical grade and used without further purification. DI water was used during synthesis.

3.3.1 Selection of NMC811 as a Layered Cathode

NMC811 was selected for its high nickel content, which gives high specific capacity, cost reduction, operating voltage, and reduced cobalt dependency. However, the material requires careful synthesis for cation mixing, surface instability, and thermal runaways.

3.3.2 Solid-State Reaction Route for Synthesis

The solid-state method was chosen for its simplicity, scalability, and suitability for producing phase-pure NMC811 powders. Stoichiometric amounts of precursors such as $\text{NiSO}_4\cdot 7\text{H}_2\text{O}$, $\text{MnSO}_4\cdot\text{H}_2\text{O}$, $\text{CoSO}_4\cdot 7\text{H}_2\text{O}$ and Ni:Mn:Co ratio 0.8:0.1:0.1 are mixed, ball-milled, and calcined at controlled temperatures, typically 750–850 °C, in an oxygen-rich atmosphere.

3.3.3 Experimental Procedure and Process Flow

Stoichiometric amounts of $\text{NiSO}_4\cdot 7\text{H}_2\text{O}$, $\text{MnSO}_4\cdot\text{H}_2\text{O}$, and $\text{CoSO}_4\cdot 7\text{H}_2\text{O}$ were weighed to achieve the Ni:Mn:Co molar ratio of 0.8:0.1:0.1. The salts were dissolved in a mixed solvent of ethylene glycol (EG) and deionised water in a 2:1 ratio (v/v) under continuous stirring. The pH of the

solution was adjusted to 11–11.5 by the dropwise addition of NaOH solution to precipitate a homogeneous hydroxide precursor. A stoichiometric amount of LiOH·H₂O with 5–10% excess lithium to compensate for volatilization during high-temperature treatment) was introduced into the precursor mixture. Citric acid was added as a chelating agent to ensure uniform distribution of cations. The mixture was thoroughly stirred and dried at 80–100 °C to remove excess water and solvent. The dried powder was lightly ground using an agate mortar and pestle to obtain fine powder. The precursor powder was first pre-heated at 450 °C for 5 h in air to decompose sulfates, hydroxides, and organic residues. The intermediate powder was reground to ensure homogeneity. The pre-calcined powder was pelletized and then sintered at 750–850 °C for 10–12 h in an oxygen-rich atmosphere to promote crystallization into the layered α -NaFeO₂ type structure (R-3m space group). After sintering, the furnace was allowed to cool naturally to room temperature. The synthesis procedure of NMC811 via solid state reaction route is schematically represented in Figure 3.1.

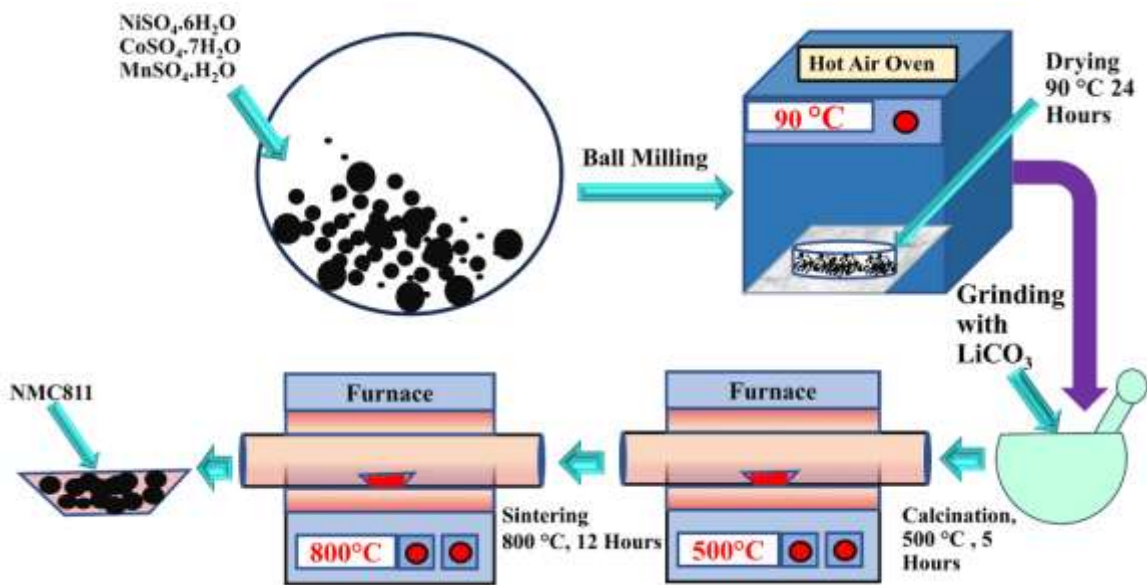


Figure 3.1 Schematic synthesis diagram of NMC811 via solid state reaction route

3.4 CHARACTERIZATION TECHNIQUES

The crystal structure of the synthesized samples was analyzed using X-ray diffraction (XRD) with a Rigaku Ultima IV diffractometer equipped with Cu K α radiation and operated at an accelerating voltage of 40 kV. Fourier transform infrared (FTIR) measurements were carried out using a NICOLET-380 spectrometer to examine the vibrational features and chemical bonding present in the materials. Surface morphology and microstructural features were investigated using a Zeiss Gemini SEM 500 scanning electron microscope. To evaluate the structural, morphological, and electrochemical properties of the synthesised NMC811 cathode material, a range of characterization techniques was employed. These methods provide complementary insights into the thermal stability, chemical bonding, crystallographic structure, microstructure, and electrochemical performance of the material.

3.5 RESULTS AND DISCUSSION

3.5.1 Thermal Stability and Phase Formation Analysis

TGA was used to study the thermal decomposition behavior and weight loss profile of the precursor mixture during heating. By measuring weight change as a function of temperature, TGA provides valuable information about phase formation, volatile removal, and stability windows. For NMC811, TGA confirmed the multi-stage decomposition process and the temperature ranges suitable for calcination, as shown in Figure 3.2. TGA of the synthesized precursor exhibited a three-stage weight loss pattern, with decreases of 8.106%, 22.476%, and 30.267%, resulting in a cumulative weight loss of 60.843%. The first stage corresponds to the evaporation of absorbed water and residual solvents, the second stage to decomposition of lithium carbonate and transition metal hydroxides, and the third stage to the formation of the layered NMC811 phase.

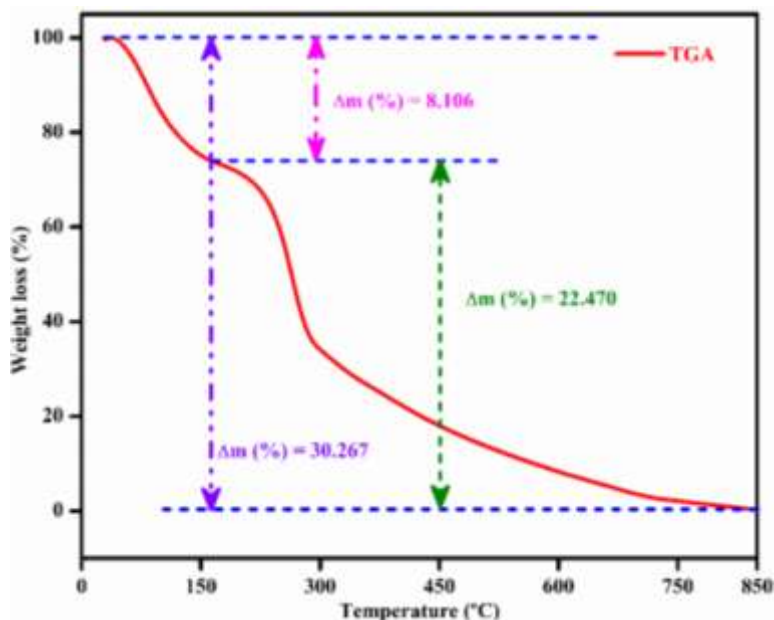


Figure 3.2 Thermogravimetric analysis of synthesized NMC811 sample

These results confirm the progressive decomposition and crystallisation behaviour of the solid-state synthesised sample, consistent with earlier reports on Ni-rich cathode synthesis.

3.5.2 Structural Properties

FTIR spectroscopy was employed to identify the functional groups and bonding interactions within the synthesized sample. The technique works by measuring the absorption of infrared radiation at specific wavelengths corresponding to different vibrational modes of bonds. In NMC811, FTIR spectra reveal the characteristic metal–oxygen (M–O) stretching vibrations, confirming lattice formation, along with additional peaks due to surface carbonate and hydroxyl impurities, as shown in Figure 3.3. FTIR spectra of NMC811 confirmed the presence of characteristic functional groups. Peaks observed between $490\text{--}535\text{ cm}^{-1}$ correspond to metal–oxygen (M–O) stretching vibrations, verifying the formation of the transition metal oxide lattice. Additional peaks at $744\text{--}1065\text{ cm}^{-1}$ correspond to C–O and C=O vibrations, which likely originate from residual carbonate species resulting from exposure to air during preparation.

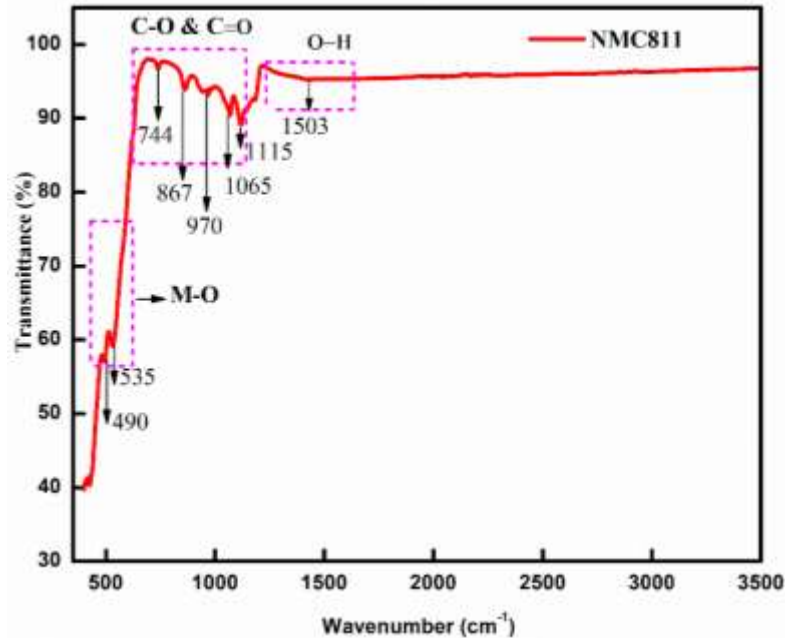


Figure 3.3 FTIR spectra of the synthesized NMC811

A broad band at 1503 cm^{-1} was attributed to O–H stretching vibrations, indicative of surface hydroxyl groups. These findings confirm the formation of the layered oxide structure with minor surface contamination.

3.5.3 X-ray Diffraction (XRD) Analysis

The XRD pattern of the synthesized $\text{LiNi}_{0.8}\text{Mn}_{0.1}\text{Co}_{0.1}\text{O}_2$ cathode material is presented in Figure 3.4. The obtained diffraction pattern confirms that the synthesized material exhibits a layered $\alpha\text{-NaFeO}_2$ type hexagonal structure with space group $R\bar{3}m$. The observed diffraction peaks match well with the standard JCPDS card No. 82-1495, indicating the successful formation of the NMC811 phase with good crystallinity. The major diffraction peaks observed at approximately 18.7° , 36.7° , 38.2° , 44.5° , 50.7° , 58.6° , 64.7° , and 68.9° correspond to the (003), (101), (006)/(102), (104), (105), (107), (018), and (113) crystallographic planes, respectively. Among these peaks, the (003) reflection is particularly significant because it represents the periodic ordering of lithium layers in the layered structure.

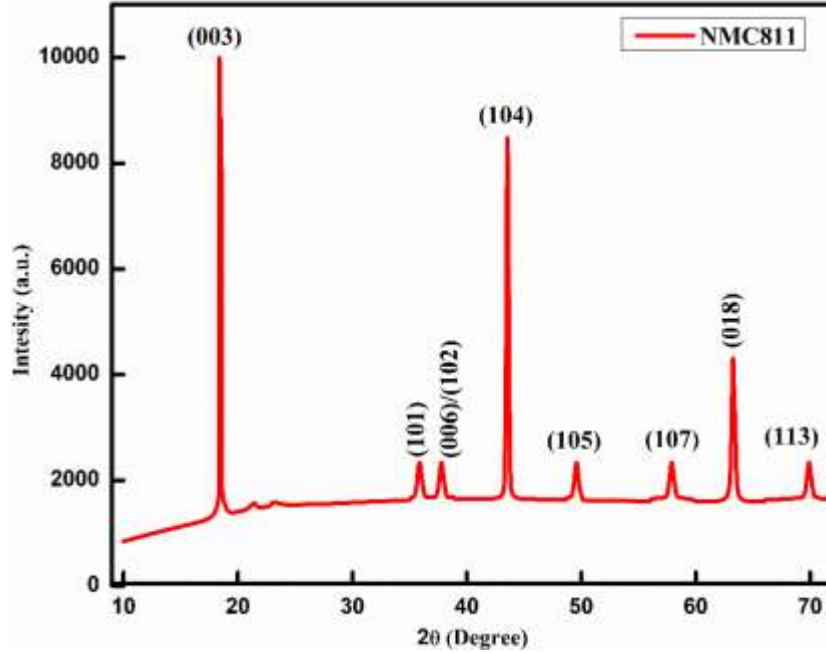


Figure 3.4 X-ray diffraction of pattern of NMC811 sample

A strong (003) peak indicates the formation of a well-defined layered structure where lithium ions occupy the lithium layers while transition metal ions (Ni, Mn, and Co) occupy the transition metal layers. This layered configuration is essential for facilitating efficient lithium-ion intercalation and de-intercalation, which directly influences the electrochemical performance of lithium-ion batteries. The average crystallite size of the synthesized material was estimated using the Scherrer formula, as expressed in equation 3.1,

$$D = \frac{K\lambda}{\beta \cos\theta} \quad (3.1)$$

Where, D crystallite size, K shape factor (≈ 0.9), λ X-ray wavelength (Cu-K α = 0.15406 nm), β full width at half maximum (FWHM) of the diffraction peak, θ Bragg diffraction angle. Using the dominant diffraction peak, the average crystallite size was calculated to be approximately 22 nm, indicating that the synthesized material consists of nanocrystalline particles. Nanostructured cathode materials are advantageous because they provide shorter lithium-ion diffusion pathways and a larger active surface area, which can enhance the electrochemical kinetics of the battery.

The lattice parameters of the hexagonal structure were calculated using Bragg's law and the hexagonal lattice relation, as expressed in equation 3.2.

$$n\lambda = 2d\sin\theta \quad (3.2)$$

This equation 3.3 is used to determine the interplanar spacing d from the diffraction angle.

$$\frac{1}{d^2} = \frac{4}{3} \frac{(h^2 + hk + k^2)}{a^2} + \frac{l^2}{c^2} \quad (3.3)$$

where h, k, l are the Miller indices of the crystal plane, a is the lattice parameter in the basal plane, c is the lattice parameter along the vertical axis. Using the (003) and (104) reflections, the lattice parameters were estimated as: $a \approx 2.86 \text{ \AA}$, $c \approx 14.2 \text{ \AA}$. The ratio between these parameters is $c/a \approx 4.97$. A c/a ratio greater than 4.9 confirms the presence of a stable layered hexagonal structure, which is favourable for lithium-ion diffusion and electrochemical stability. The degree of cation mixing between Li^+ and Ni^{2+} ions was evaluated using the intensity ratio of the (003) and (104) peaks. $\frac{I_{003}}{I_{104}}$. For well-ordered layered cathode materials, the ratio should satisfy $I_{003}/I_{104} > 1.2$. A higher value of this ratio indicates low cation mixing, meaning that nickel ions do not significantly occupy lithium sites. This ensures open lithium diffusion channels, which improve battery capacity and cycling performance. The structural ordering of the synthesized NMC811 cathode was further evaluated using the R-factor, defined as $R = (I_{006} + I_{102})/I_{101}$. The calculated R value was 0.41, indicating a well-ordered layered hexagonal structure with minimal structural disorder. A low R-factor confirms that the synthesised NMC811 possesses good structural ordering and minimal distortion in the layered lattice.

In addition to the main diffraction peaks, minor impurity peaks corresponding to Li_2CO_3 and Li_2O were observed. These impurities commonly appear in nickel-rich layered cathodes due to surface reactions of residual lithium species with atmospheric CO_2 and moisture during sample handling or storage. The intensity of these impurity peaks is relatively low, indicating that the synthesized

material is predominantly phase pure. The XRD analysis confirms that the synthesized material exhibits a highly crystalline layered α -NaFeO₂ structure with space group $R\bar{3}m$. The calculated lattice parameters, favorable c/a ratio, high I_{003}/I_{104} value, and low R-factor collectively indicate good structural ordering, minimal cation mixing, and stable layered architecture. These structural characteristics are essential for enabling efficient lithium-ion diffusion, high specific capacity, and improved cycling stability, making the synthesized NMC811 material suitable for lithium-ion battery cathode applications.

3.5.4 Morphological and Elemental Analysis

SEM was employed to investigate the surface morphology and particle microstructure of NMC811, as shown in Figure 3.5. High-resolution micrographs revealed particle size, grain growth, and agglomeration behaviour. The morphology is critical to electrochemical performance, as it influences lithium-ion transport pathways and electrode–electrolyte interfacial contact. SEM micrographs revealed that the NMC811 particles are agglomerated with a relatively uniform distribution. The average grain size of powder particles was estimated at ~170 nm, while dense sintered pellets exhibited an average grain size of ~410 nm. Such dense morphology is beneficial for enhanced ionic conductivity but may also contribute to reduced electrode–electrolyte interfacial contact. EDX analysis confirmed the presence of Ni, Mn, and Co, validating the expected stoichiometry of the synthesised NMC811 composition. The EDS elemental mapping was performed to evaluate the spatial distribution of TM in the synthesis of NMC811. This elemental mapping confirms the presence of Ni, Mn, Co, and O, with all elements uniformly distributed across the analysed region.

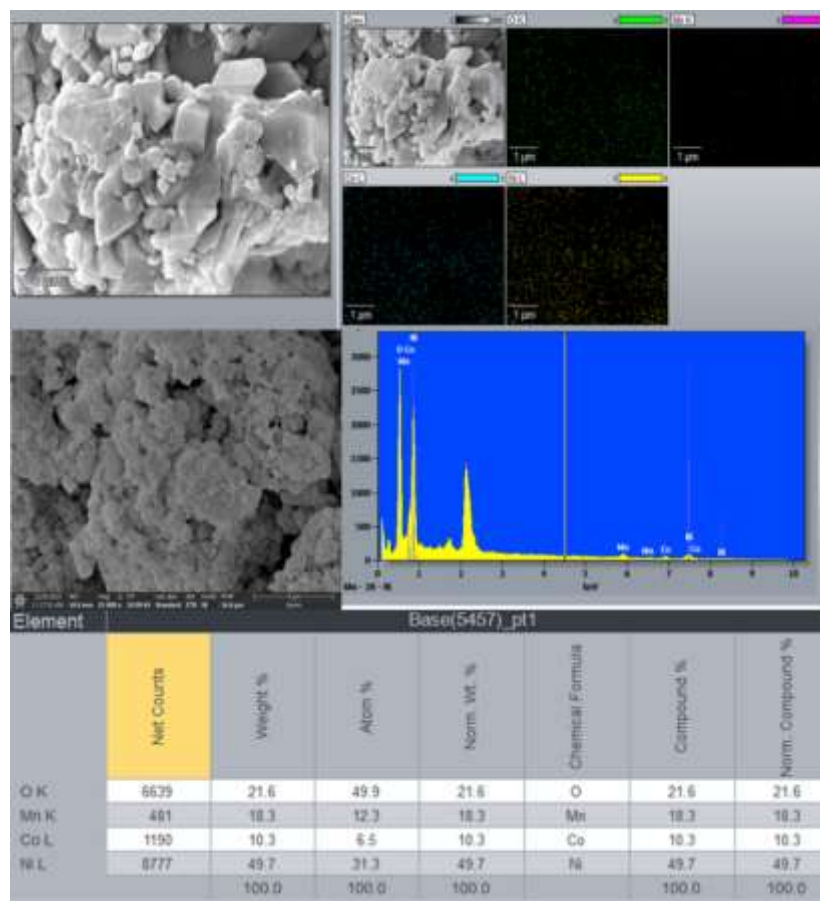


Figure 3.5 SEM images and EDX spectra of the NMC811 sample

This homogenous distribution indicates effective precursor mixing and successful formation of a single-phase layered oxide structure. Quantitative EDS investigation shows that the atomic (%) of around 31.3% Ni, 12.3% Mn, and 6.5% Co. When adjusted, the transition-metal ratio is very close to the theoretical stoichiometry of $\text{LiNi}_{0.8}\text{Mn}_{0.1}\text{Co}_{0.1}\text{O}_2$. The lack of extra impurity peaks in the spectrum is more proof that the synthesized cathode material is pure in terms of its composition. These results show that the solid-state synthesis method worked well to make a homogeneous and compositionally accurate NMC811 layered oxide that is good for high-performance LIBs use. The characterized results confirm the successful synthesis of the single-phase layered NMC811 with crystallinity, thermal stability, and uniform morphology.

3.6 CONCLUSION

This chapter presented the synthesis and characterization of the Ni-rich layered cathode material NMC811, which was successfully synthesized via the solid-state reaction route. TGA revealed a three-step decomposition process leading to phase formation with total weight loss of 60.8%, confirming the multistage precursor decomposition and validating the optimized calcination temperature range of 750-850°C for stable single-phase formation. The XRD confirm the formation of the hexagonal α -NaFeO₂ layered structure (R-3m space group) with the good crystallinity. However, the FTIR analysis further confirmed metal oxygen lattice formation through the characteristics vibrational bond in the 490-535cm⁻¹ range. The morphological analysis revealed that the particles are agglomerated and have a particle size of 170-410nm, demonstrating controlled microstructure development. EDS investigation shows that the atomic percentages are around 31.3% Ni, 12.3% Mn, and 6.5% Co. When adjusted, the transition-metal ratio is very close to the theoretical stoichiometry of LiNi_{0.8}Mn_{0.1}Co_{0.1}O₂. In summary, this characterization confirms that the Ni-rich layered cathode material NMC811 was successfully synthesized via the solid-state reaction route with structural stability, uniform composition, and microstructure. Detailed electrochemical tests (CV, GCD, EIS), which are essential for evaluating practical performance, remain as part of future work.

CHAPTER 4

DESIGN AND MODELLING OF AI-BASED APPROACH FOR STATE ESTIMATION OF LITHIUM-ION BATTERY

4.1 INTRODUCTION

The LIBs are extensively used in EVs and grid storage due to their high energy density, long cycle life, and low self-discharge. However, inaccurate estimation of SOC and SOE can lead to overcharging, thermal runaway, and even explosions, posing safety risks. Conventional model-based and data-driven approaches for SOC/SOE estimation face challenges such as complex mathematical design, large dataset requirements, and high computational cost. While AI models, including LSTM and GRU, improve estimation accuracy, they demand significant training time, hyperparameter tuning, and energy consumption, limiting their contribution to Green AI. To address these challenges, this work proposes a novel filtering technique (FT) based on sliding windows and supervised learning, which reduces dataset redundancy while preserving data integrity. By integrating FT with CNN-BiLSTM models, the framework achieves accurate SOC/SOE estimation, reduces training time, improves computational efficiency, and achieves energy savings.

4.2 DATA-DRIVEN APPROACHES FOR STATE ESTIMATION OF LIBs

4.2.1 Convolutional Neural Network Architecture

The CNN developed by LeCun et al. [110], is an efficient feed-forward deep learning technique for pattern recognition and feature extraction.

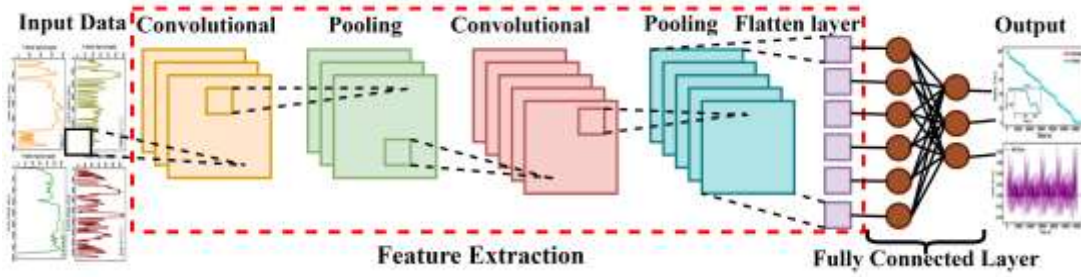


Figure 4.1 1D-CNN model structure for feature extraction

Through layer-by-layer convolution and pooling processes, the CNN uses a set of filters to extract the topological properties buried within the data. The CNN may use several parameters to extract the input's spatial properties and combine them to produce high-level features. These features are subsequently supplied into the fully connected layer when used for further classification or regression. However, CNN is well-known for its effectiveness during dealing with 1D data structures [111]. In this study, 1D convolution is used to capture the spatial characteristics of battery variables. A convolutional layer is added for the input data to proceed to the subsequent layer, as shown in Figure 4.1 and expressed in equation 4.1.

$$h_k = \sigma_{cnn}(W_{cnn} * X_k + b_{cnn}) \quad (4.1)$$

Where, σ_{cnn} , b_{cnn} , W_{cnn} , X_k , * are activation function, bias, weight, input signal, and discrete convolution, respectively.

4.2.2 Long Short-Term Memory Architecture

According to the latest developments in ML techniques, RNNs are one of the most advanced algorithms for classification issues applied to sequential data. A specific type of ANN, known as an RNN, utilises loops of feedback to store previous input data as activation. Furthermore, it can establish a connection between the network's previous and present data. However, RNNs can also learn the lengths of random dimensions; still, they face difficulties with gradient explosion and vanishing [112]. This can potentially be addressed by using the specific variant of RNN that

Hochreiter and Schmidhuber (1997) developed in which the RNN cell is swapped and exchanged for a gated cell named a Long Short-Term Memory network. Figure 4.2. depicts the fundamental architecture of a single LSTM network. A memory cell, shown by C_t with self-loops, is part of an LSTM network and stores the temporal information imprinted on the cell's state. Forget gate f_t [0, 1], input gate i_t [0, 1], and output gate O_t [0, 1] are the three gates that regulate the flow of information in the network.

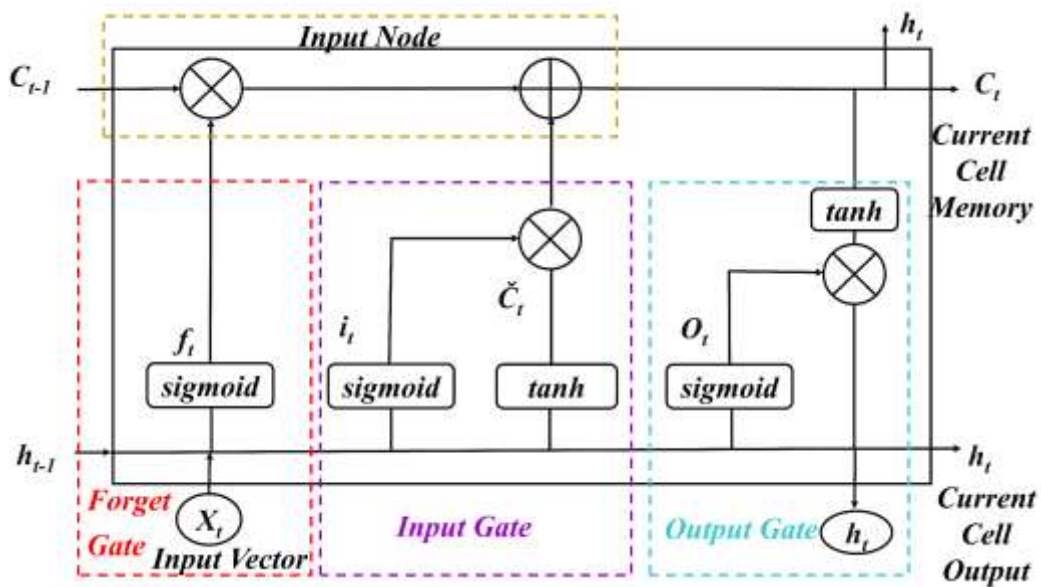


Figure 4.2 The internal structure of an LSTM unit

To reduce the possibility of errors, the network learns what has to be recollected and when to enable reading and writing. The Forget gate determines which data from the previous memory cell state has expired and must be erased. The input gate changes the memory cell state by choosing the relevant data from the candidate state C_t .

The memory cell data is filtered by the output gate so that the model only considers the essential data needed to assess. Following are the expression used to calculate each gate value, equation (4.2-4.3).

$$\begin{aligned}
f_t &= \text{sigmoid}(W_f[X_t, y_{(t-1)}] + b_f) \\
i_t &= \text{sigmoid}(W_i[X_t, y_{(t-1)}] + b_i) \\
\left. \begin{aligned}
c_t^* &= \text{sigmoid}(W_c[X_t, y_{(t-1)}] + b_c) \\
o_t &= \text{sigmoid}(W_o[X_t, y_{(t-1)}] + b_o)
\end{aligned} \right\} \quad (4.2)
\end{aligned}$$

$$\begin{aligned}
C_t &= C_{(t-1)} \odot f_t + c_t^* \odot i_t \\
\left\{ \begin{aligned}
y_t &= o_t \odot \tanh(C_t)
\end{aligned} \right\} \quad (4.3)
\end{aligned}$$

Weight matrices are denoted by $W_{[i, f, c, o]}$ while the bias vectors are denoted by $b_{[i, f, c, o]}$. Using the following equations, the memory cell value c_t^* and output (o_t) of the network is determined. “ \odot ” is the Hamard product.

4.2.3 Bidirectional Long Short-Term Memory Architecture

Schuster and Paliwal [113] developed bidirectional RNN, a kind of RNN that uses past and future input data sequences to train the network. The input data is processed using two linked layers, and each layer performs operations in reversed time step direction. The outcomes can be merged using various merging strategies. In BiLSTM, one layer processes data in the same direction as the sequence, while the second layer processes data in the opposite direction. The BiLSTM shows more accurate results than unidirectional LSTM in some applications, including battery management systems [114]. The unfolded BiLSTM network topology is depicted in Figure 4.3. BiLSTM has two hidden layers: forward and backward LSTM, coupled with the same output layer. The forward LSTM layer output \vec{h}_t is calculated by BiLSTM independently, and then \overleftarrow{h}_t every time step t is similarly concatenated through BiLSTM.

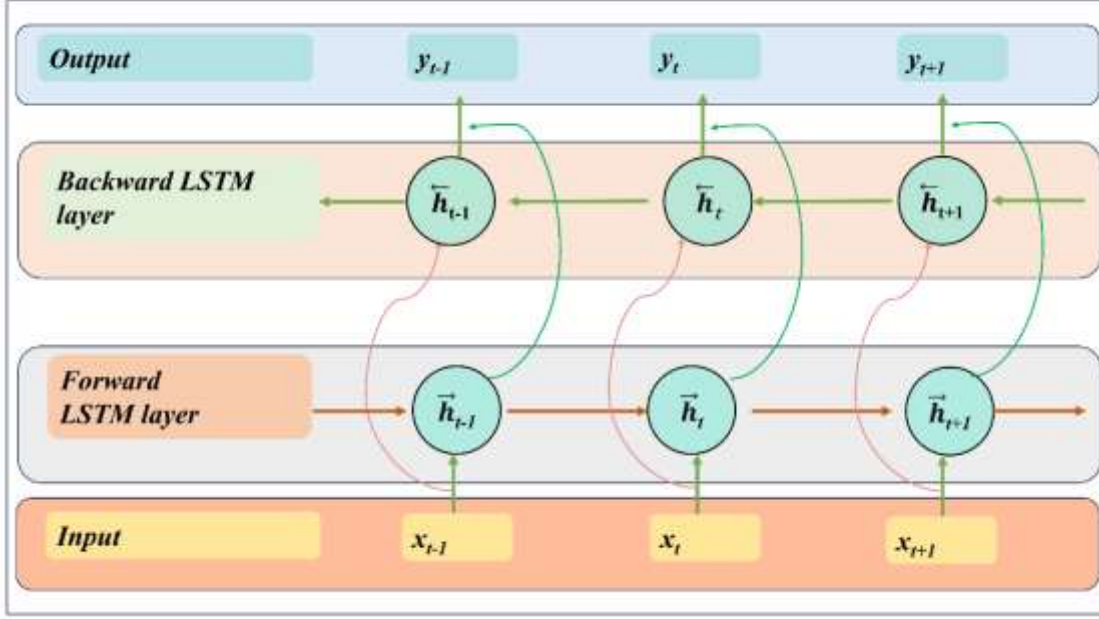


Figure 4.3 Bidirectional LSTM model structure

The BiLSTM process is represented in equations 4.4-4.6.

$$\vec{h}_t = f(X_t, \vec{h}_{(t-1)}; \vec{\Theta}_{BiLSTM}) = \begin{cases} \vec{f}_t = \text{sigmoid}(\vec{W}_f[X_t, \vec{h}_{(t-1)}] + \vec{b}_f) \\ \vec{i}_t = \text{sigmoid}(\vec{W}_i[X_t, \vec{h}_{(t-1)}] + \vec{b}_i) \\ c_t^* = \tanh(\vec{W}_c[X_t, \vec{h}_{(t-1)}] + \vec{b}_c) \\ \vec{o}_t = \text{sigmoid}(\vec{W}_o[X_t, \vec{h}_{(t-1)}] + \vec{b}_o) \\ \vec{c}_t = \vec{f}_t \odot C_{(t-1)} + c_t^* \odot \vec{i}_t \\ \vec{h}_t = \vec{o}_t \odot \tanh(\vec{c}_t) \end{cases} \quad (4.4)$$

$$\bar{h}_t = f(X_t, \bar{h}_{t-1}; \bar{\Theta}_{BiLSTM}) = \begin{cases} \bar{f}_t = \text{sigmoid}(\bar{W}_f[X_t, \bar{h}_{(t-1)}] + \bar{b}_f) \\ \bar{i}_t = \text{sigmoid}(\bar{W}_i[X_t, \bar{h}_{(t-1)}] + \bar{b}_i) \\ c_t^* = \tanh(\bar{W}_c[X_t, \bar{h}_{(t-1)}] + \bar{b}_c) \\ \bar{o}_t = \text{sigmoid}(\bar{W}_o[X_t, \bar{h}_{(t-1)}] + \bar{b}_o) \\ \bar{c}_t = \bar{f}_t \odot C_{(t-1)} + c_t^* \odot \bar{i}_t \\ \bar{h}_t = \bar{o}_t \odot \tanh(\bar{c}_t) \end{cases} \quad (4.5)$$

$$y_t = W_{\vec{h}_y} \vec{h}_t + W_{\bar{h}_y} \bar{h}_t + b_y \quad (4.6)$$

$\overrightarrow{W_f}$ shows the weight from the forward LSTM layer to the output. W_b represents the weight from the backward LSTM layer to the output layer. The bias at the output layer is explicitly stated as " b_y ".

4.2.4 Stacked Bidirectional LSTM Network

This study aims to employ a stacked bidirectional LSTM network, illustrated in Figure 4.4, to capture past and future sequential data across different directions and time intervals. The key role of our research is the proposal of a stacked BLSTM model, which allows for deeper and more accurate modeling by stacking the hidden layers. This model is applied as a deep learning technique for classification. The efficiency of neural networks in a wide range of challenging prediction problems is commonly known to describe their depth [115]. The input vector is $\psi t = [V(t), I(t), T(t)]$ where $V(t)$, $I(t)$, and $T(t)$ denote the voltage, current, and temperature of the battery at time interval t in this proposed approach. At each time interval, the data is converted into an image and then fed into a 2D-CNN model to extract features. Once the convolutional layers have extracted the features, SBLSTM is used to train the feature maps by taking them as input. Lastly, the proposed technique estimated SOC at time t . The model includes two hidden layers, each with 25 nodes, using Bi-LSTM. Additionally, a fully connected (FC) layer and an output layer have been incorporated to enable the linear translation of the Bi-LSTM layers' hidden state into a single SOC output value. The output layer employs the rectified linear unit (ReLU) activation function. Furthermore, two stacked layers are used. As the model loss during each forward propagation, the mean square error (MSE) is determined by comparing the estimated SOC value with the true SOC value, as expressed in equation 4.7 [116].

$$Loss = \frac{1}{m} \sum_{t=1}^m |(\hat{SOC}(t) - SOC(t))|^2 \quad (4.7)$$

Where, the measurement capacity $SOC(t)$, estimated capacity $(\hat{SOC}(t))$, and m indicates the sample number.

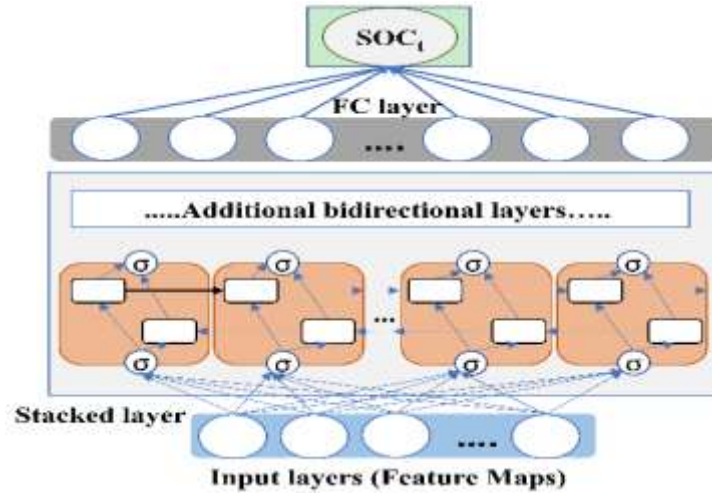


Figure 4.4 Stacked bidirectional LSTM model structure

4.2.5 Challenges in Accurate SOC/SOE Estimation

Accurate estimation of SOC and SOE in lithium-ion batteries remains challenging due to several factors. Model-based approaches often require complex mathematical formulations that lack adaptability across varying operating conditions. Data-driven methods, while capable of handling large datasets, face limitations such as computational burden, training inefficiency, and dependency on dataset quality. The presence of redundant or closely grouped values in battery datasets further increases modeling complexity and training time. Advanced AI models, including RNN, LSTM, and GRU, can enhance estimation accuracy but suffer from high computational costs, energy consumption, and the need for frequent retraining. Optimization methods, such as particle swarm optimization and genetic algorithms, help refine hyperparameters but may encounter local minima traps and require significant computational resources. Additionally, SOE estimation is less explored compared to SOC, with existing approaches being sensitive to sensor inaccuracies and prone to error accumulation. These challenges highlight the need for efficient techniques that can

reduce dataset redundancy, improve computational efficiency, and ensure accurate SOC/SOE estimation while aligning with the principles of Green AI.

4.2.6 Green AI Perspective in Battery State Estimation

The rapid adoption of artificial intelligence in battery state estimation has significantly improved prediction accuracy and robustness; however, it has also introduced new challenges in terms of computational cost and energy consumption. Traditional deep learning architectures, such as LSTM, GRU, and hybrid CNN-RNN models, often require extensive datasets, prolonged training times, and frequent hyperparameter tuning. These factors not only increase the carbon footprint of training but also hinder real-time deployment in embedded systems with limited computational resources. Green AI emphasizes the development of energy-efficient and sustainable AI models that achieve high performance while minimizing computational demand. In the context of battery modeling, this perspective is particularly important since excessive energy consumption during model training contradicts the overarching goal of enabling cleaner, more sustainable energy solutions. Techniques such as model pruning, quantization, lightweight architectures, and redundant data filtering are key strategies to balance accuracy with computational efficiency.

For SOC and SOE estimation, integrating Green AI approaches ensures reduced training time, optimized memory utilization, and lower energy requirements without compromising accuracy. In addition, these methods support real-time implementation in BMS, where fast response and low power consumption are critical. Beyond efficiency, the Green AI perspective also enhances the scalability of battery modeling, making it feasible to adapt across different chemistries, drive cycles, and operating conditions. Thus, aligning battery state estimation with Green AI principles not only addresses technical challenges but also contributes to broader sustainability goals in electrified transportation and renewable energy integration.

4.3 DESIGN AND MODELING PROPOSED HYBRID FILTER TECHNIQUE FRAMEWORK

The accurate SOC/SOE estimation of the LIBs can extend mileage and lifecycle for consumers. These accurate estimation data can be used as supportive data for the development of BMS of EVs, and they can increase efficiency and reduce degradation over time of the LIBs. Hence, developing a robust SOC and SOE estimation framework approach is needed [51]. The SOC is defined as the ratio of the remaining available capacity to the nominal capacity of the battery. However, SOE is defined as the ratio of remaining battery energy under specific operating circumstances, such as variable temperature and load, over the total battery available energy. Battery SOE estimation was used to compute the available energy information of the battery. However, battery SOC refers to available capacity (Ah) rather than available energy (Wh). The SOC and SOE can be represented by equations 4.8 and 4.10, [52].

$$SOC_t = SOC_0 - \frac{\int_0^t i(\xi) d\xi}{C_n} \quad (4.8)$$

$$SOE_t = SOE_0 - \frac{\int_0^t p(\xi) d\xi}{E_n} \quad (4.9)$$

$$SOE_t = SOE_0 - \frac{\int_0^t i(\xi)u(\xi) d\xi}{E_n} \quad (4.10)$$

Where initial SOC is (SOC_0), SOC_t is SOC at time t, nominal capacity (C_n), SOE at time t is (SOE_t), SOE_0 initial SOE, total available energy is (E_n), current $i(\xi)$, power $p(\xi)$, and voltage $u(\xi)$ at time ξ , respectively. In this work, the authors examined the comprehensive analysis that precisely estimated the SOC and SOE of LIBs under four dynamic drive cycles. The proposed SOC and SOE estimation framework with FT is represented in Figure 4.5.

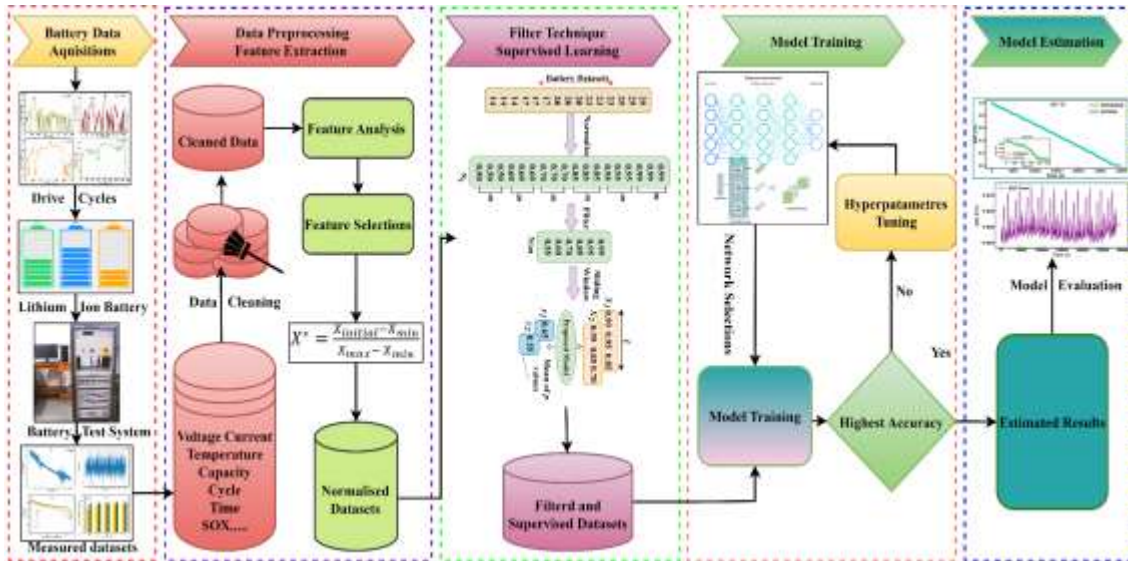


Figure 4.5 The proposed SOC and SOE estimation framework with filter technique

4.3.1 Mathematical Modelling of FT, Supervised Learning and Sliding Window Approach

Frequently, it is noticed that a massive dataset has several similar values. These values only enhance the sequence of the dataset and enlarge its size. When such data is processed by AI models, the model training time increases. Hence, the model exhibits a significant time delay in providing its result and requires a higher level of power consumption, thereby making it unsatisfactory for any system. To improve the efficiency of model training, we proposed FT that decreased the volume of the dataset without affecting the original patterns. However, when the FT was integrated with the AI models, it attained higher estimated accuracy and computational efficiency in comparison to other models that were excluded from the FT. The FT works as an average-based reduction process. The main aim of this filtering process is to preserve significant data patterns while reducing the volume and length of original datasets, as shown in Figure 4.6.

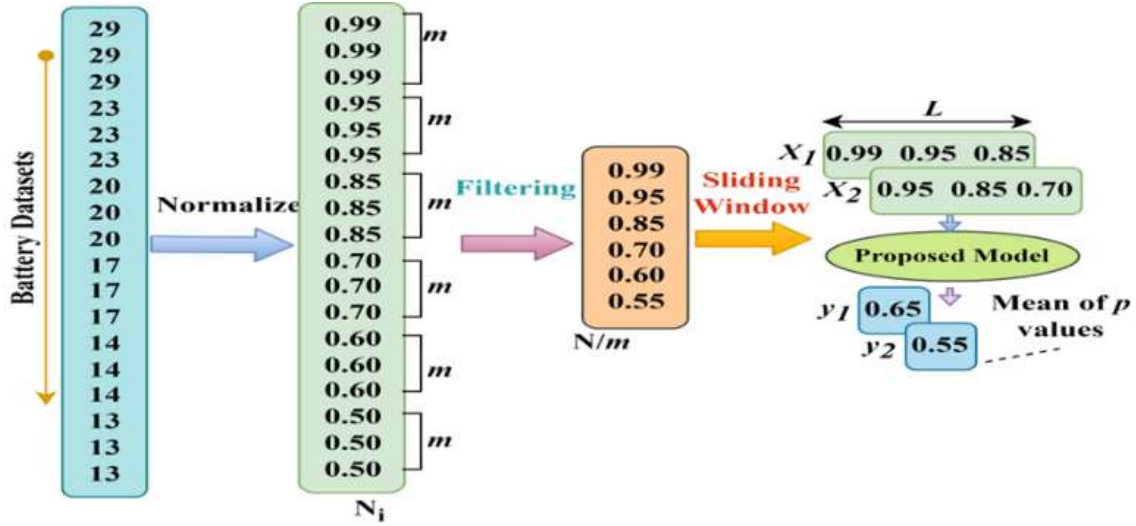


Figure 4.6 The proposed filter technique with the supervised learning model

Let's consider original battery dataset is D with N data points as expressed in equation 4.11:

$$D = \{d_1, d_2, d_3, \dots, d_N\} \quad (4.11)$$

The original datasets were normalized to obtain the sequence, as expressed in equation 4.12:

$$N_i = \left\{ \frac{d_i - \min(D)}{\max(D) - \min(D)} \mid i = 1, 2, \dots, N \right\} \quad (4.12)$$

This normalization scales the data to a range $[0, 1]$. The normalized dataset has duplicate values when used for AI model training because of its heavily grouped values. Let the normalized sequence N_i be defined, as expressed in equation 4.13:

$$N_i = \{x_1, x_2, x_3, \dots, x_n\} \quad (4.13)$$

Where each x_i represents a normalized value in the normalized dataset. x_i is the i th value in the sequence. The n is the total number of elements in the sequence N_i . An effective way to avoid duplication without affecting significant data is to average groups of consecutively similar values to reduce the original sequence. The filtering process involves grouping the sequence into smaller

batches of size named `mean_batch`, calculating the average of each batch, and creating a new filtered sequence (F). Let's consider `mean_batch = k`. Then, the F is given in equation 4.14:

$$F = \{f_1, f_2, \dots, f_{\frac{n}{k}}\} \quad (4.14)$$

The average (f_i) of the i th group of k consecutive values in N_i is used. The k denotes the number of duplicate numbers in each group used to compute an average. The length of the filtered sequence is $\frac{n}{k}$, assumed to be divisible by k . The average for each batch f_i is calculated as expressed in equation 4.15:

$$f_i = \frac{1}{k} \sum_{j=1}^k x_{(i-1)k+j}, \quad i = 1, 2, \dots, \frac{n}{k} \quad (4.15)$$

During supervised learning, the filtered sequence is applied to generate input sequences with a fixed number of steps in order to preserve the historical structure. In the sliding window approach, a subsequence of length m ($m = n_steps$) is chosen as the input sequence, and the output is predicted as the average of the next p steps ($p = pred_steps$). The input sequence (X_i) consists of m consecutive values from the filtered sequence F , as expressed in equation 4.16.

$$X_i = \{f_i, f_{i+1}, \dots, f_{i+m-1}\} \quad (4.16)$$

Where m is the number of steps in each input sequence. The initial value of i is 1 and increases by 1 in each iteration until it reaches $\frac{n}{k} - m - p + 1$. This defining valid positions for sequence operations within the filtered sequence. Where p is the number of prediction steps. The output value for every input sequence is obtained by taking the average of the following p steps, which correspond to the pattern and prediction purpose. The output value y_i is the average of the subsequent p consecutive values derived from the filtered sequence F subsequent to the input sequence X_i , as expressed in equation 4.17.

$$y_i = \frac{1}{p} \sum_{j=1}^p f_{i+m-1+j} \quad (4.17)$$

A large amount of data reduces the AI model's performance. The actual dataset points in the different drive cycles, HWFET, LA92, UDDS, and US06, are 40161, 76374, 124941, and 27868, respectively, as shown in Figure 4.7 and 4.8.

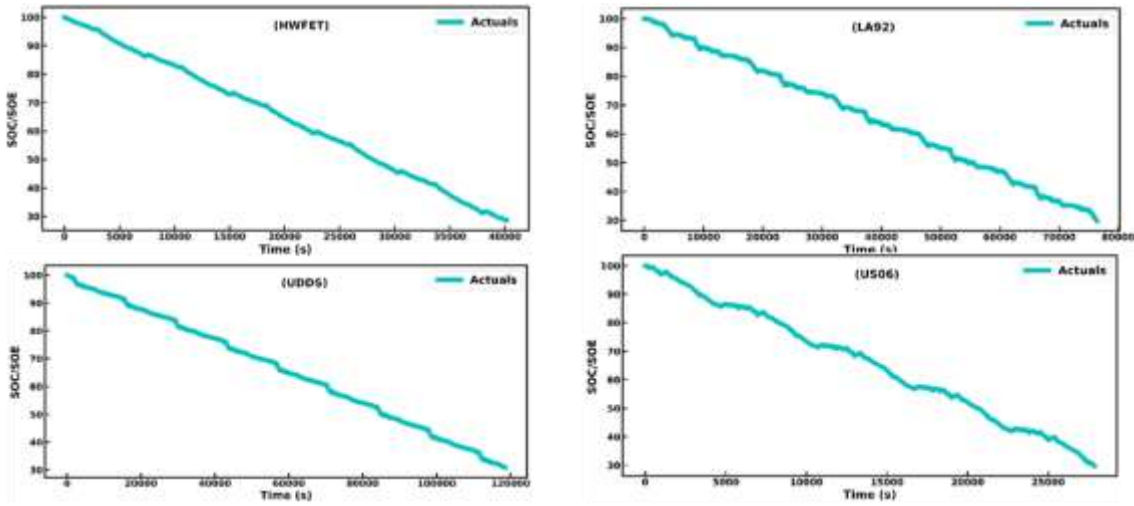


Figure 4.7 Actual datasets of the four different drive cycles without the filter techniques

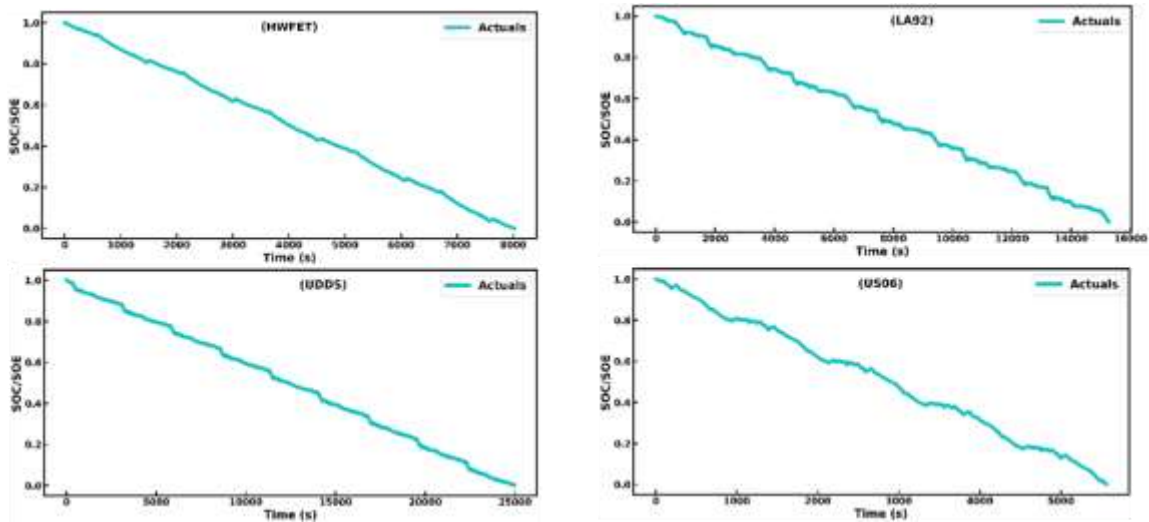


Figure 4.8 Actual datasets of the different four cycles with the filter techniques

Table 4.1 illustrates the notable reductions in both dataset size and memory usage that occurred when the filtering technique was implemented on the original datasets on various drive cycles. For instance, the memory used to decrease by 80%, from 315 KB to 63 KB, and the size of the HWFET dataset decreased by 80%, from 40,161 values to 8,022. On the other hand, the LA92 dataset experienced an 80.07% reduction in memory utilization from 597 KB to 119 KB and an 80.03% decrease in size from 76,374 to 15,264 values. The size of the UDDS dataset decreased by 80.03%, from 124,941 to 24,978 values, and memory utilization decreased by 79.84%, from 977 KB to 197 KB. Lastly, the US06 datasets memory usage dropped by 79.45%, from 219 KB to 45 KB, and its overall size shrank by 80.03%, from 27,868 to 5,563 items.

Table 4. 1 Data description with and without filter techniques

Drive Cycles	Actual Dataset Length	Filtered Dataset Length	Percentage Reduction (%)	Memory Used (Actual dataset)	Memory Used (Filtered dataset)	Percentage Reduction (%)
HWFET	40161	8022	80.02	315 KB	63 KB	80.00
LA92	76374	15264	80.01	597 KB	119 KB	80.06
UDDS	124941	24978	80.00	977 KB	197 KB	79.83
US06	27868	5563	80.03	219 KB	45 KB	79.45

The AI models benefit significantly from these reductions in training computational energy, and power consumption. Decreasing dataset size speeds up model processing, reducing training time and improving performance. Reduced memory utilization is one of the most significant benefits of AI models because this makes it possible to run on low-resource hardware, making them more affordable and significant to a larger range of devices and applications. These advantages are crucial in driverless cars, medical diagnostics, and IoT devices, where massive processing of data with high efficiency is required.

4.4 EXPERIMENTAL SETUP AND DATASET DESCRIPTION

The experimental work has been performed in our laboratory Centre of Excellence for Electric Vehicles and Related Technologies, Delhi Technological University, Delhi. The charge and

discharge of the battery cells are controlled by Chroma regenerative battery pack test system model 17020 and its software, as shown in Figure 4.9. It is capable of charging and discharging the test battery in a range of preset current or voltage settings. The host computer containing Chroma 17020 software configures several settings, including sampling timing, cut-off frequencies, and battery charging and discharging specifications. The battery negative and positive terminals are connected to the acquisition and output terminals of the Chroma 17020 test system. After that, the current profile of the drive cycle, UDDS, LA92, US06, and HWFET is set on the host computer to perform the test and analyse the results. To record the battery surface temperatures using the built-in chroma have been sensors. To build the program for the model training and for simulation, Python were used. To train the proposed models, the data from the tested battery was applied. The best hyperparameters of the network for the training were selected precisely [117]. These models used integration with and without filter techniques with supervised learning for SOC and SOE estimation of LIBs under different dynamic drive cycles. To precisely evaluate proposed models, the authors used the same hyperparameters and evaluation matrices to assess performance in various driving cycles.

4.4.1 18650 Battery Specifications and Testing Conditions

The Chroma 17020 regenerative battery test system used as an experimental platform in this investigation is depicted in Figure 4.9. In addition, all the battery tests are performed with the above battery tester. The host computer is used to record battery information, such as voltage, current, temperature, and so on. In these experiments, 18650 lithium-ion batteries with 2.6 Ah rated capacity are studied. The test battery parameters are tabulated in Table 4.2.



Figure 4.9 Schematic diagram of the experimental test bench and data logging system

Table 4. 2 The battery technical information

Battery	Rechargeable Lithium-ion
Format	Cylindrical 18650
Cathode	NMC
Rated Capacity, Voltage	5.0 Ah, 3.7 V
Normalized Resistance	14 mΩ
Specific Power	7.3 W/kg
Specific Energy	134k Wh/kg
Energy Density	329 Wh/l

4.4.2 Dynamic Drive Cycles

Based on the current profile of driving cycles, four different drive cycles are used. The Urban Dynamometer Driving Schedule (UDDS), Los Angeles 92 (LA92), Supplemental Federal Test Procedure Driving Schedule (US06), and Highway Fuel Economy Driving Schedule (HWFET) are published by the United States Environmental Protection Agency (EPA), as shown in Figure 4.10. The UDDS is known for the light vehicle on city driving conditions, and the LA92 simulates energy-efficient and low-emission driving situations. The US06 simulates complex driving situations on the highway, and HWFET signifies that 77 km/h is the average speed at which driving conditions are simulated. These driving cycle profiles cover the battery load behaviours of electric

vehicles in various environments. It should be clarified that all charge and discharge measurements are performed at 25 degrees Celsius at ambient temperatures.

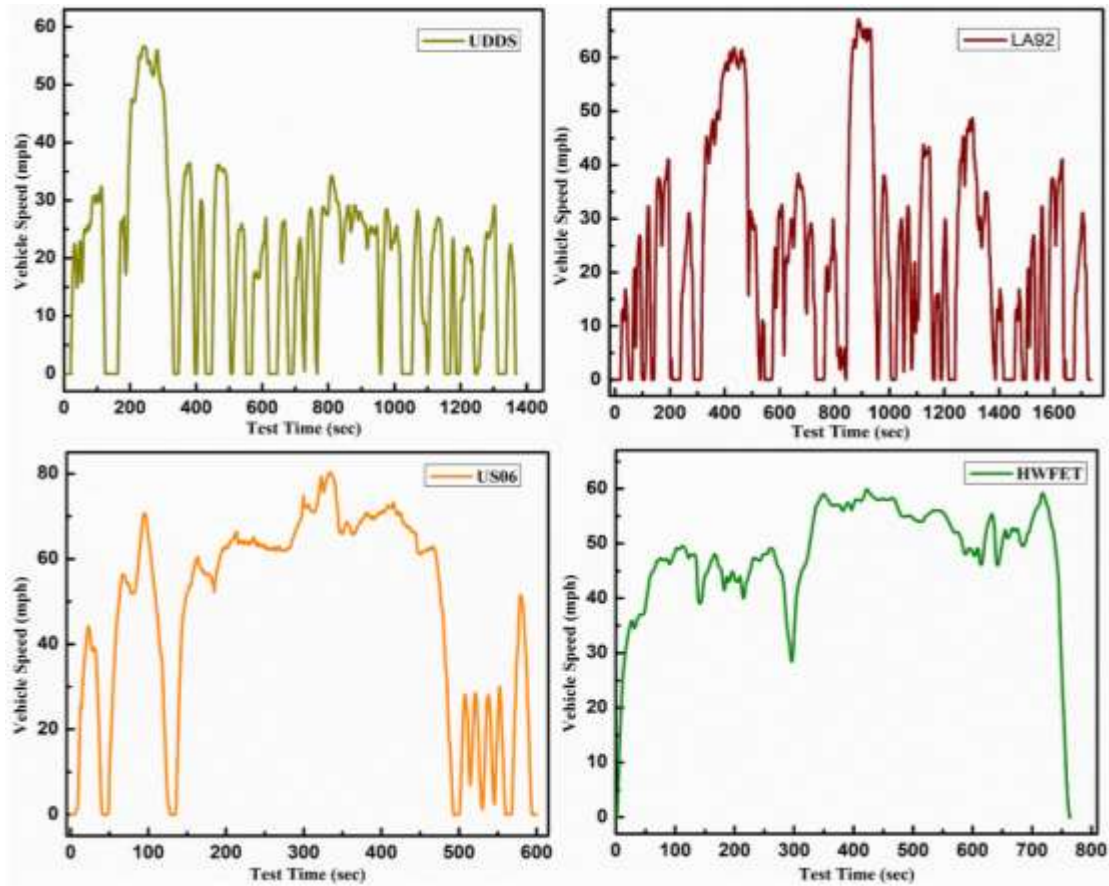


Figure 4.10 The four drive cycles for tested the LIBs

4.4.3 Battery Data Diversity Analysis

To employ AI models for SOC and SOE estimation, it is required to analyse the correlation of different features, i.e. voltage, current, temperature, capacity, and SOC and SOE. Its influence on SOC and SOE estimation within the collected dataset. The significance of correlation analysis lies in its ability to identify redundant and irrelevant data to improve the performance of AI models. Therefore, to determine the most correlated features and how they relate to SOC and SOE estimation. The correlation matrix displays the resultant matrix as shown in Figure 4.11.

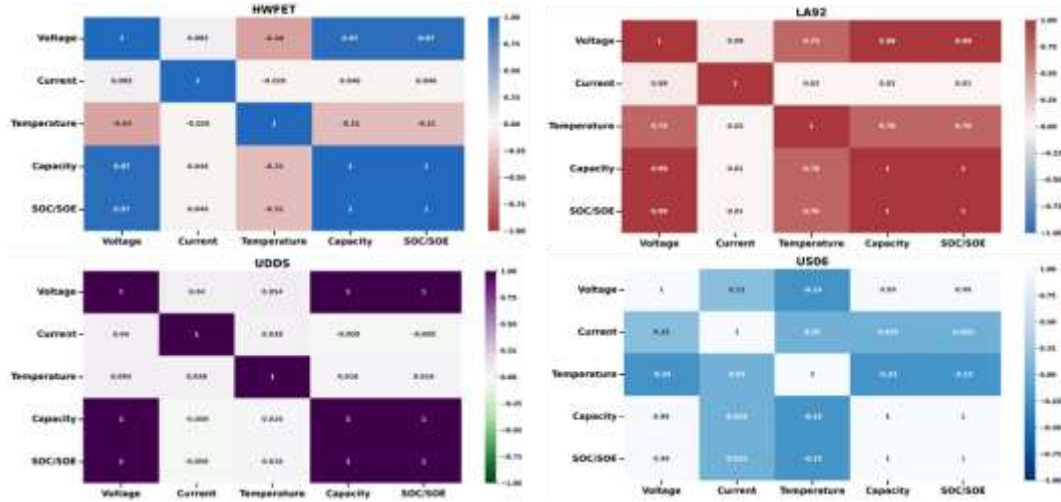


Figure 4.11 The correlation matrix of four different EV drive cycles

It exhibited temperature, voltage, current, SOC and SOE correlation of four driving cycles. Upon examination of the correlation matrix, it was found that a few more correlated features in the dataset might potentially cause multicollinearity and instabilities within the proposed model.

4.4.4 Model Evaluation Metrics

Three metrics are used to evaluate the estimation accuracy of the proposed CNN-SBLSTM network, such as maximum absolute error (MaxError), mean absolute error (MAE), and root mean square error (RMSE) as expressed in equations 4.18-4.21. The accuracy of the estimation is validated by MAE, while the robustness of the estimation is validated by RMSE, and the reliability of the estimation is demonstrated by MaxError.

$$MAE = \frac{1}{m} \sum_{t=1}^m |(\hat{SOC}(t) - SOC(t))| \quad (4.18)$$

$$MSE = \frac{1}{m} \sum_{t=1}^m (\hat{SOC}(t) - SOC(t))^2 \quad (4.19)$$

$$RMSE = \sqrt{\frac{1}{m} \sum_{k=1}^m (SOC_k - SOC'_k)^2} \quad (4.20)$$

$$MaxE = \max_{t=1, 2, 3, \dots, m} |(\hat{SOC}(t) - SOC(t))| \quad (4.21)$$

4.5 RESULTS AND DISCUSSION

This section evaluated trained AI approaches integration with and without filter technique with supervised learning for ambient temperature SOC/SOE estimation.

4.5.1 Model Performance without FT in different Drive Cycles

This section evaluates the performance of five AI approaches for SOC and SOE estimation across four standard dynamic drive cycles without applying the proposed filtering technique or supervised learning. Figure 4.12(a-d). present the estimation results, while Figure 4.12 (e–h) illustrates the associated estimation errors. The detailed statistical outcomes are summarised in Table 4.3.

4.1.1.1 HWFET Drive Cycle

The CNN-BiLSTM model consistently outperformed other approaches, achieving improvements of 52.09% in RMSE, 70.06% in MSE, 7.06% in MAE, and 66.75% in maximum error. The highest coefficient of determination, $R^2 = 95.73\%$, confirmed strong alignment between actual and estimated SOC/SOE values, indicating reliable prediction accuracy.

4.1.1.2 LA92 Drive Cycle

In this cycle, CNN-BiLSTM again demonstrated superior accuracy with average improvements of 46.51% in RMSE, 65.16% in MSE, 46.51% in MAE, and 57.46% in maximum error. R^2 values ranged from 87.99% to 95.73%, with CNN-BiLSTM achieving the best performance, highlighting its robustness under complex drive conditions.

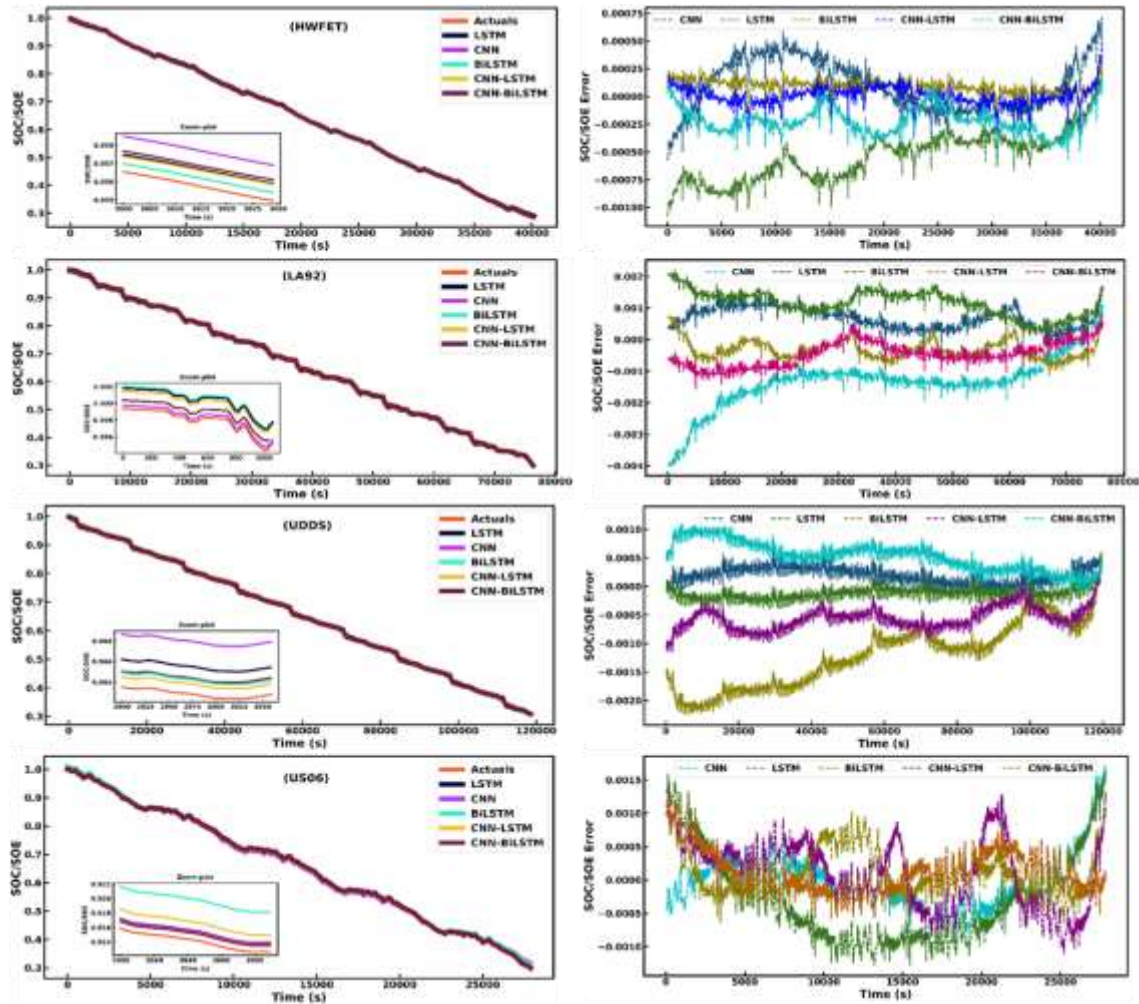


Figure 4.12 The SOC/SOE estimation result (a-d) and estimation errors (e-h) without FT (a) HWFET; (b) LA92; (c) UDDS; (d) US06; drive cycles

4.1.1.3 UDDS Drive Cycle

For UDDS, CNN-BiLSTM achieved the lowest error values, with average improvements of 45.86% in RMSE, 64.52% in MSE, 45.86% in MAE, and 75.83% in maximum error. R^2 values varied between 89.03% and 96.93%, again underscoring the strong correlation between predicted and actual values.

Table 4. 3 The statistical performances of proposed models without FT

Drive Cycles	Approaches	MAE	MSE	RMSE	R ²	Maximum Error
HWFET	CNN	1.5635	3.8373	1.9589	0.8993	0.0049
	LSTM	2.0542	6.6294	2.5747	0.8799	0.0070
	BiLSTM	1.3561	2.8882	1.6994	0.9192	0.0026
	CNN-LSTM	1.5575	3.8054	1.9507	0.9397	0.0015
	CNN-Bi-LSTM	0.5572	0.4869	0.6975	0.9573	0.0003
LA92	CNN	1.4665	3.3732	1.8367	0.9035	0.0013
	LSTM	2.1364	7.1642	2.6766	0.8935	0.0028
	BiLSTM	1.3572	2.8903	1.7001	0.9157	0.0011
	CNN-LSTM	1.1962	2.2455	1.4985	0.9369	0.0081
	CNN-Bi-LSTM	0.1662	0.0431	0.2076	0.9798	0.0001
UDDS	CNN	1.1475	2.0652	1.4370	0.8904	0.0026
	LSTM	2.3378	8.5751	2.9283	0.9079	0.0053
	BiLSTM	1.1765	2.1708	1.4733	0.9339	0.0093
	CNN-LSTM	1.1574	2.1008	1.4494	0.9295	0.0040
	CNN-Bi-LSTM	0.1163	0.0210	0.1449	0.9693	0.0002
US06	CNN	1.3578	2.8906	1.7001	0.9199	0.0017
	LSTM	2.3172	8.4294	2.9033	0.9599	0.0011
	BiLSTM	2.0071	6.3243	2.5148	0.9396	0.0029
	CNN-LSTM	1.6567	4.3114	2.0764	0.9498	0.0016
	CNN-Bi-LSTM	0.2127	0.07082	0.2661	0.9887	0.0001

*The bold are represented best results.

4.1.1.4 US06 Drive Cycle

In the most aggressive cycle, US06, CNN-BiLSTM maintained its dominance, delivering improvements of 59% in RMSE, 74.32% in MSE, 59.12% in MAE, and 74.17% in maximum error. The highest R² value of 98.87% was achieved, confirming excellent predictive performance. Overall, the CNN-BiLSTM approach demonstrated consistent superiority across all cycles, offering accurate SOC/SOE estimation and strong generalization capability. However, the models exhibited computational complexity due to the absence of dataset filtering, highlighting the need for efficiency improvements.

4.5.2 Model Performance with FT in different Drive Cycles

This section evaluates the integration of the proposed FT with supervised learning for SOC and SOE estimation across four dynamic drive cycles Figure 4.13. (a–d) illustrate the estimation results, while Figure 4.13.(e–h) show the associated estimation errors. The detailed statistical results are provided in Table 4.4.

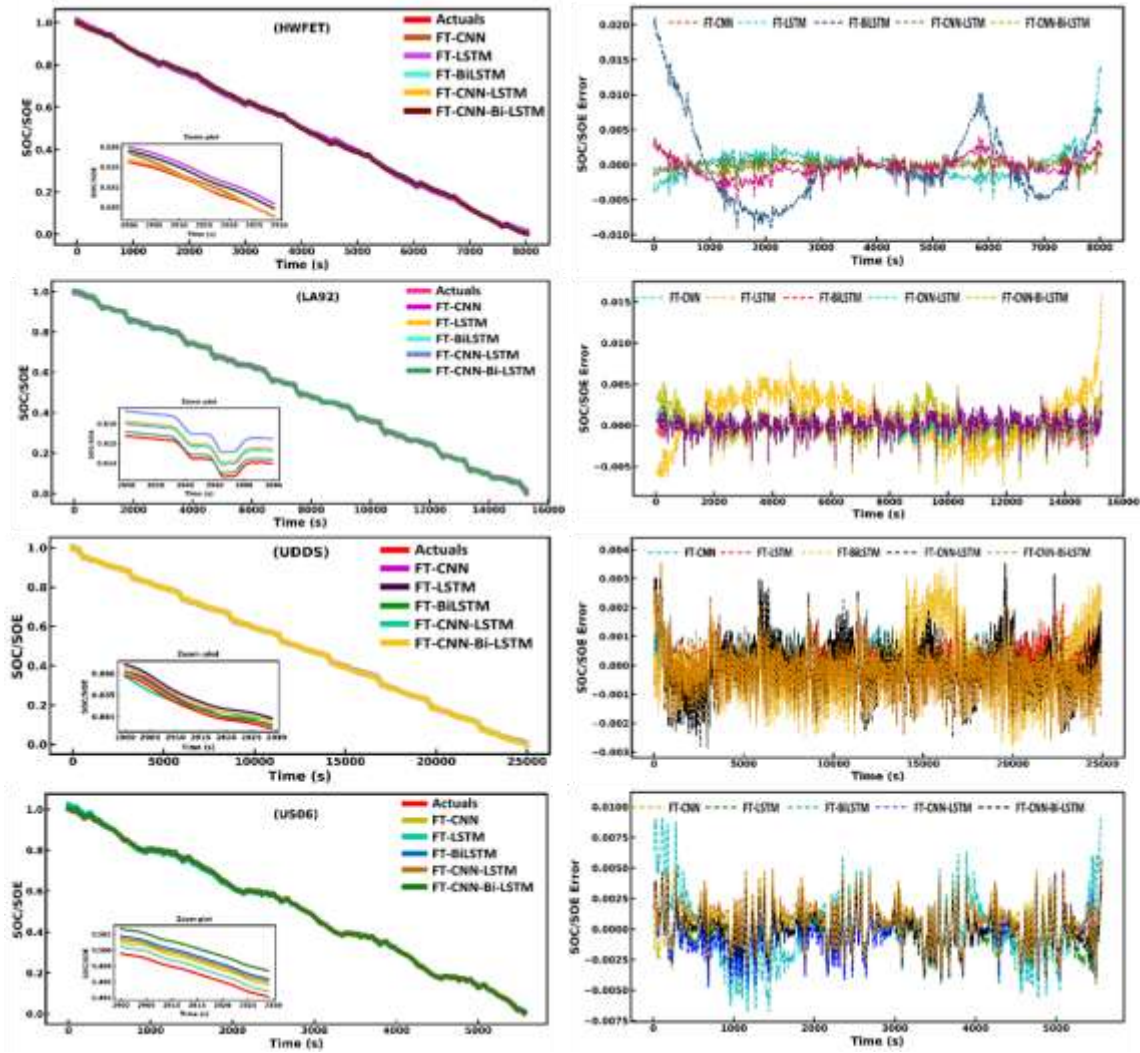


Figure 4.13 SOC/SOE estimation result (a-d) and estimation errors with FT (e-h), (a) HWFET (b) LA92; (c) UDDS; (d) US06; drive cycles

Five approaches, FT-CNN, FT-LSTM, FT-BiLSTM, FT-CNN-LSTM, and FT-CNN-BiLSTM, were comparatively analyzed using standard performance metrics such as MAE, MSE, RMSE, maximum error, and R^2 .

4.5.2.1 HWFET Drive Cycle

The FT-CNN-BiLSTM achieved the lowest RMSE and MSE values with average improvements of 75% in MAE, 79.54% in MSE, and 75.06% in RMSE. Its R^2 value 99.77%, confirming excellent predictive ability and reliability in dynamic conditions.

Table 4. 4 The statistical performances of proposed models with FT

Drive Cycles	Approaches	MAE	MSE	RMSE	R^2	Maximum Error
HWFET	FT-CNN	0.0069	5.8754e-05	0.0076	0.9883	0.0151
	FT-LSTM	0.0015	4.5876e-06	0.0021	0.9875	0.0138
	FT-BiLSTM	0.0011	2.1901e-06	0.0014	0.9841	0.0055
	FT-CNN-LSTM	0.004	4.5505e-07	0.0006	0.9870	0.0036
	FT-CNN-Bi-LSTM	0.0005	6.0550e-07	0.0007	0.9977	0.0017
LA92	FT-CNN	0.0013	3.4736e-06	0.0018	0.9859	0.0085
	FT-LSTM	0.0026	1.0066e-05	0.0031	0.9863	0.0163
	FT-BiLSTM	0.0011	2.2527e-06	0.0015	0.9951	0.0056
	FT-CNN-LSTM	0.0007	9.3551e-07	0.0009	0.9979	0.0051
	FT-CNN-Bi-LSTM	0.0007	9.1360e-07	0.0009	0.9983	0.005
UDDS	FT-CNN	0.0005	6.7643e-07	0.0008	0.9830	0.0053
	FT-LSTM	0.0008	1.0634e-06	0.0010	0.9738	0.0039
	FT-BiLSTM	0.0004	4.5786e-07	0.0006	0.9814	0.0036
	FT-CNN-LSTM	0.0004	3.3170e-07	0.0005	0.9799	0.0032
	FT-CNN-Bi-LSTM	0.0005	5.1110e-07	0.0007	0.9875	0.002
US06	FT-CNN	0.0050	5.1209e-05	0.0071	0.9731	0.0259
	FT-LSTM	0.0017	5.1377e-06	0.0022	0.9691	0.0082
	FT-BiLSTM	0.0020	7.6331e-06	0.0027	0.9701	0.0103
	FT-CNN-LSTM	0.0011	2.1394e-06	0.0014	0.9858	0.0049
	FT-CNN-Bi-LSTM	0.0012	2.4616e-06	0.0015	0.9897	0.0044

*The bold are represented best results.

4.5.2.2 LA92 Drive Cycle

The FT-CNN-BiLSTM consistently outperformed other models, achieving improvements of 70.47% in MAE, 78.73% in MSE, 70.50% in RMSE, and 40.88% in maximum error. A near-unity R^2 value 99.83% indicated superior accuracy and robustness for SOC/SOE estimation.

4.5.2.3 UDDS Drive Cycle

In this cycle, FT-CNN-BiLSTM achieved 77.66% improvement in MAE, 79.92% in MSE, 77.66% in RMSE, and 38.58% in maximum error, with an R^2 of 98.75%. These results demonstrate its strong capability to capture SOC/SOE deviations under complex drive conditions.

4.5.2.4 US06 Drive Cycle

The most aggressive US06 cycle further validated the superiority of FT-CNN-BiLSTM, which achieved improvements of 74% in MAE, 79.35% in MSE, 73.59% in RMSE, and 39.36% in maximum error, with an R^2 of 98.97%. Across all datasets, FT-CNN-BiLSTM consistently reduced RMSE values by up to 98.11% (HWFET), 94.23% (LA92), 98.08% (UDDS), and 97.20% (US06) compared to baseline approaches. The MSE and MAE also showed remarkable reductions, ranging from 83.33% to 99.96%. This superior performance results from CNN's capability to extract deep features and BiLSTM ability to capture temporal dependencies in both directions.

Overall, the integration of the filtering technique significantly improved model accuracy, reduced computational complexity, and minimized dataset redundancy. The FT-CNN-BiLSTM model demonstrated consistent generalization across all drive cycles, highlighting its potential for real-world BMS applications under a Green AI framework.

4.5.2.5 Computational Efficiency and Energy Consumption Analysis

A comprehensive comparison was carried out between AI models trained with and without the FT across four dynamic drive cycles. The evaluation considered estimation accuracy, MAE, MSE, RMSE, maximum error, R^2 , alongside computational efficiency, time, active power, and energy consumption, as shown in Table 4.5. Results show that incorporating FT significantly enhances both precision and efficiency. Among all tested models, the FT-CNN-BiLSTM consistently outperformed its counterparts. Compared to the baseline CNN-BiLSTM, it achieved improvements of up to 99.98% in RMSE, 99.97% in MSE, and 99.96% in MAE, while also reducing computational time by 59–66% and energy consumption by 61–68% across all drive cycles. These quantitative improvements demonstrate that FT not only preserves data integrity while reducing dataset volume by up to 80% but also ensures superior estimation accuracy and

reduces resource usage, aligning with Green AI objectives. The FT-CNN-BiLSTM emerges as the most reliable and sustainable solution for real-time SOC/SOE estimation in EV. These improvements demonstrate that integrating FT results in faster model convergence, reduced memory requirements, and significantly lower consumption, all of which align with the sustainability goals of Green AI.

4.5.3 Filtering Technique and Its Role in BMS

The comparative evaluation confirmed that FT significantly enhances SOC/SOE estimation accuracy and computational efficiency. Across all drive cycles, the FT-CNN-BiLSTM model reduced RMSE by up to 99.98%, MSE by 99.97%, and MAE by 99.96% compared to the traditional CNN-BiLSTM. Computational time decreased by 59–66%, while energy consumption dropped by 61–68%, demonstrating both faster convergence and lower resource demand. FT also reduced dataset volume by up to 80% without compromising data integrity, thereby enabling more efficient learning. These improvements directly benefit BMS by enabling faster, more reliable, and energy-efficient SOC/SOE estimation, which is critical for real-time electric vehicle operation. Furthermore, integrating FT aligns with the principles of Green AI, reducing unnecessary computational overhead and carbon footprint while extending battery life. Thus, FT not only improves technical performance but also supports sustainable and intelligent energy management. This establishes FT as a promising pathway for next-generation BMS design under Green AI principles.

Table 4. 5 Energy consumption and computational time comparisons of all models

Drive Cycles	Approaches	MAE	MSE	RMSE	R ²	Maximum Error
HWFET	CNN	1.5635	3.8373	1.9589	0.8993	0.0049
	LSTM	2.0542	6.6294	2.5747	0.8799	0.0070
	BiLSTM	1.3561	2.8882	1.6994	0.9192	0.0026
	CNN-LSTM	1.5575	3.8054	1.9507	0.9397	0.0015
	CNN-Bi-LSTM	0.5572	0.4869	0.6975	0.9573	0.0003
LA92	CNN	1.4665	3.3732	1.8367	0.9035	0.0013
	LSTM	2.1364	7.1642	2.6766	0.8935	0.0028
	BiLSTM	1.3572	2.8903	1.7001	0.9157	0.0011
	CNN-LSTM	1.1962	2.2455	1.4985	0.9369	0.0081
	CNN-Bi-LSTM	0.1662	0.0431	0.2076	0.9798	0.0001
UDDS	CNN	1.1475	2.0652	1.4370	0.8904	0.0026
	LSTM	2.3378	8.5751	2.9283	0.9079	0.0053
	BiLSTM	1.1765	2.1708	1.4733	0.9339	0.0093
	CNN-LSTM	1.1574	2.1008	1.4494	0.9295	0.0040
	CNN-Bi-LSTM	0.1163	0.0210	0.1449	0.9693	0.0002
US06	CNN	1.3578	2.8906	1.7001	0.9199	0.0017
	LSTM	2.3172	8.4294	2.9033	0.9599	0.0011
	BiLSTM	2.0071	6.3243	2.5148	0.9396	0.0029
	CNN-LSTM	1.6567	4.3114	2.0764	0.9498	0.0016
	CNN-Bi-LSTM	0.2127	0.07082	0.2661	0.9887	0.0001

*The bold are represented best results.

4.6 CONCLUSION

This work proposed a novel FT with supervised learning to enhance AI-based SOC/SOE estimation in lithium-ion batteries. By reducing dataset volume by up to 80% while maintaining data integrity, FT improves model accuracy, reduces computational time, and lowers energy consumption. The proposed FT-CNN-BiLSTM model, tested on four dynamic drive cycles, consistently outperformed traditional AI models. It achieved improvements of 99.98% in RMSE, 99.97% in MSE, and 99.96% in MAE, alongside reductions of 59–66% in computation time and 61–68% in energy consumption compared to CNN-BiLSTM. These results demonstrate that FT significantly strengthens estimation robustness, accelerates model convergence, and aligns with the principles of Green AI by minimising carbon-intensive computations. The approach supports faster, more reliable, and energy-efficient Battery Management Systems (BMS), extending battery life and ensuring safer operation in electric vehicles. Future research will extend this framework to different battery chemistries and temperature conditions, broadening its applicability for real-world deployment

CHAPTER 5

DEVELOPMENT OF AI-BASED ALGORITHM FOR BATTERY HEALTH MONITORING IN BMS

5.1 INTRODUCTION

Battery health monitoring in LIBs is essential to ensure safe operation, enhance performance, and extend the lifetime of the BMS. Among various health indicators, the SOH is a critical parameter that indicates the battery degradation, capacity loss, and the ageing behaviour. The accurate SOH estimation, necessary to prevent failures, enables predictive maintenance, hazardous failures, and optimizes energy management strategies in EVs and grid ESSs. This chapter focuses on the development of an AI-based algorithm for efficient SOH estimation in BMS. This work presents the use of the data FT combined with the DL model to improve prediction accuracy by reducing the computational complexity and energy consumption. The proposed approach aims to enhance real-time health monitoring and support the reliable and sustainable operation of the next generation. Table 5.1, recent literature on SOH estimation of lithium-ion batteries using AI techniques, highlighting key findings, advantages, limitations, and the extent of Green AI considerations [118], [119], [120], [121], [122], [123].

Table 5. 1 Literature related to SOH estimations

Year	Key Findings	Advantages	Disadvantages	Limitations	Green AI Focus
2026	A deep-learning-based battery health prediction model was proposed for SOH and remaining useful life (RUL) estimation in EV batteries to improve lifecycle monitoring and predictive maintenance.		Deep learning models increase computational complexity and training time.	Deployment in embedded BMS systems may be challenging due to power and hardware constraints.	Moderate alignment with Green AI since the work discusses efficiency challenges for real-time BMS deployment.
2025	Neural-ODE-based deep learning model combining CNN, LSTM, and	hybrid model	Hybrid architecture increases model training complexity.	Computational cost may restrict	Minimal Green AI focus; emphasis mainly on

	attention mechanisms for SOH estimation using charging curves.		embedded BMS implementation.	predictive accuracy.
2025	A multi-expert fusion network (MEFNet) combining mechanism models, LSTM, and Transformer was proposed for accurate SOH estimation.	High model complexity due to hybrid architecture.	Requires significant training data and computational resources.	Limited Green AI considerations; focus mainly on accuracy improvement.
2024	Increased SOH estimate accuracy with 10%, 30%, and 50% data incompleteness. Robust against incomplete data. LiNCM and LiFePO4 battery compatibility.	Higher computational time compared to simple algorithms like SVR and GRU. Moderate training complexity.	Limited Green AI concepts explored. It did not carefully reduce computing costs or energy usage in algorithm design.	The methodology did not explicitly address Green AI concepts.
2023	Used source data to eliminate deterioration tests. Overall, dataset estimate accuracy is high. Using experimental data effectively. Strong data imbalance resistance.	The computational cost for training multiple DNNs. Dependence on high-quality source data.	Limited exploration of computational efficiency. No clear measures for minimizing energy consumption during model training.	It does not clearly target energy efficiency in model design but indirectly supports resource saving by eliminating degradation experiments.
2022	Achieved SOH estimation error below 1.5%, 70% better than conventional methods, with reduced reliance on cell-level models and improved robustness.	Limited consideration of energy-efficient hardware setups. Performance can degrade under large-scale dynamic loads.	Assumes ideal voltage-based balancing, which may not hold in real-world applications. Energy loss during balancing is not accounted for comprehensively.	The study did not explicitly implement or evaluate Green AI principles. Optimizations for computational energy efficiency or hardware usage were not prioritized.
2021	Better estimate accuracy and reliability than SVR, ARIMA, and particle filters. Deterministic MLR models lowered RUL prediction MAPE by 60% above benchmarks. Less computation.	MLR models struggle with complex nonlinear relationships in predictors. Strong dependence on high-quality ADT data. Heavily reliant on ADT data quality and availability.	Performance degrades for long prediction horizons. Insufficient exploration of alternative energy-efficient methodologies or advanced ML models.	No explicit focus on reducing computational energy usage or adopting Green AI principles. Energy-efficient modelling approaches are not discussed.

5.2 NEED of AI-BASED ALGORITHM FOR BATTERY HEALTH MONITORING

The SOH is a critical parameter that indicates the battery degradation, capacity loss, and the ageing behaviour. The accurate SOH estimation, necessary to prevent failures, enables predictive maintenance, hazardous failures, and optimizes energy management strategies in EVs and grid ESSs. Conventional SOH estimation methods are lookup tables, coulomb counting, and model-based methods. Through direct measurement of battery parameters like capacity, internal resistance, and impedance, experimental methods estimate SOH.

5.2.1 Challenges in Energy-Efficient SOH Estimation

Accurate SOH estimation often involves processing large volumes of battery data, which increases computational cost, memory utilization, and energy consumption. Traditional AI and DL models, such as CNN, LSTM, and Bi-LSTM, require long training periods, mainly when hyperparameter tuning is performed on high-dimensional datasets. This not only increases energy usage but also limits real-time applicability in BMS. Key challenges include high computational demand, large dataset dependency, hyperparameter optimization, and real-time constraints. These challenges highlight the need for data-efficient frameworks and optimized AI models that reduce energy consumption while maintaining high predictive accuracy, forming the basis for the proposed filtering technique and lightweight AI approach in this study.

5.3 PROPOSED RESEARCH METHODOLOGY

This research presents an energy-efficient SOH estimation framework that integrates DL and filter-based methods, as shown in Figure 5.1. The entire process of the proposed work can be described as follows: Step 1: Collect battery-tested data, including current, voltage, capacity, and temperature measurements. Remove any outliers, smooth the data, and align all measurement data.

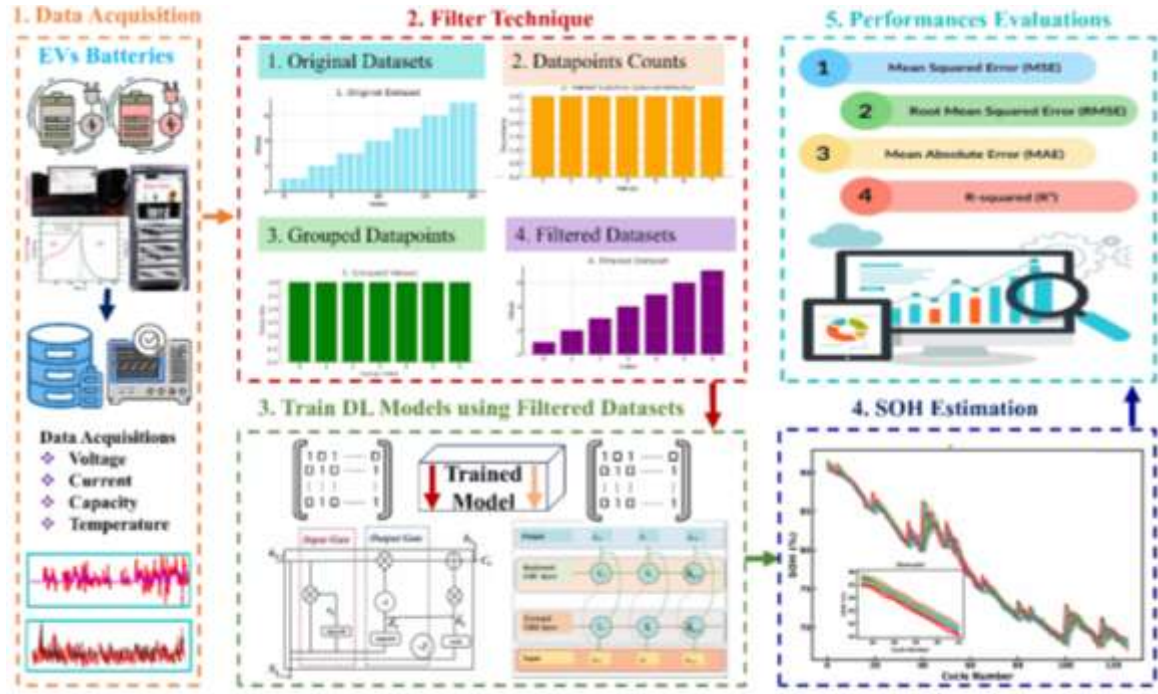


Figure 5.1 The proposed SOH estimation framework with the filter technique

Normalise the data by using a min-max scalar. Step 3: The FT method is applied to eliminate redundant and duplicate data points, reducing dataset size, computational load, and energy consumption while maintaining original degradation patterns. Step-4: Train the DL model, i.e., CNN, GRU, LSTM. Hyperparameter tuning is performed to optimise the model's performance. Step-5: Estimation of SOH output. The statistical performance of the models is calculated by calculating MAE, MSE, and RMSE, computational time, energy efficiency, and estimation errors.

5.3.1 Mathematical modelling of Filter Technique Approach

Let the original dataset D :

$$D = \{d_1, d_2, \dots, d_n\} \quad (5.1)$$

Where d_i represents the i^{th} data point in the dataset. n is the total number of data points in the original dataset. For example, consider similar duplicate values in the dataset D .

$$D = [1,1,1,2,2,2,3,3,3,4,4,4,5,5,5,6,6,6,7,7,7] \quad (5.2)$$

The identification of similar values and the count of their occurrence. For each unique value x_k in the dataset, count how many times it appears (its frequency) in the dataset D . The count function can be mathematically represented as:

$$f(x_k) = \sum_{i=1}^n \mathbf{1}_{(d_i=x_k)} \quad (5.3)$$

Where, $f(x_k)$ is the frequency of the value x_k in the dataset. $\mathbf{1}_{(d_i=x_k)}$ is the indicator function, which is 1 if $d_i = x_k$ and 0 otherwise. Group similar values based on a similarity threshold δ , which determines how close two values must be to be considered the same. For each unique value x_k in D , define the group G_k as:

$$G_k = \{d_i \mid |d_i - x_k| \leq \delta\} \text{ for each distinct } x_k \in D \quad (5.4)$$

Where, G_k is the group of similar values corresponding to the value x_k . δ the similarity threshold defines how two similar values must be grouped. A sensitivity analysis was conducted for δ values ranging from 0.01 to 0.10 to ensure model performance. At $\delta = 0.05$, ~85% data reduction was achieved with negligible impact on SOH estimation accuracy. This threshold prevents key transition points from being over-grouped and losing critical patterns. After grouping similar values, apply to the FT by selecting one representative value from each group G_k . The representative value can be chosen based on the mode (the most frequent value in the group), but could also be the mean. Let the representative value for each group be R_k .

$$R_k = \text{Mode}(G_k) \quad (5.5)$$

Where, R_k is the representative value of the group G_k . $\text{Mode}(G_k)$ returns the most frequent value in the group G_k . For example, datasets where the values in D are identical within each group, such

as $R_1 - 1, R_2 - 2, R_3 - 3, R_4 - 4, R_5 - 5, R_6 - 6, R_7 - 7$. After applying the filter technique, the filtered dataset D_f contains one representative value for each group of similar values.

$$D_f = \{R_1, R_2, \dots, R_m\} \quad (5.6)$$

Where, R_1, R_2, \dots, R_m are the representative values from each group. m is the number of groups formed after applying for the FT. For the example dataset, the filtered dataset will be.

$$D_f = [1,2,3,4,5,6,7] \quad (5.7)$$

Finally, calculate the reduction in the dataset size, which is the percentage decrease in the number of data points from the original dataset D to the filtered dataset D_f . The proposed approach differs from traditional downsampling and interpolation methods by preserving key transition points and avoiding approximation errors. The FT was applied in the proposed FT before the DL model was trained, as shown in Figure 5.2. To minimise dataset size and preserve essential information, the FT remove redundant and duplicate values. This filtered dataset feeds the GRU-based DL model. The GRU layers, which capture sequential dependencies, may work more efficiently without losing relevant learning information. This integration showed a significant reduction in dataset size, 85.73% and 86.04% decrease in memory usage. This reduction demonstrates that it is lower in computational operating cost, can be advantageous for real-time BMS applications where energy efficiency is critical. Compared to conventional interpolation-based filtering methods, it achieves better estimation performance while significantly minimizing processing power. The actual and filtered dataset points in the different datasets, B1, B2, B05, B06, B07, and B18, are 60285, 63972, 50285, 44354, 48299, and 31991, respectively, as shown in Figure 5.3. It is important to note that, to visualize data points, the datasets are shown as SOH vs. time (sec). Table 5.2 shows the notable reductions in both dataset size and memory usage that occurred when the filtering technique was implemented on the original datasets on various datasets.

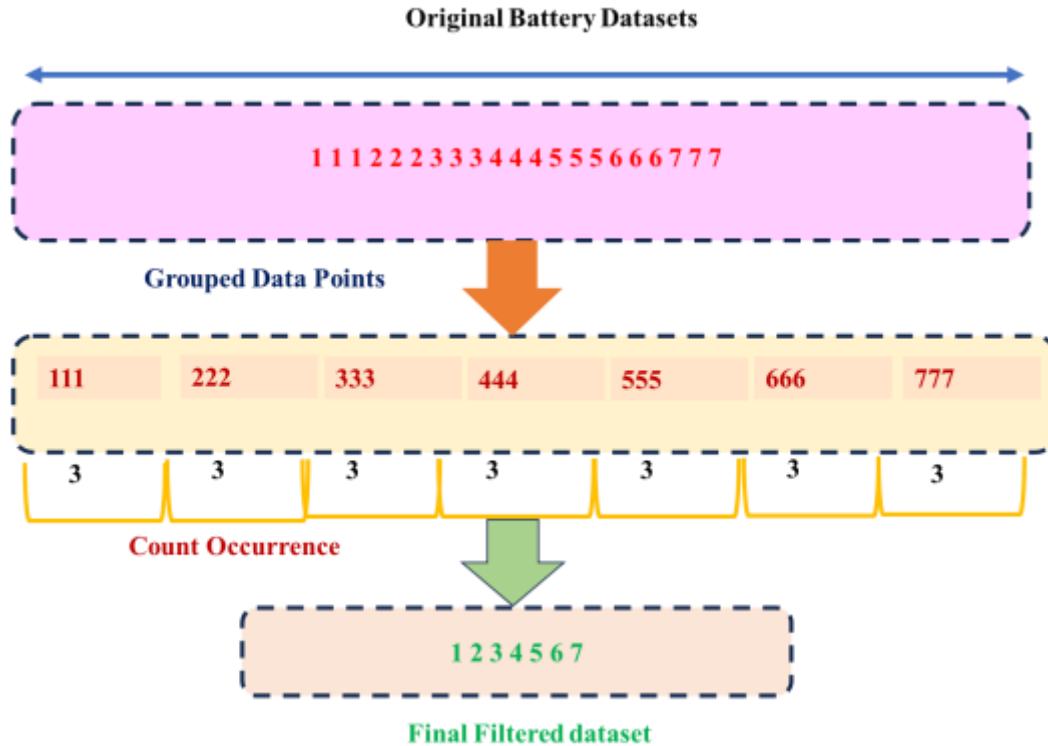


Figure 5.2 The proposed filter technique

For example, the memory used decreased by 86.04%, from 387 KB to 54 KB, and the size of the B1 dataset decreased by 85.71%, from 60,285 values to 8,609. The B2 dataset experienced an 85.72% reduction in memory utilization from 393 KB to 57 KB and an 80.49% decrease in size from 63,972 to 9,135 values. The size of the B05 dataset decreased by 85.73%, from 50,284 to 7,176 values, and memory utilization decreased by 85.63%, from 383 KB to 55 KB. The size of the B06 dataset decreased by 85.72%, from 44,354 to 6,333 values, and memory utilization decreased by 85.59%, from 347 KB to 50 KB. The size of the B07 dataset decreased by 85.72%, from 48,299 to 6,896 values, and memory utilization decreased by 85.67%, from 377 KB to 54 KB. The size of the B18 dataset decreased by 85.72%, from 31,991 to 4,567 values, and memory utilization decreased by 85.65%, from 251 KB to 36 KB. The DL models benefit significantly from these reductions in training computational energy and power consumption.

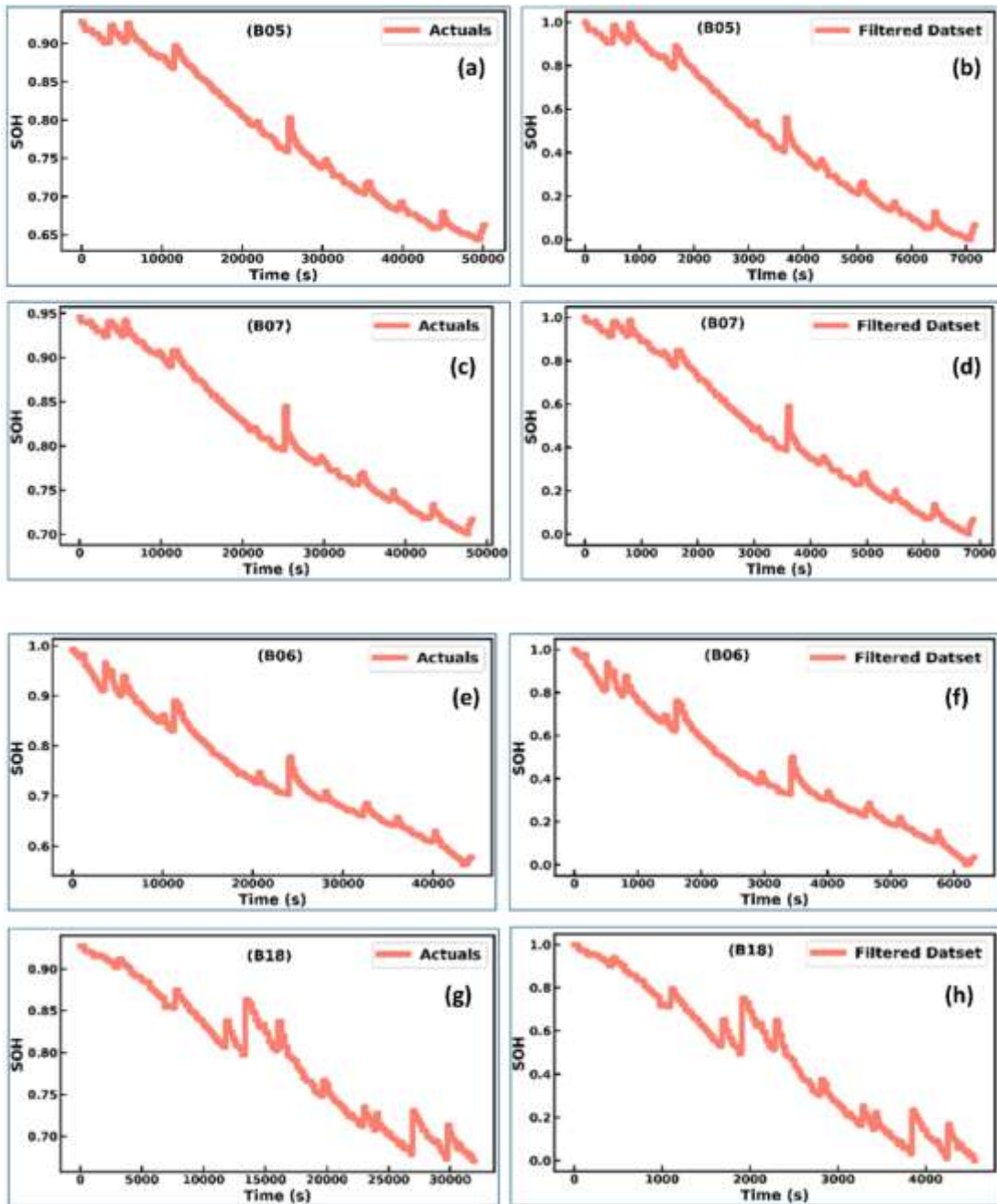


Figure 5.3 Actual datasets (a, c, e, and g) and datasets with the filter techniques (b, d, f, and h).

Reduced memory utilization is one of the most significant benefits of AI models because this makes it possible to run on low-resource hardware, making them more affordable and significant to larger range of devices and applications.

Table 5. 2 Data description with and without filter techniques

Datasets	Actual Dataset Points	Filtered Dataset Points	Percentage Reduction (%)	Memory Used (Actual dataset)	Memory Used (Filtered dataset)	Percentage Reduction (%)
B1	60285	8609	85.71	387 KB	54 KB	86.04
B2	63972	9135	85.72	393 KB	57 KB	85.49
B05	50285	7176	85.73	383 KB	55 KB	85.63
B06	44354	6333	85.72	347 KB	50 KB	85.59
B07	48299	6896	85.72	377 KB	54 KB	85.67
B18	31991	4567	85.72	251 KB	36 KB	85.65

These efficiencies are crucial in driverless cars, medical diagnostics, and IoT devices. Where massive processing of data and immediate efficiency are required. This increases implementation on low-power embedded systems used in BMS without affecting model accuracy. Reduced memory requirements increase device lifespan, allow longer-term data logging, and facilitate predictive maintenance without frequent data unloading, improving real-time monitoring efficiency and reliability.

5.3.2 Proposed Techniques

The implementation process of SOH estimation using the GRU and BiGRU models is presented with an in-depth overview of traditional RNNs.

5.3.2.1 Recurrent Neural Networks

The analysis of past data, which is essential for sequential development handling tasks like decoding phrases or sentences, creating subtitles for visual inputs, and so forth, is not possible with a conventional feed-forward neural network. The typical neural network is unable to manage the varied input and output sizes seen in these applications. Recurrent units are used by RNN [124] to store knowledge from the past to handle sequential input, in contrast to feed-forward neural networks. The feedback loop of the recurrent unit is shown in Figure 5.4. If the unit is activated, the hidden state h_k is updated by:

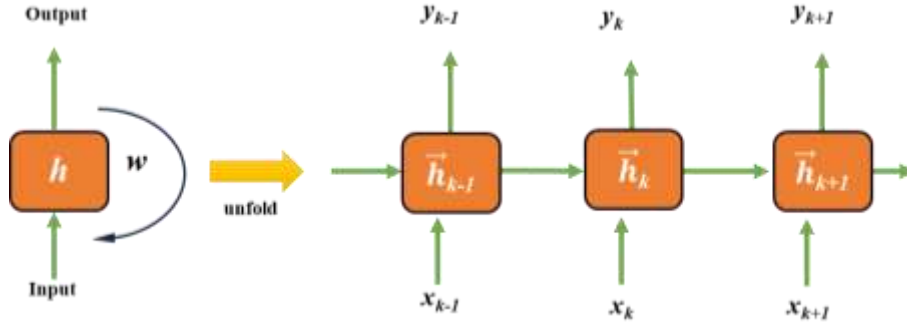


Figure 5.4 Structure of the RNN

$$h_k = \begin{cases} 0, & k = 0 \\ \Phi(h_{k-1}, X_k), & \text{Otherwise}' \end{cases} \quad (5.8)$$

x_k is the k^{th} input vector and Φ is a nonlinear function, such as the combination of an affine transformation and a logistic sigmoid. The update of the hidden state in Equation (5.9) is implemented practically as follows:

$$h_k = g(W_h * [X_k, h_{(k-1)}] + b_h) \quad (5.9)$$

where b_h is a bias parameter that represents an offset of each node; W_h is a weight matrix between a hidden layer and an input layer; and g is a smooth, bounded activation function, such as a logistic sigmoid function or a hyperbolic tangent function. Following, the corresponding output y_k may be acquired by:

$$y_k = g(W_h * h_k + b_y) \quad (5.10)$$

RNNs are particularly good at tasks like voice recognition and linked handwriting identification because of their time-step recurrent edge.

5.3.2.2 Gated Recurrent Unit Architecture

To resolve the issue of long-term dependence, the GRU [19] is suggested. Unlike a regular RNN, the GRU does not immediately change the current hidden state h_k based on the prior hidden state $h_{(k-1)}$ or the current input X_k . Rather, the GRU makes use of an update gate to decide how much historical data should be retained and a reset gate to decide how much data should be erased. The overall structure of the GRU is seen in Figure 5.5, where a candidate state \hat{h}_t and the prior state h_{k-1} are combined linearly to activate the GRU:

$$h_k = (1 - z_k) * h_{(k-1)} + z_k * \tilde{h}_k \quad (5.11)$$

In this case, z_k is referred to be the update gate, and sigmoid function activates it:

$$z_k = \text{sigmoid}(W_z * [X_k, h_{(k-1)}]) \quad (5.12)$$

The present state depends more on the candidate state if an entry of z_k is near to 1, while the former state is more dependent on the current state if an entry is close to 0. z_k intuitively ascertains the appropriate percentage of the applicant state to be admitted. The following formula is used to determine the GRU candidate state:

$$\hat{h}_k = \tanh(W_h * [X_k, h_{(k-1)} * r_k]) \quad (5.13)$$

When a sigmoid function activates the reset gate, denoted by r_k :

$$r_k = \text{sigmoid}(W_r * [X_t, h_{(k-1)}]) \quad (5.4)$$

The reset gate limits the influence of the previously concealed state on the candidate state, much as the update gate does. The GRU has the authority to choose what should be updated and what should be reset, while the typical RNN requires the recurrent unit to update in an exponential-moving-average manner.

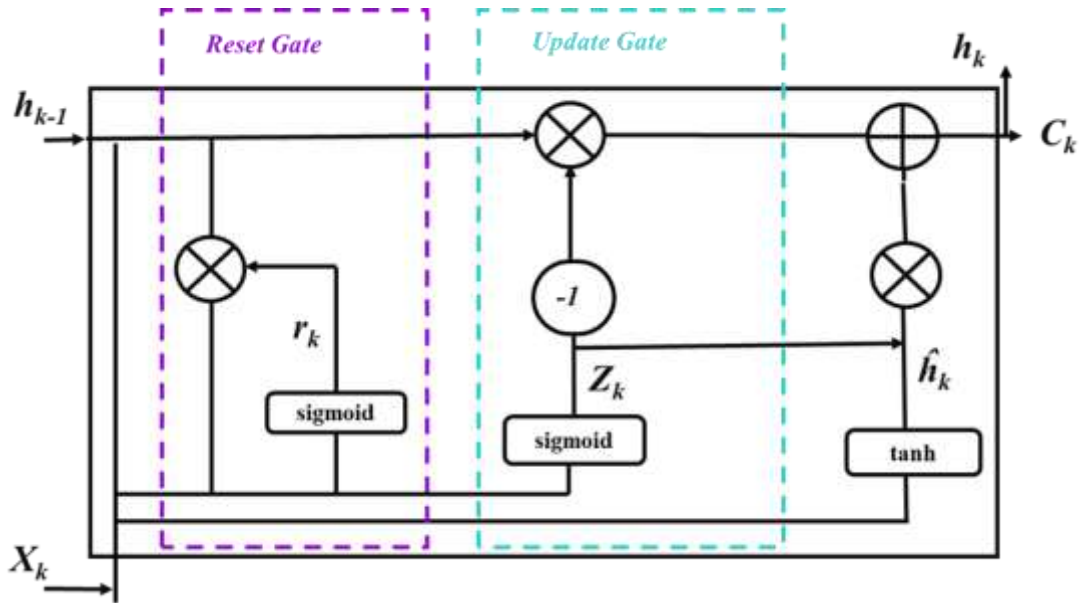


Figure 5.5 Structure of the GRU

Furthermore, the hidden unit output travels a relatively long way up the enlarged chain if the gating factor is near to 1. Since mistakes may also spread backward across several temporal stages, the gradient vanishing phenomena can also be significantly prevented in the meantime. The ability to capture long-term dependencies then arises.

5.3.2.3 Bidirectional Gated Recurrent Unit Architecture

The RNN's issues may be successfully resolved by the GRU, which can also identify long-term dependencies. Nevertheless, some of the accessible information is unavoidably lost in the forward transmission of previous data, However, the BiGRU is capable of handling this problem. Figure 5.6 shows the structure of the BiGRU. It is made up of two layers: one for forward propagation and the other for reverse propagation. When it comes to computation, the forward propagation layer works from time 1 to time t, while the backpropagation layer works backwards from time t to time 1. Lastly, the dense layers are concurrently linked to the anticipated outputs of the forward propagation layer and the backpropagation layer.

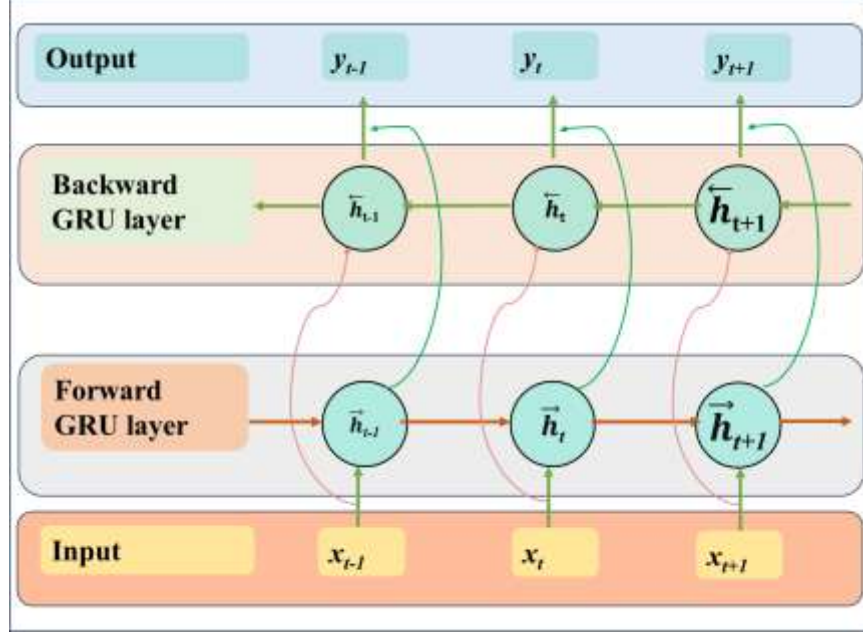


Figure 5.6 Structure of the BiGRU

By making up for the shortfalls of the one-way GRU, the BiGRU enables the GRU to learn the data from the input time series more quickly and provide reliable prediction results. The impact is stronger and more noticeable as the input time series grows. Besides, it makes sense to employ the BiGRU for the SOH estimate since the battery voltage, current, and temperature at the input are all time series. The following in equation (5.15-5.16) with arrows involved to represent i.e., \rightarrow and \leftarrow , which signify the forward and backward processes, respectively. The forward and backward processes are defined by a set of parameters $\vec{\Theta}_{BiGRU}$ and $\bar{\Theta}_{BiGRU}$ respectively.

$$\vec{h}_k = f(X_k, \vec{h}_{(k-1)}; \vec{\Theta}_{BiGRU})$$

$$= \begin{cases} \vec{z}_k = \text{sigmoid}(\vec{W}_z * [X_k, \vec{h}_{(k-1)}] + \vec{b}_z) \\ \vec{r}_k = \text{sigmoid}(\vec{W}_r * [X_k, \vec{h}_{(k-1)}] + \vec{b}_r) \\ \hat{h} = \tanh(\vec{W}_h * [X_k, \vec{h}_{(k-1)}] \odot \vec{r}_k) + \vec{b}_h \\ \vec{h}_k = (1 - \vec{z}_k) \odot \vec{h}_{(k-1)} + \vec{z}_k \odot \hat{h} \end{cases} \quad (5.15)$$

$$\bar{h}_k = f(X_k, \bar{h}_{(k-1)}; \bar{\Theta}_{BiGRU})$$

$$= \begin{cases} \bar{z}_k = \text{sigmoid}(\bar{W}_z * [X_k, \bar{h}_{(k-1)}] + \bar{b}_z) \\ \bar{r}_k = \text{sigmoid}(\bar{W}_r * [X_k, \bar{h}_{(k-1)}] + \bar{b}_r) \\ \hat{h} = \text{tanh}(\bar{W}_r * [X_k, \bar{h}_{(k-1)}] \odot \bar{r}_k) + \bar{b}_h \\ \bar{h}_k = (1 - \bar{z}_k) \odot \bar{h}_{(k-1)} + \bar{z}_k \odot \hat{h} \end{cases} \quad (5.16)$$

These parameters are shared by all degradation cycles and are learned during model training.

$\vec{h}_{(k-1)}$ represents hidden states of degradation cycle at time "t-1". The bias weights of the forward and backward process are represented by " $\vec{b}_{z,r,h}$ ", and " $\overleftarrow{b}_{z,r,h}$ ". The input weights of forward and backward process are represented by " $\vec{W}_{z,r,h}$ ", and " $\overleftarrow{W}_{z,r,h}$ ". The nonlinear activation functions are represented by "sigmoid" and "tanh" hyperbolic tangent, however multiplication of two vectors is denoted by the symbol " \odot ".

5.4 EXPERIMENTAL SETUP AND DATASET

Battery aging tests were conducted using Chroma 17020 battery tester with Chroma 17020 software as shown in Figure 5.7. Two batteries, namely B1 and B2, were tested under ambient conditions using the constant current constant voltage (CCCV) Charge and discharge protocol. The batteries technical parameters are listed in Table 5.3 and initial capacity variances were maintained under 1%. The experimental setup includes HP Victus laptop with an NVIDIA GeForce GTX 1650 GPU (TDP) and 16 GB of RAM running Windows 11 with the Python based TensorFlow environment. The energy consumption was estimated by using GPU power data from nvidia-smi and computational time. Energy consumption was calculated based on the GPU's TDP and the average execution time during model training and inference. Min-Max normalization was applied to maintain data indicator comparability equation 5.17. Moreover, it can enable the network to update the parameters faster during training.

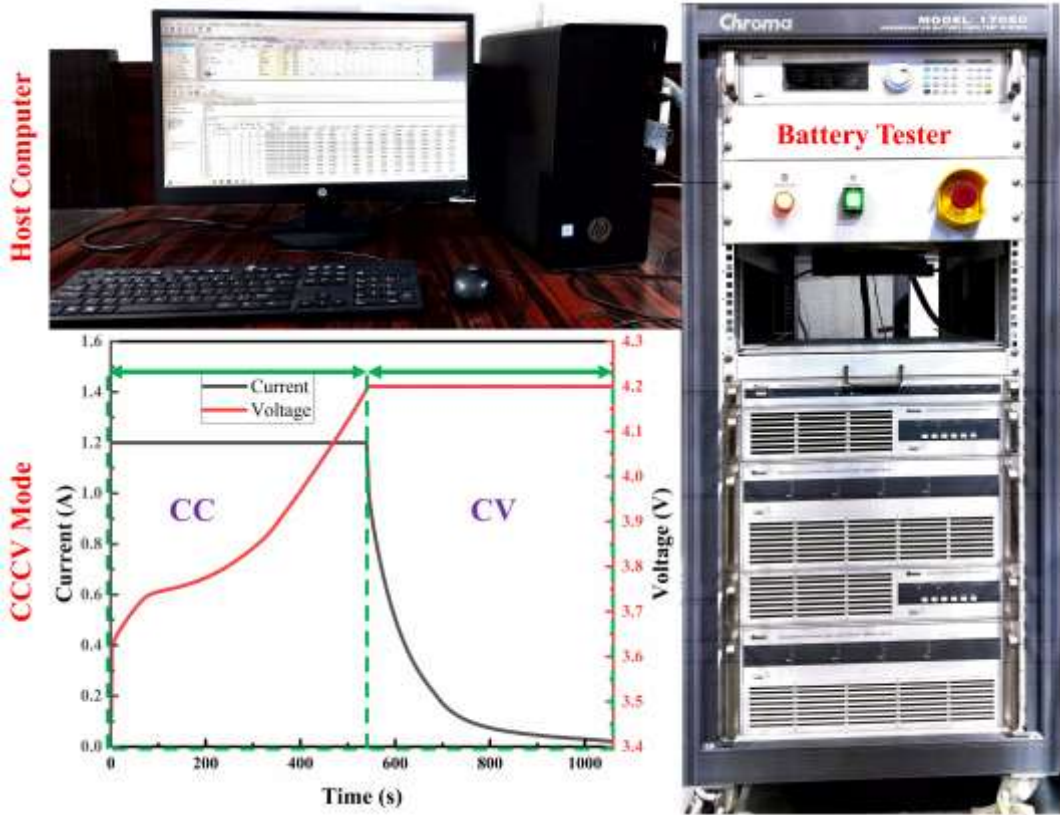


Figure 5.7 Experimental setup for lithium-ion battery testing

$$\hat{x}_t = \frac{x_t - x_{t,min}}{x_{t,max} - x_{t,min}} \quad (5.17)$$

When x_t is the battery operating parameter at time t , \hat{x}_t is the normalized feature value, $x_{t,min}$ is the input parameter's minimum value, and $x_{t,max}$ is the input parameter maximum value. The following evaluation metrics are used in this investigation to quantify the effectiveness of the SOH estimation model. MAE, MAE, RMSE, and the determination coefficient R^2 verify the estimation accuracy of the proposed models are calculated by equation 5.18-5.21, respectively.

$$MAE = \frac{1}{N} \sum_{t=1}^N |SOH_t - SOH'_t| \quad (5.18)$$

$$MSE = \frac{1}{N} \sum_{t=1}^N (SOH_t - SOH'_t)^2 \quad (5.19)$$

$$RMSE = \sqrt{\frac{1}{N} \sum_{t=1}^N (SOH_t - SOH'_t)^2} \quad (5.20)$$

$$R^2 = 1 - \frac{\sum_k (SOH'_t - SOH_t)^2}{\sum_k (SOH_t - \overline{SOH})^2} \quad (5.20)$$

$$MaxError = \max | SOH_t - SOH'_t | \quad (5.21)$$

"N" number of windows, arithmetic mean of the actual value is \overline{SOH} . The actual value "SOHt", and the models estimated the value is SOH'_t .

Table 5. 3 Technical Specification of LIBs

Battery	Type
Format	Cylindrical
Chemistry	LFP and NMC
Rated Capacity	5.0 Ah
Normalized Resistance	14 mΩ
Specific Power and Energy	7.3 & 134k W/kg
Energy Density	329 Wh/l

5.4.1 Battery Data Diversity Analysis

To employ DL models for SOH estimation, it is necessary to analyse the correlations among features, such as voltage, current, temperature, capacity, and SOH. Its influence on SOH estimation within the collected dataset. The significance of correlation analysis is its ability to identify redundant and irrelevant data to improve the performance of AI models. Therefore, the most correlated features and how they relate to SOH estimation must be determined. The correlation matrix displays the resultant matrix as shown in Figure 5.8. It exhibits temperature, voltage, current, and SOH correlation of six different dynamic SOH patterns. Upon examination of the correlation matrix, it was found that a few more correlated features in the dataset might potentially cause multicollinearity and instabilities within the proposed model.

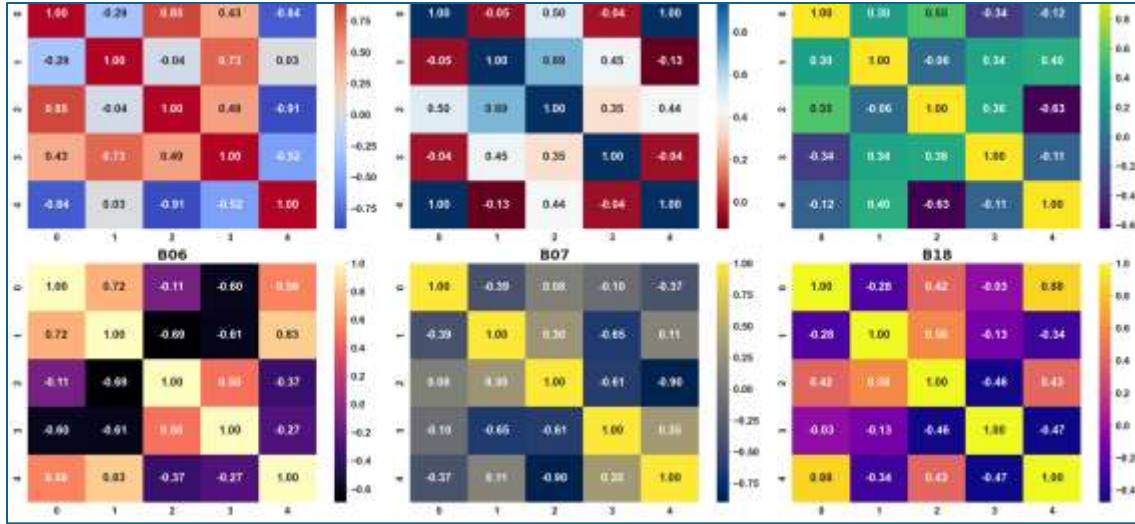


Figure 5.8 The correlation matrix of four different SOH datasets: B1, B2, B05, B06, B07, and B18

5.5 RESULTS AND DISCUSSIONS

The primary objective of this thesis is to minimize unnecessary training time in DL models, which leads to excessive energy consumption. For instance, in SOH estimation of LIBs, a large number of redundant, highly similar data points exist within a single cycle, as shown in Figure 5.3. These redundant values unnecessarily increase dataset size and memory utilization, thereby contributing to higher computational and energy demands. When SOH estimation is performed over an extended number of cycles, DL models require large parameters and computational resources, further exacerbating energy consumption. Therefore, it is essential to eliminate redundant values and retain only the most relevant data to enhance model efficiency while reducing energy overhead.

5.5.1 Performance Analysis of Each Dataset with the Filtering Technique

The FT was integrated with five DL architectures: FT-GRU, FT-BiGRU, FT-SBiGRU, FT-GRU-BiGRU, and FT-GRU-SBiGRU and tested across six dynamic datasets B1, B2, B05, B06, B07, and B018, as illustrated in Figure 5.9(a–f).

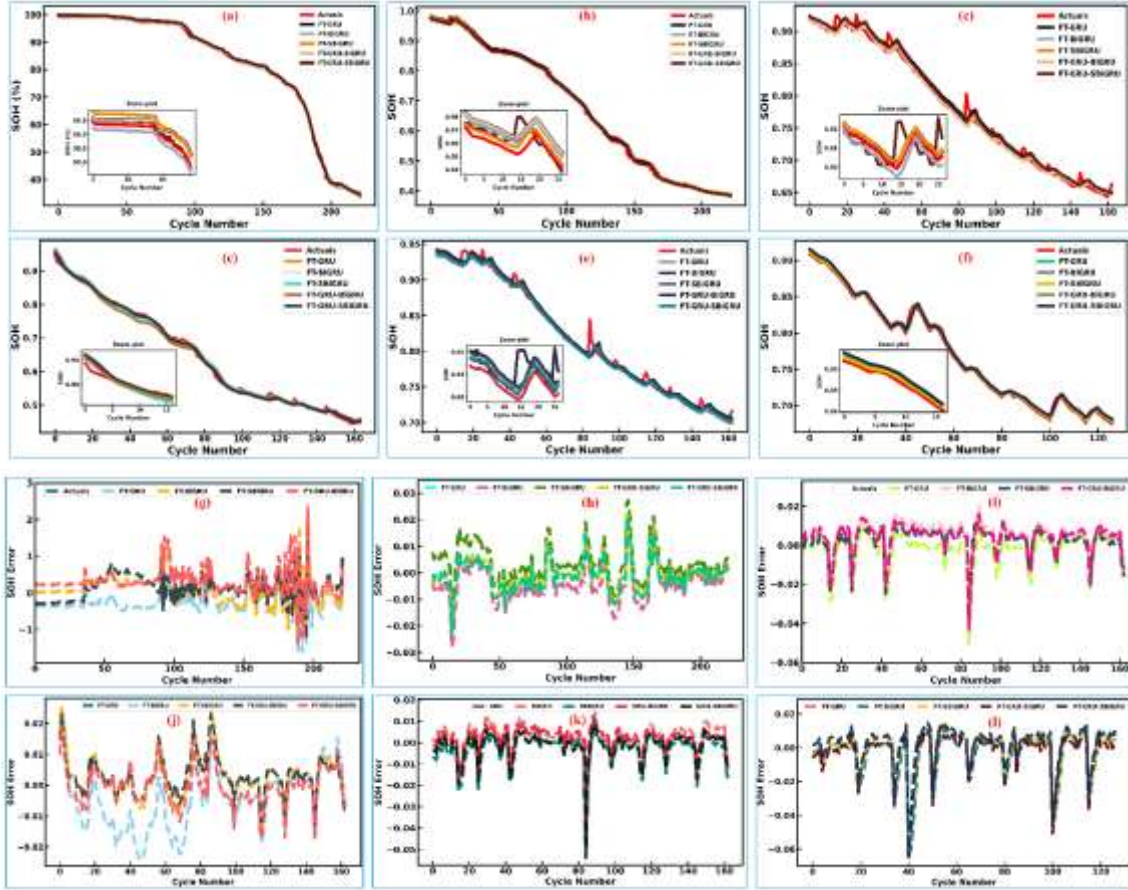


Figure 5.9 SOH estimation result (a-f) and estimation errors with the FT (g-l), (a) B1, (b) B2, (c) B05, (d) B06, (e) B07, (f) B018, datasets.

Performance was assessed using MAE, MSE, RMSE, R^2 , and maximum error in Table 5.4. Overall, the FT improved SOH estimation accuracy across all datasets, while also reducing training complexity and computational overhead. Among the tested models, FT-GRU consistently achieved the best performance, offering the lowest error metrics and highest correlation with real data.

5.5.1.1 Performance on B1-B2 and B05-B018 Dataset

FT-GRU achieved the most accurate results, with improvements of 92.75% of MAE, 99.49% of MSE, 75.96% of RMSE, and 94.45% of maximum error with the B1 dataset. The R^2 value of 99.90% confirmed strong correlation with experimental data, highlighting FT-GRU's robustness in capturing battery degradation patterns.

Table 5. 4 The statistical performances of the proposed models with FT

Datasets	Approaches	MAE	MSE	RMSE	R ²	Maximum Error
B1	FT-GRU	0.0004	2.7712e-07	0.0005	0.9990	0.0023
	FT-BiGRU	0.0049	4.5286e-05	0.0067	0.9889	0.0379
	FT-SBiGRU	0.0051	4.6333e-05	0.0068	0.9888	0.0341
	FT-GRU-BiGRU	0.0058	5.1622e-05	0.0007	0.9987	0.0473
	FT-GRU-SBiGRU	0.0085	9.5444e-05	0.0097	0.9977	0.0531
B2	FT-GRU	0.0003	2.2735e-07	0.0004	0.9992	0.0026
	FT-BiGRU	0.0041	3.4388e-05	0.0056	0.9986	0.0325
	FT-SBiGRU	0.0052	5.4551e-05	0.0073	0.9987	0.0398
	FT-GRU-BiGRU	0.0060	5.6852e-05	0.0075	0.9986	0.0482
	FT-GRU-SBiGRU	0.0077	8.3263e-05	0.0095	0.9980	0.0501
B05	FT-GRU	0.0004	2.6442e-07	0.0005	0.9931	0.0053
	FT-BiGRU	0.0045	6.8848e-05	0.0082	0.9920	0.0698
	FT-SBiGRU	0.0051	7.5060e-05	0.0086	0.9913	0.0703
	FT-GRU-BiGRU	0.0063	8.3721e-05	0.0091	0.9903	0.0774
	FT-GRU-SBiGRU	0.0082	9.1009e-05	0.0095	0.9895	0.0983
B06	FT-GRU	0.0004	2.9044e-07	0.0005	0.9984	0.0020
	FT-BiGRU	0.0049	4.5583e-05	0.0067	0.9979	0.0282
	FT-SBiGRU	0.0055	5.6735e-05	0.0075	0.9974	0.0356
	FT-GRU-BiGRU	0.0063	6.3388e-05	0.0079	0.9971	0.0410
	FT-GRU-SBiGRU	0.0065	7.5806e-05	0.0087	0.9965	0.0538
B07	FT-GRU	0.0003	2.1557e-07	0.0004	0.9924	0.0053
	FT-BiGRU	0.0042	5.5943e-05	0.0074	0.9909	0.0455
	FT-SBiGRU	0.0052	5.2455e-05	0.0072	0.9915	0.0595
	FT-GRU-BiGRU	0.0058	6.7665e-05	0.0082	0.9890	0.0515
	FT-GRU-SBiGRU	0.0066	6.8588e-05	0.0082	0.9889	0.0780
B018	FT-GRU	0.0001	3.5390e-08	0.0001	0.9875	0.0023
	FT-BiGRU	0.0012	2.4616e-06	0.0015	0.9897	0.0443
	FT-SBiGRU	0.0017	5.1377e-06	0.0022	0.9691	0.0820
	FT-GRU-BiGRU	0.0020	7.6331e-06	0.0027	0.9701	0.0903
	FT-GRU-SBiGRU	0.0050	5.1209e-05	0.0071	0.9731	0.0997

*The bold represents the best results.

FT-GRU again outperformed all other models on the B2 dataset, recording improvements of 93.07% of MAE, 74.72% of MSE, and 70.53% of RMSE, with an R² of 99.92%. These results demonstrate the model's adaptability to dynamic operating conditions. The performances of the proposed model with the B05 dataset achieved 92.91% of MAE, 74.76% of MSE, and 70.74% of RMSE, with an R² of 99.31%. This indicates high precision while maintaining efficiency, validating its suitability for BMS applications. FT-GRU maintained superior accuracy with 92.48% MAE, 74.66% of MSE, and 69.94% of RMSE on B06 dataset. The R² value of 99.84% reflects excellent predictive strength and consistency across datasets. Results revealed improvements of 92.09% of MAE, 74.73% of MSE, and 70.55% of RMSE, with an R² of 99.24%. FT-GRU continued to demonstrate robust

generalization capacity under varied operating conditions on the B07 dataset. Despite the dataset's complexity, FT-GRU achieved strong predictive capability with improvements of 70.16% of MAE, 74.69% of MSE, and 70.46% of RMSE, with a maximum error reduction of 96.78% and R^2 of 99.24% on the B018 dataset.

5.5.2 Performance Analysis of Each Dataset without Filtering Technique

This subsection evaluates the SOH estimation performance of the GRU model across six different datasets (B1, B2, B05, B06, B07, and B018) without applying the FT. The numerical results are summarised in Table 5.5, while Figure 5.10(a–f) presents SOH estimation curves and Figure 5.10(g–l) shows estimation errors.

5.5.2.1 Performance on B1 Dataset

The GRU model achieved the best performance on the B1 dataset compared to other approaches. Improvements were observed in terms of MAE 34.18%, MSE 46.32%, RMSE 30.16%, and maximum error 46.42%. The reduction in maximum error highlights the model's ability to minimize extreme deviations between estimated and actual SOH values. Additionally, all models demonstrated strong correlations between predicted and actual SOH, with R^2 values ranging from 99.78% to 99.95%, with the highest at 99.95% for the GRU approach. This confirms the reliability of GRU for the B1 dataset. For the B2 dataset, the GRU outperformed baseline models, achieving 29.60% improvement in MAE, 48.84% in MSE, 30.72% in RMSE, and 54.58% in maximum error in Table 5.5. These results demonstrate that the GRU maintains high accuracy and effectively reduces error rates under varying cycling conditions. On the B05 dataset, the GRU achieved 37.08% MAE, 53.89% MSE, 37.97% RMSE, and 52.23% maximum error improvements over other approaches. The substantial MSE reduction across all cycles indicates the GRU's robustness in capturing degradation patterns.

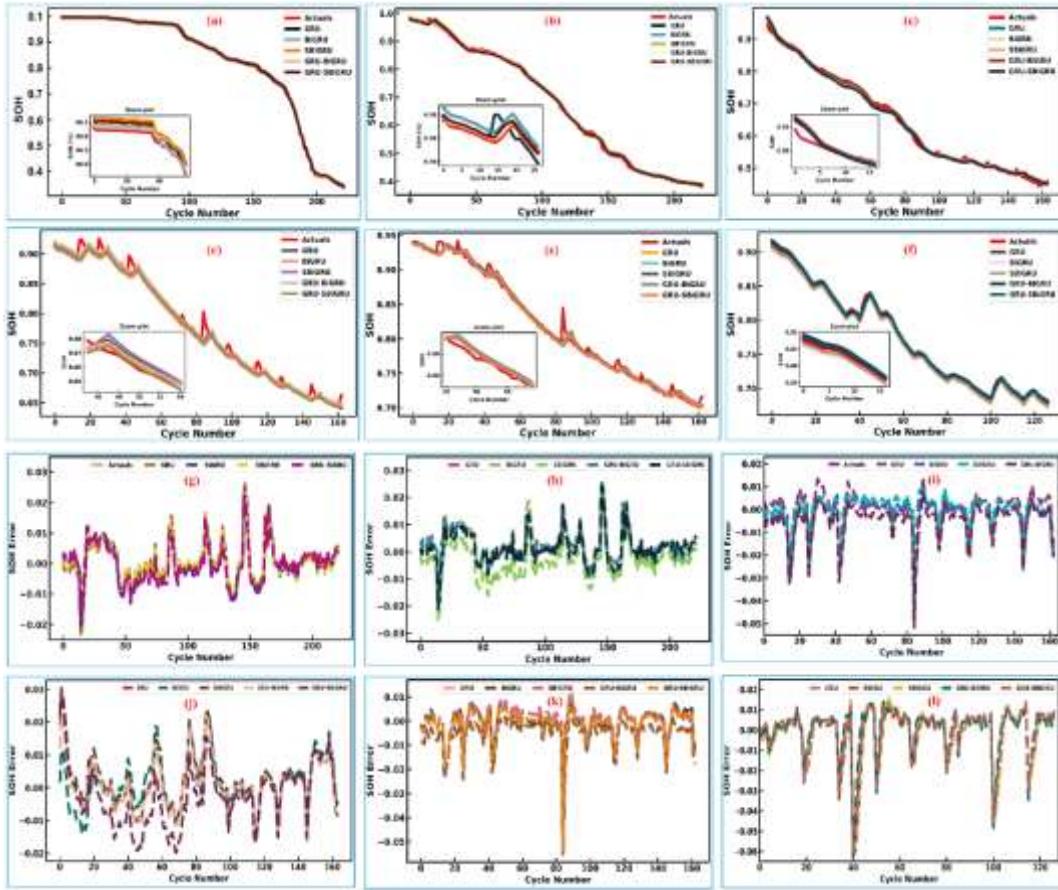


Figure 5.10 The SOH estimation result (a-f) and estimation errors without incorporation filter technique (g-l), (a) B1, (b) B2, (c) B05 (d) B06, (e) B07, (f) B018 datasets

The R^2 values ranged between 98.89% and 99.17%, further validating model accuracy. The GRU consistently provided the lowest MAE and RMSE on the B06 dataset. Average improvements were 32.19% of MAE, 43.89% of MSE, 46.34% of RMSE, and 38.69% of maximum error compared to existing methods. High R^2 values of 98.90%–99.26% confirmed the reliability of SOH predictions for this dataset. The B07 dataset recorded the highest RMSE improvement of 62.30% among all datasets. Overall, the GRU achieved 37.60% MAE, 56.37% MSE, and a 42.57% improvement in maximum error. This demonstrates the GRU’s strength in mitigating large deviations, enhancing prediction stability. For the B018 dataset, the GRU delivered the best improvements: 43.21% in MAE, 55.28% in MSE, 37.42% in RMSE, and 52.26% in maximum error.

Table 5. 5 The statistical performances of proposed models without FT

Datasets	Approaches	MAE	MSE	RMSE	R ²	Maximum Error
B1	GRU	0.3256	0.2085	0.4566	0.9995	0.2429
	BiGRU	0.3670	0.2450	0.4950	0.9994	0.3471
	SBiGRU	0.4367	0.4159	0.6449	0.9990	0.3935
	GRU-BiGRU	0.6055	0.8767	0.9363	0.9979	0.548
	GRU-SBiGRU	0.7015	0.8871	0.9418	0.9978	0.6346
B2	GRU	0.4585	0.2333	0.4830	0.9094	0.3891
	BiGRU	0.5623	0.3460	0.5882	0.8854	0.7105
	SBiGRU	0.6989	0.5242	0.7240	0.8901	0.869
	GRU-BiGRU	0.7597	0.6161	0.7849	0.8770	0.9288
	GRU-SBiGRU	0.7938	0.6713	0.8193	0.8935	0.9675
B05	GRU	0.1758	0.0310	0.1762	0.9889	0.2094
	BiGRU	0.2769	0.0968	0.3111	0.9917	0.4941
	SBiGRU	0.3720	0.1657	0.4071	0.9896	0.6222
	GRU-BiGRU	0.4518	0.2357	0.4855	0.9911	0.7188
	GRU-SBiGRU	0.4717	0.2545	0.5045	0.9915	0.7406
B06	GRU	0.2440	0.0726	0.2695	0.9926	0.4222
	BiGRU	0.3232	0.1228	0.3504	0.9920	0.5325
	SBiGRU	0.5143	0.2967	0.5447	0.9893	0.7842
	GRU-BiGRU	0.6157	0.4186	0.6470	0.9890	0.9118
	GRU-SBiGRU	0.6353	0.4447	0.6668	0.9900	0.9368
B07	GRU	0.3306	0.1287	0.3587	0.9889	0.4303
	BiGRU	0.3081	0.1168	0.1168	0.9913	0.4874
	SBiGRU	0.5793	0.3685	0.6070	0.9824	0.7351
	GRU-BiGRU	0.6729	0.4870	0.6979	0.9909	0.8316
	GRU-SBiGRU	0.7615	0.6195	0.78713	0.9911	0.9319
B018	GRU	0.2662	0.0844	0.2905	0.9921	0.3097
	BiGRU	0.3115	0.1193	0.34541	0.9917	0.5379
	SBiGRU	0.4302	0.2040	0.4517	0.9915	0.5475
	GRU-BiGRU	0.7401	0.5859	0.7654	0.9901	0.9075
	GRU-SBiGRU	0.9075	0.3654	0.60452	0.9924	0.7255

**The bold are represented best results.*

These results highlight its robustness in reducing estimation errors consistently, even under advanced ageing conditions. Across all datasets, the GRU model consistently outperformed alternative approaches without FT. Improvements ranged from 29% to 43% in MAE, 44% to 56% in MSE, and up to 62% in RMSE, with strong R² correlations above 98.8%. This demonstrates its reliability for SOH estimation across diverse battery cycling and ageing conditions.

5.5.3 Energy Efficiency and Computational Cost Evaluation

Traditional DL models demand significant computational resources for training and inference, resulting in high energy consumption and increased carbon footprint. The integration of the FT

into the DL framework addresses these limitations by enhancing energy efficiency and reducing computational cost, aligning with Green AI objectives, as shown in Table 5.6. A comparative evaluation was carried out across multiple SOH datasets to analyze the computational efficiency of models with and without FT. The performance indicators considered were computational time, active power, and total energy consumption. The FT-GRU model achieved substantial reductions in computational time, showing improvements of 56.42%, 57.69%, 63.15%, 57.14%, 54.54%, and 76.47% for the B01, B02, B05, B06, B07, and B018 datasets, respectively. Corresponding reductions in energy consumption were 69.50%, 67.65%, 75.58%, 69.20%, 65.98%, and 82.38%. These results highlight that the proposed approach not only improves prediction accuracy but also significantly decreases computational burden and energy demand. The findings demonstrate the practical potential of FT-enhanced models for real-time applications in BMS, where both accuracy and efficiency are critical.

5.5.4 Comparison and Discussion of Different Approaches with and Without FT

This section presents a comparative evaluation of DL models across multiple dynamic datasets, both with and without the FT. The analysis considers key performance indicators, including MAE, MSE, RMSE, maximum error, computation time, and R^2 , to highlight the practical benefits of FT integration. The statistical outcomes are summarized in Tables 5.4, 5.5 and 5.6. The results show that incorporating FT consistently improves model accuracy and efficiency. The FT-GRU model achieved the most notable performance, with improvements of 91.42% in MAE, 99.61% in MSE, and 93.73% in RMSE, while maintaining R^2 values close to unity. These results demonstrate the model's strong predictive ability and its reliability for SOH estimation across diverse operating

conditions. In addition to accuracy, the FT-GRU approach substantially reduces computational demands.

Table 5. 6 Energy consumption and computational time comparisons of all models across all datasets

Datasets	Approaches	Comp. Time (Sec)	Power (P_{active}) (W)	Energy Consumption (Joules)	Approaches	Comp. Time (Sec)	Power (P_{active}) (W)	Energy Consumption (Joules)	Percentage Reduction (%)
B1	GRU	23	6.40	147.20	FT-GRU	10	4.49	44.90	69.50
	BiGRU	31	7.80	241.80	FT-BiGRU	16	5.03	80.48	66.72
	SBiGRU	43	8.50	365.50	FT-SBiGRU	20	6.13	122.60	66.46
	GRU-BiGRU	47	8.95	420.65	FT-GRU-BiGRU	22	6.58	144.76	65.59
	GRU-SBiGRU	55	9.53	524.15	FT-GRU-SBiGRU	26	7.08	184.08	64.88
B2	GRU	25	6.90	172.50	FT-GRU	11	5.073	55.80	67.65
	BiGRU	38	8.20	311.60	FT-BiGRU	15	5.91	88.65	71.55
	SBiGRU	57	9.67	551.19	FT-SBiGRU	21	6.82	143.22	74.02
	GRU-BiGRU	63	9.80	617.40	FT-GRU-BiGRU	26	7.05	183.30	70.31
	GRU-SBiGRU	71	10.13	719.23	FT-GRU-SBiGRU	31	7.43	230.33	67.98
B05	GRU	19	6.17	117.23	FT-GRU	7	4.09	28.63	75.58
	BiGRU	27	6.72	181.44	FT-BiGRU	11	4.79	52.69	70.96
	SBiGRU	49	7.51	367.99	FT-SBiGRU	18	5.98	107.64	70.75
	GRU-BiGRU	55	8.97	493.35	FT-GRU-BiGRU	23	6.53	150.19	69.56
	GRU-SBiGRU	65	10.37	674.05	FT-GRU-SBiGRU	28	6.97	195.16	71.05
B06	GRU	20	6.37	127.40	FT-GRU	9	4.36	39.24	69.20
	BiGRU	29	7.03	203.87	FT-BiGRU	13	5.10	66.30	67.48
	SBiGRU	39	8.34	325.26	FT-SBiGRU	18	5.83	104.94	67.74
	GRU-BiGRU	45	9.12	410.40	FT-GRU-BiGRU	20	6.17	123.40	69.93
	GRU-SBiGRU	51	9.97	508.47	FT-GRU-SBiGRU	22	6.55	144.10	71.66
B07	GRU	22	6.56	144.32	FT-GRU	10	4.91	49.10	65.98
	BiGRU	35	7.97	278.95	FT-BiGRU	15	5.53	82.95	70.26
	SBiGRU	44	8.45	371.80	FT-SBiGRU	19	6.01	114.19	69.29
	GRU-BiGRU	56	9.05	506.80	FT-GRU-BiGRU	24	6.47	155.28	69.36
	GRU-SBiGRU	67	10.07	674.69	FT-GRU-SBiGRU	27	7.05	190.35	71.79
B018	GRU	16	5.49	87.84	FT-GRU	4	3.87	15.48	82.38
	BiGRU	29	6.87	199.23	FT-BiGRU	11	5.08	55.88	71.95
	SBiGRU	34	7.39	251.26	FT-SBiGRU	14	6.13	85.82	65.84
	GRU-BiGRU	48	8.09	388.32	FT-GRU-BiGRU	23	6.32	145.36	62.57
	GRU-SBiGRU	57	9.53	543.21	FT-GRU-SBiGRU	26	7.02	182.52	66.40

Improvements in computational time ranged from 25% to 70.76%, while reductions in energy consumption ranged from 69.50% to 82.38% compared to models without FT. Such enhancements are critical for real-time electric vehicle applications, where timely and resource-efficient SOH estimation directly influences battery management and operational safety. Overall, the FT-GRU method offers precise, reliable, and energy-efficient SOH estimation. By reducing computational overhead and energy consumption, it aligns with Green AI principles and supports the development of sustainable and scalable battery management solutions. Its adaptability across

datasets and driving conditions makes it highly suitable for next-generation electric vehicle applications.

5.5.5 Analysis of DL Model Reliability in Terms of Energy & Efficiency

To integrate Green AI methodologies into the DL model, it is critical to investigate energy efficiency and model accuracy. Therefore, the balance between performance and energy usage should be evaluated to identify how this filtering approach can enhance energy-efficient reliability. The DL models need significant computer resources for both training and inference. The reliable Green AI models must reduce energy usage while maintaining accuracy. Therefore, authors can establish the energy efficiency score (EES) to measure reliability in energy-efficient DL models as expressed in Equation 5.22. This evaluation encourages DL models through a balance of accuracy and energy use. It helps to identify the energy-efficient, robust DL models that are reliable across multiple datasets, raises sustainable research practices, and guides industries and researchers toward energy-efficient decision-making.

$$ESS = \frac{\text{Accuracy (\%)}}{\text{Energy Consumption (Joules)}} \quad (5.22)$$

R^2 is used for accuracy. Therefore, in this work $accuracy (\%) = R^2 \times 100$. The high ESS indicates that the models maintain accuracy while consuming less energy, ensuring stability. Comparison between GRU and FT-GRU models demonstrates that the application of FT significantly enhances energy efficiency while maintaining high predictive reliability. The EES improvements across datasets indicate that FT-GRU consistently outperforms GRU in energy-efficient DL model deployment. As shown in Table 5.7, the FT-GRU model consistently outperforms the conventional GRU across all datasets. For example, in the B1 dataset, energy consumption is reduced from 147.2 J to 44.9 J, with an EES improvement of 227.68%. In B2, energy consumption decreases from 172.5 J to 55.8 J, yielding a 239.65% improvement, while

accuracy rises from 90.94% to 99.92%. The B05 dataset records the highest gain of 311.20%, while the B018 dataset achieves the best overall EES of 3.4687 with a 464.81% improvement. Similar improvements are observed in the B06 and B07 datasets. These results confirm that FT-GRU significantly reduces energy consumption while maintaining high predictive reliability. The consistent improvements in EES across datasets, highlighted in Table 5.6, validate FT-GRU as a robust and sustainable alternative to conventional models for energy-efficient deployment in practical applications.

Table 5. 7 Energy consumption and computational time comparisons of all models across all datasets

Datasets	Approaches	Energy (Joules)	R2	Accuracy (%)	EES	ESS, Percentage improvement (%)
B1	GRU	147.2	0.9995	99.95	0.6790	227.68
	FT-GRU	44.9	0.9990	99.90	2.2249	
B2	GRU	172.5	0.9094	90.94	0.5272	239.65
	FT-GRU	55.803	0.9992	99.92	1.7906	
B05	GRU	117.23	0.9889	98.89	0.8436	311.20
	FT-GRU	28.63	0.9931	99.31	3.4687	
B06	GRU	127.4	0.9926	99.26	0.7791	226.57
	FT-GRU	39.24	0.9984	99.84	2.5443	
B07	GRU	144.32	0.9889	98.89	0.6852	194.97
	FT-GRU	49.10	0.9924	99.24	2.0212	
B018	GRU	87.84	0.9921	99.21	1.1294	464.81
	FT-GRU	15.48	0.9875	98.75	6.3792	

5.5.6 Key Findings and Contributions

The results demonstrate that the integration of the FT significantly enhances DL model performance for SOH estimation of LIBs. FT-GRU consistently outperforms conventional GRU models across all datasets, achieving higher accuracy, lower estimation errors, and stronger correlation with actual SOH values. Energy efficiency is also substantially improved, as evidenced by the energy efficiency score (EES) in Table 5.6, with reductions in energy consumption up to 464.81%. The approach reduces computational time and memory usage, making it suitable for

real-time and resource-constrained applications. Overall, FT-GRU provides a reliable, accurate, and energy-efficient solution, supporting sustainable Green AI practices in BMS.

5.5.7 Limitations of Proposed Approach

Despite its effectiveness, the proposed FT-GRU approach has certain limitations. First, the method relies on historical battery datasets, and its performance may be influenced by data quality and the availability of sufficient training cycles. Second, the FT may oversimplify highly dynamic datasets with rapid fluctuations, potentially removing subtle but important information. Third, while FT significantly reduces energy consumption and computational cost, extremely large-scale deployments or ultra-fast real-time applications may still face computational challenges. Finally, the approach has been validated on specific LIB chemistries and operating conditions, and its generalization to other battery types or extreme environmental conditions requires further investigation. These limitations suggest areas for future refinement and broader applicability of the method.

5.6 ROLE OF PROPOSED FT IN BMS

The proposed FT plays a critical role in enhancing BMS by improving the efficiency, accuracy, and sustainability of SOH estimation. By reducing redundant data and optimizing DL models, FT enables more reliable battery monitoring while lowering computational and energy requirements.

5.6.1 Real-Time Applicability of Proposed Algorithm

The FT-GRU framework is suitable for real-time SOH estimation in EVs and other battery-powered applications. By decreasing dataset size and computational overhead, the algorithm can provide fast and accurate predictions, supporting timely decisions for battery operation, maintenance, and safety interventions.

5.6.2 Deployment Considerations in Embedded Platforms

The reduced memory footprint and computational demand of FT-GRU make it compatible with embedded BMS platforms. The algorithm can be integrated into microcontrollers or edge devices, enabling efficient energy management without requiring high-performance computing hardware, which is essential for portable and automotive battery systems.

5.6.3 Advantages over Conventional Monitoring Methods

Compared to traditional empirical, electrochemical, and AI-based monitoring techniques, the FT-GRU approach gives superior accuracy, faster estimation, lower energy consumption, and better adaptability to dynamic operating conditions. These advantages make it a more sustainable and practical solution for modern BMS, aligning with Green AI principles and improving overall battery performance, safety, and lifecycle management.

5.7 CONCLUSION

This chapter quantitatively demonstrates the effectiveness of the proposed FT integrated with DL models for SOH estimation of LIBs. The FT-GRU model achieved the highest predictive performance across all datasets, with average improvements of 91.42% in MAE, 99.61% in MSE, 93.73% in RMSE, and up to 464.81% in the energy efficiency score (EES) compared to conventional GRU, as reported in Table 5.7. R^2 values consistently exceeded 99.2%, indicating strong correlation with actual SOH values. The FT reduced computational time by 54.54–76.47% and energy consumption by 65.98–82.38%, highlighting its suitability for real-time and embedded BMS applications. These results confirm that FT-GRU provides a reliable, accurate, and energy-efficient solution, capturing degradation trends under varying conditions while adhering to Green AI principles, thus offering a robust framework for next-generation BMS.

CHAPTER 6

AI-DRIVEN CONTROL STRATEGIES AND ANALYSIS OF OPERATING AND ENVIRONMENTAL CONDITIONS IN BATTERY STATE ESTIMATION

6.1 INTRODUCTION

The LIBs are widely used in EVs due to their long cycle life and efficiency. However, their performance is influenced by operating and environmental conditions such as temperature variation, dynamic load profiles, and long-term cycling. Further, the highly aggressive drive cycles increase stress and accelerate aging. These factors make it difficult to accurately estimate key battery states such as SOC, SOE, and SOH. Conventional BMS control strategies based on ECM and KFs techniques are less accurate in modelling nonlinear and real-time operating conditions. Therefore, there is a need to develop condition-aware estimation and control approaches. This chapter focuses on different AI-driven integrated adaptive control strategies for different state estimation under varying operating and environmental conditions. Green AI techniques, such as lightweight architectures and feature optimization, are discussed to reduce computational cost while maintaining accuracy.

6.2 AGING EFFECTS AND DEGRADATION UNDER DIFFERENT OPERATING STRESS

Battery aging under real-world EV conditions is influenced by factors such as temperature variation, cycling rate and dynamic profiles. These stressors accelerate electrochemical and mechanical degradation, leading to capacity fading, increased impedance, and safety risks, including lithium plating and gas generation. This section analyzes the impact of the operating

conditions on battery ageing and explores AI-based predictive control strategies to mitigate and improve long-term battery reliability.

6.3 Process of Machine Learning based SOH Estimation

The ML-based SOH estimation involves several key stages: data collection, preprocessing, feature extraction, model training, and performance evaluation as shown in Figure 6.1. Battery parameters such as voltage, current, temperature, and cycle data are collected to capture nonlinear degradation behaviour. Preprocessing of the raw datasets removes noise, outliers, and missing values, while the min-max normalisation standardises input features. The CNNs-based feature extraction identifies critical degradation patterns followed by model training using optimized learning algorithms. Model selection and hyperparameter tuning using grid search and the leave-one-out cross-validation (LOOCV) method to prevent overfitting and enhance generalization. Finally, performance was validated using evaluation metrics like MAE, MSE, RMSE, MaxError, and R^2 , ensuring reliable and accurate SOH estimation.

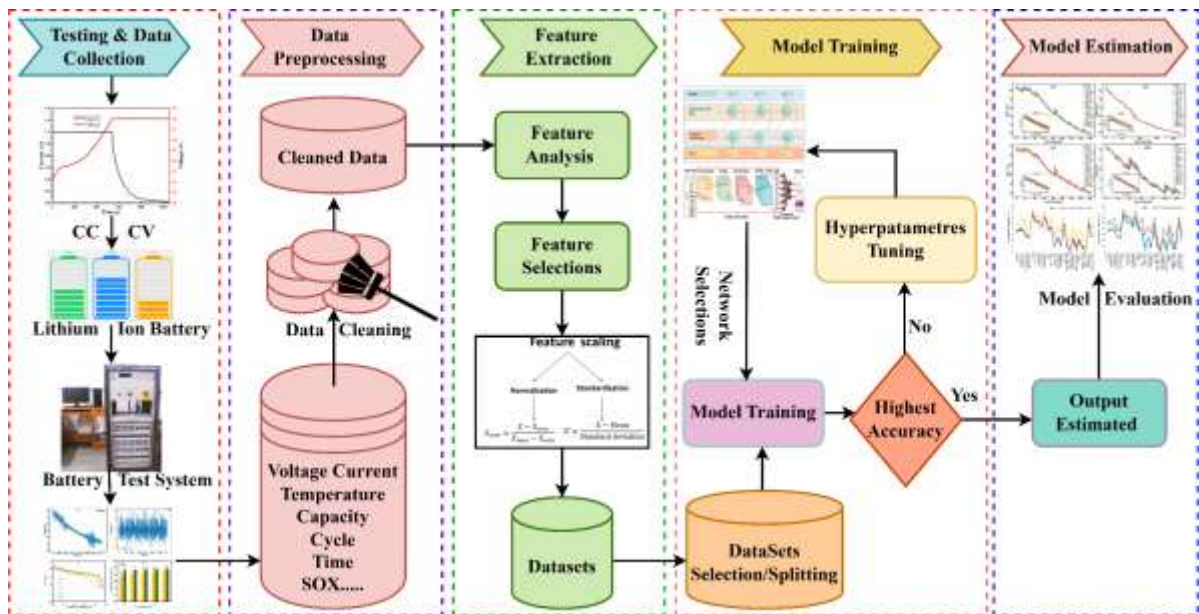


Figure 6.1 The ML-based framework for SOH estimation of LIBs

6.3.1 Experimental Setup and Dataset Description

A battery test bench equipped with a Chroma 17020 tester and Chroma 17020 software has been used to perform ageing tests, as shown in Figure 6.2. The setup supports CC and CC-CV cycling modes, with currents up to ± 2600 A and an output power of 60 kW, offering measurement precision of ± 0.02 – 0.05% . Four 18650 cylindrical LIBs with different cathode materials (LCO, NCA, LFP, NCA) and graphite anodes, labelled D1–D4, were tested under CCCV conditions at room temperature, within the voltage ranges of 2.7–4.2 V and capacity of 2.6 Ah. Each battery underwent ageing cycles at a 1C rate, and the results are shown in Figure 6.2(c’).

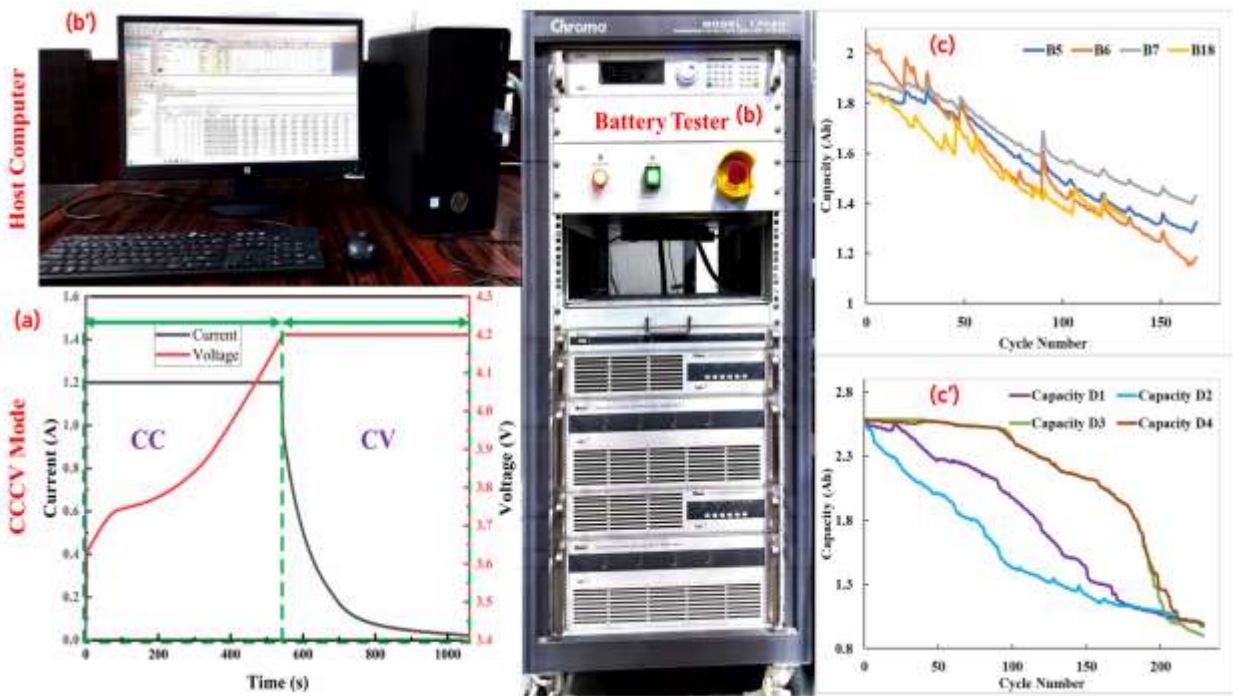


Figure 6.2 The degradation trajectory of batteries; (a) CCCV process approach (b-b’), battery test bench setup, (c-c’) NASA battery and experimental battery dataset

For validation, a NASA PCoE dataset comprising four 18650 NCA cells (B0005–B0018) is tabulated in Table 6.1 was also used, during under CC-CV charging and CC discharging. All models were implemented in TensorFlow (Python 6.4.12) on a Windows 11 Pro system (Intel i7–

12700, 12-core, UHD 770 GPU). Adam optimiser and grid search were used for optimisation, and leave-one-out cross-validation ensured generalisation. Moreover, the model accuracy was evaluated using MAE, MSE, RMSE, R^2 , and MaxError as discussed in chapters 4 and 5. Hence, MAE measures the average deviation, RMSE captures error fluctuations, R^2 indicates goodness of fit (values close to 1 show high reliability), and MaxError identifies the largest deviation between predicted and actual SOH values.

Table 6. 1 Lithium-ion batteries technical specifications.

Battery	LCO	NCA	LFP	NMC
Positive Material	LiCoO ₂	LiNi _{0.8} Co _{0.15} Al _{0.05} O ₂	LiFePO ₄	LiNi _{0.5} Co _{0.3} Mn _{0.2} O ₂
Negative Material	Graphite	Graphite	Graphite	Graphite
Nominal Capacity (Ah)	2.6	2.6	2.6	2.6
Voltage Ranges (V)	4.2	2.5-4.2	2-3.65	4.6
Charge/ Discharge Conditions	CCCV/CC	CCCV/CC	CCCV/CC	CCCV/CC
Max Discharge Current (A, 25°C)	20	6	20	20
Acceptable Temperature (°C)	0-50	0-45	0-60	0-50

6.3.2 Results and Discussion

The performance of the proposed models, including their precision, robustness, and computational efficiency, was validated and tested using dataset generalizability. In this section, the performance of all ML models was validated, discussed, and explained. To verify the generalisation, SOH estimation was performed on four battery chemistries, denoted D1 to D4, which are illustrated in Figure 6.3(a-d). The results demonstrate reliable predictive performance across different datasets, as evidenced by minimum and maximum estimation errors.

6.3.3 Validation Across Different Battery Chemistries

The proposed ML models were validated by including different cathode materials: LCO (D1), NCA (D2), LFP (D3), and NCA (D4), as shown in Figure 6.3 (a–d). The estimation results confirmed the applicability of the proposed ML models to the D1-type battery dataset, as illustrated in Figure 6.3(a), and estimation errors are shown in Figure 6.4(a–d).

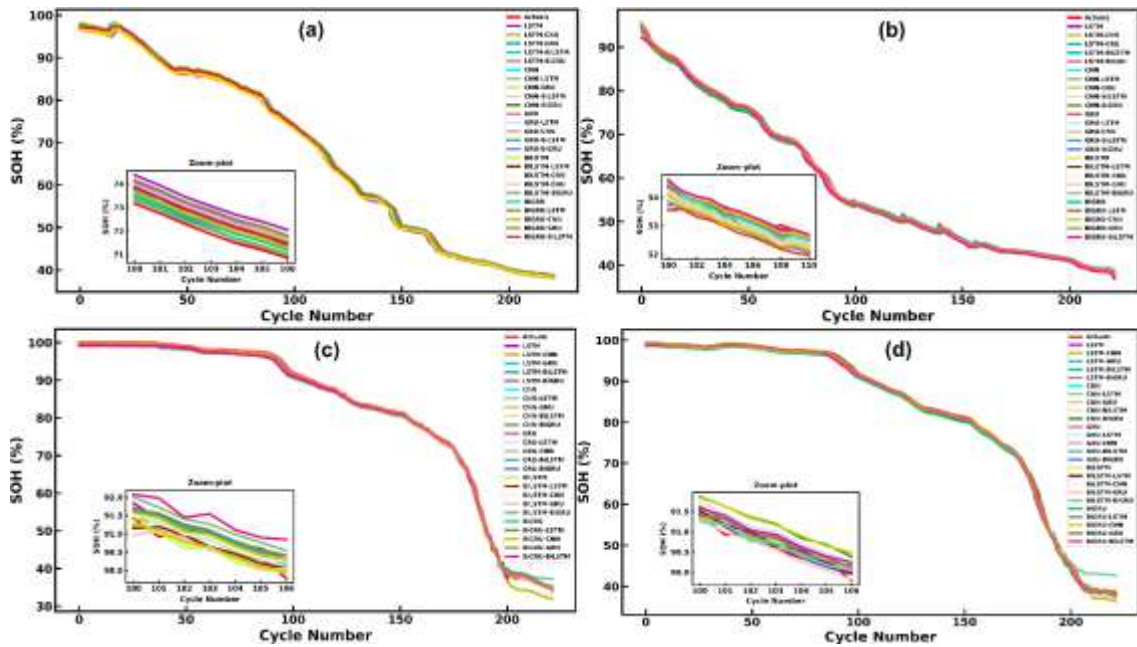


Figure 6.3 SOH estimation results against the measurements of D1-D4 batteries (a-d).

Among them, the BiGRU-LSTM achieved the best performance, with the lowest value of MAE of 0.0028, MSE of 0.0017, and RMSE of 0.0041, as shown in Figure 6.4(a). In contrast, CNN-GRU exhibited a higher error, with an MAE of 0.0088, an MSE of 0.0094, and an RMSE of 0.0099, but in 8 ms for computation, compared to 16 ms for BiGRU-LSTM, as shown in Figure 6.4(a & c), indicating greater computational efficiency. The maximum and minimum errors were 3.4775 and 2.2436 for CNN-GRU and BiGRU-LSTM, respectively, in Figure 6.4(f). The R^2 values of 0.9995 for the CNN-GRU model and 0.9978 for BiGRU-LSTM in Figure 6.4(g) verify strong model fitness, confirming the robustness and reliability of the proposed ML frameworks.

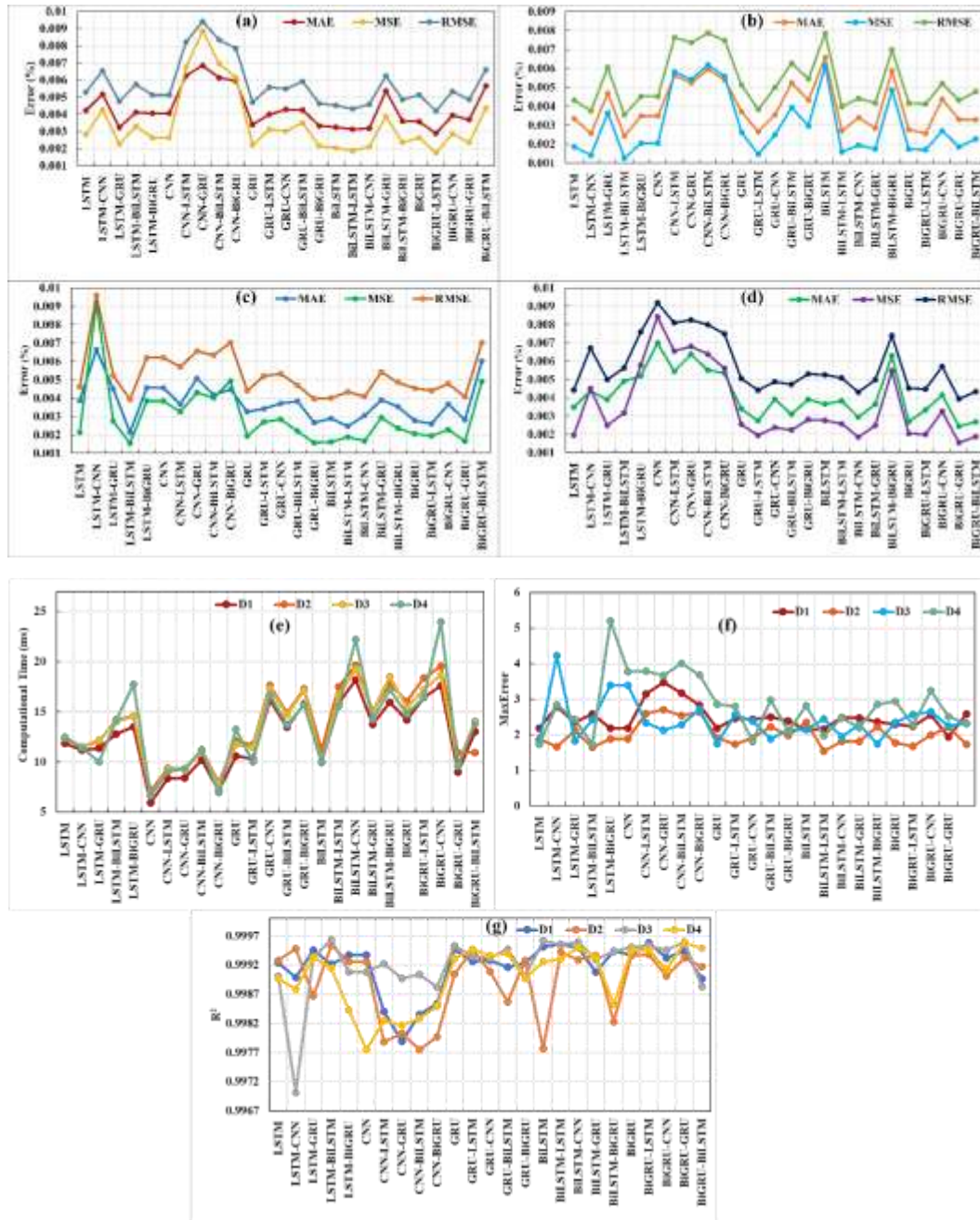


Figure 6.4 SOH estimation errors (a-d), computational time (e), Maxerror (f), R^2 (g) across the D1-D4 batteries.

Figure 6.3(b) illustrates the D2-type SOH estimation results for different ML models. Figure 6.4(b) demonstrates that LSTM-BiLSTM achieves the lowest estimation error, MAE of 0.0024, MSE of 0.0012, and RMSE of 0.0035 among all ML models. However, the CNN-BiLSTM achieved the

lowest MAE, MSE, and RMSE among all ML modes: 0.0059, 0.0061, and 0.0078, respectively. The computational efficiency of these two models was recorded at 14.201 ms and 11.1092 ms, respectively, as seen in Figure 6.4(e). These results verify that the LSTM-BiLSTM were not computationally efficient compared to the CNN-BiLSTM. As demonstrated in Figure 6.4(f), the LSTM-BiLSTM had lowest maximum error of 1.6500, outperforming the CNN-BiLSTM 2.5344. This shows the LSTM-BiLSTM has higher SOH estimation accuracy. The statistical fit validates both models R² values of 0.9995 and 0.9977, as shown in Figure 6.4 (g). It shows that LSTM-BiLSTM fits the dataset better than CNN-BiLSTM.

The SOH estimation results for the D3 batteries dataset, as shown in Figure 6.3(c), demonstrate that the LSTM-BiLSTM achieved the minimum estimation errors, with an MAE of 0.0021, MSE of 0.0015, and RMSE of 0.0039, superior to all of the other models, as illustrated in Figure 6.4(c). In terms of computational efficiency, the LSTM-CNN outperforms the LSTM-BiLSTM, with a computational time of 11.5179 ms compared to 13.9796 ms, as seen in Figure 6.4(e). Despite this, the LSTM-BiLSTM model was superior to the LSTM-CNN, with a larger maximum error of 4.2206. The LSTM-BiLSTM and LSTM-CNN performed well in SOH estimation as shown in Figure 6.4(f). However, Figure 6.4(g) demonstrates that the LSTM-BiLSTM had a slightly improved fit, with an R² value of 0.9996 compared to the LSTM-CNN R² of 0.9970. The most suitable SOH estimation model should consider the requirements specific to an application, such as reducing maximum errors. Although the LSTM-CNN is faster, the LSTM-BiLSTM has a lower maximum error and provides more accurate estimates.

Figure 6.c(d) shows the SOH estimation results for all models tested on the D4 dataset. The BiGRU-GRU had the highest performance, with the lowest error metrics, MAE of 0.0024, MSE of 0.0015, and RMSE of 0.0039, validating its higher accuracy, as shown in Figure 6.4(d). In

contrast, the CNN model had the highest estimated errors, with an MAE of 0.0069, MSE of 0.0084, and RMSE of 0.0091, indicating significantly worse performance than the other models. However, the CNN model outperformed the BiGRU-GRU model in terms of computational efficiency, processing data in 6.6656 ms compared to 9.5734 ms, as demonstrated in Figure 6.4(e). The BiGRU-GRU maximum error was 2.5113, whereas the CNN achieved 3.0237, resulting in a slightly larger maximum error and lower SOH estimation accuracy, as shown in Figure 6.4(f). The BiGRU-GRU model was highly reliable, with an R^2 of 0.9995, and the CNN model achieved an R^2 of 0.9977, as shown in Figure 6.4(g). These findings highlight the importance of selecting an appropriate ML model for SOH estimation in the D4 dataset.

6.3.4 NASA Dataset Generalization Validation

This work tested proposed ML models for generalisation validation using publicly available NASA PCoE battery datasets [125]. The SOH estimation results of ML models using datasets B5-B7 and B18 are shown in Figure 6.5(B5-B7 and B18) and estimation error in Figure 6.6. Upon examining the B5 dataset, the different ML models achieved different estimates, as shown in Figure 6.5(B5). The minimum estimation errors, MAE, MSE, and RMSE, are achieved by GRU-BiGRU, 0.0042, 0.0047, and 0.0068, respectively, as shown in Figure 6.6 (B5). When compared to all other models, the BiLSTM-CNN model obtained the highest estimate errors, MAE, MSE, and RMSE of 0.0074, 0.0095, and 0.0099, respectively, as seen in Figure 6.6(B5). To validate computational efficiency, the GRU-BiGRU model ran faster than the BiLSTM-CNN model, taking 26.7317 ms versus 29.0554 ms, as demonstrated in Figure 6.6(a). The maximum error indicates the largest difference between the actual and predicted SOH values by the ML models. The GRU-BiGRU model achieved the maximum error of 4.5617, whereas the BiLSTM-CNN model achieved 5.2380, as shown in Figure 6.6(b).

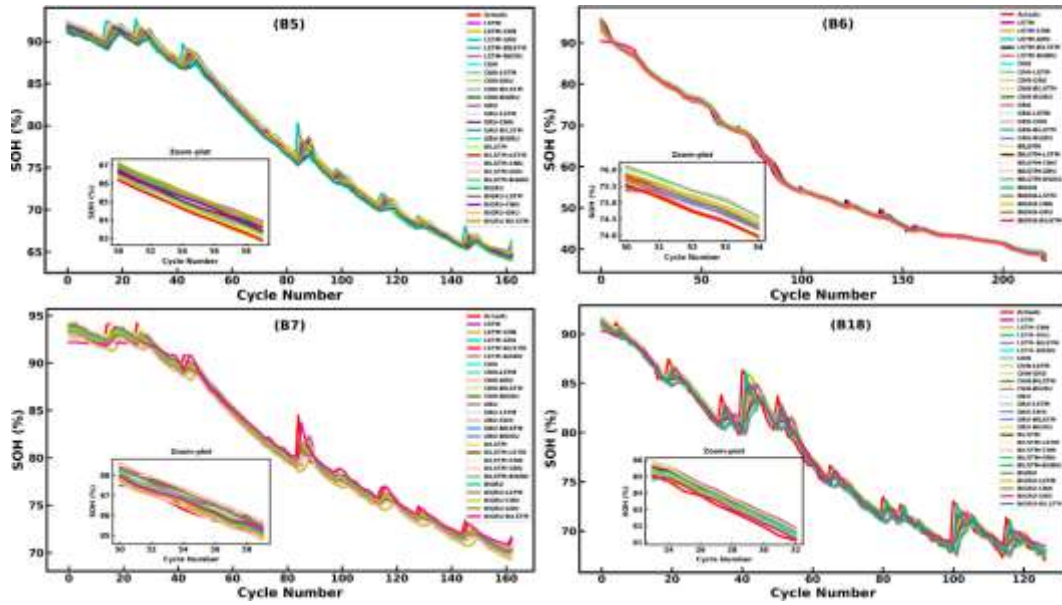


Figure 6.5 NASA batteries SOH estimation results of B5, B6, B7, and B18

The results demonstrate that the GRU-BiGRU model is more accurate and efficient than the BiLSTM-CNN model in terms of maximum error. The R^2 values of 0.9921 and 0.9871, shown in Figure 6.6(c), further confirm the superior fitting performance of the GRU-BiGRU model on the B5 dataset.

For the B6 dataset, the LSTM-BiLSTM model exhibited the best accuracy, with MAE of 0.0023, MSE of 0.0035, and RMSE of 0.0012, as shown in Figure 6.6(B6), outperforming the CNN-BiLSTM, which had higher errors, such as MAE of 0.0065, MSE of 0.0059, and RMSE of 0.0077, respectively. Although CNN-BiLSTM achieved a faster computation time around 11.11 ms than LSTM-BiLSTM around 14.20 ms are shown in Figure 6.6(a), the latter showed higher estimation accuracy. The maximum error of CNN-BiLSTM of 5.2380 was also greater than that of LSTM-BiLSTM of 4.5610 are shown in Figure 6.6(b). The R^2 values of 0.9997 for LSTM-BiLSTM and 0.9953 for CNN-BiLSTM are shown in Figure 6.6(c) confirm a better model fit.

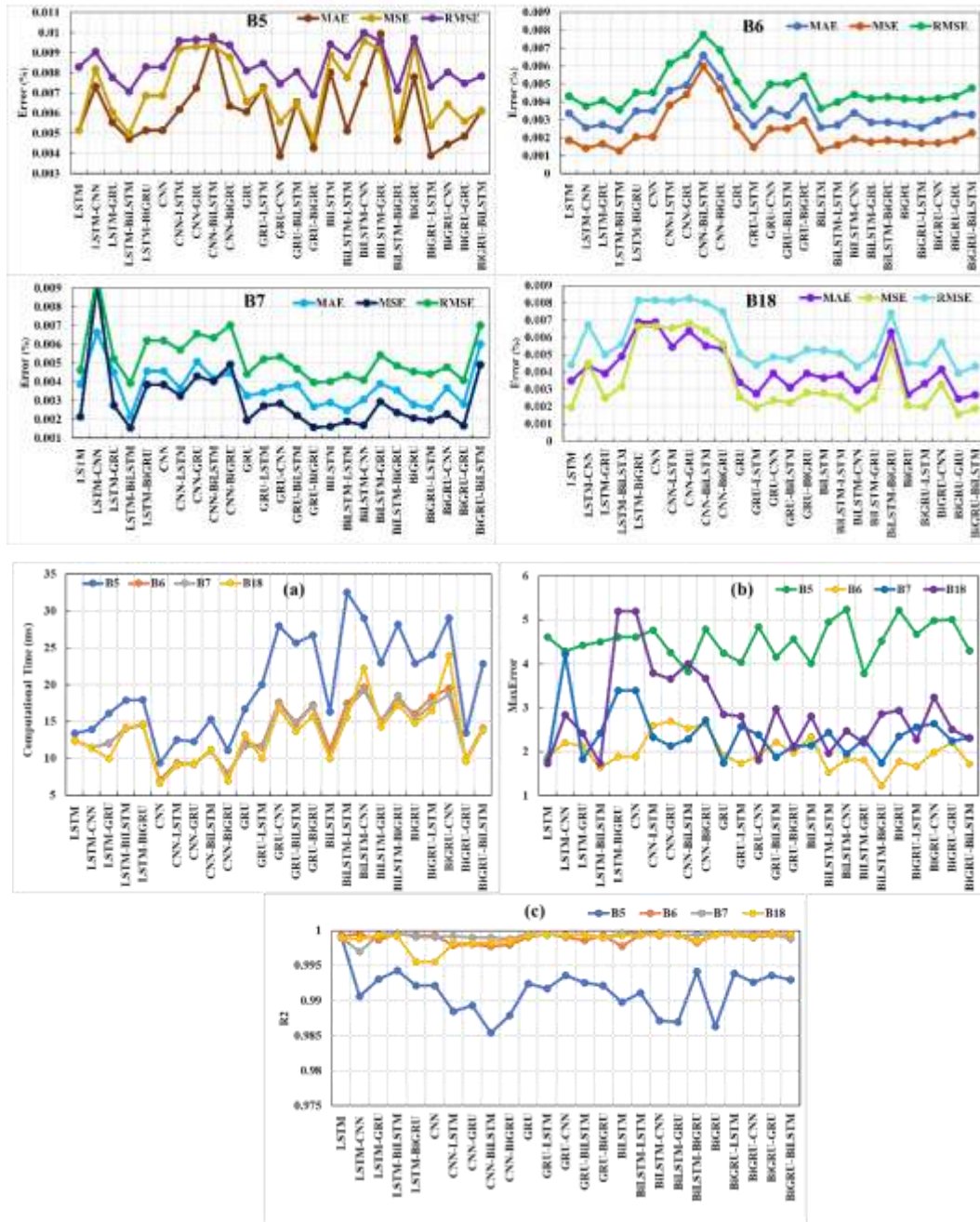


Figure 6.6 SOH estimation errors (B5, B6, B7, and B18), computational time (e), Maxerror (f),

R^2 (g) across the NASA batteries B5, B6, B7, and B18

In the B7 dataset, the LSTM-BiLSTM model outperformed the LSTM-CNN model, achieving lower errors, as shown in Figure 6.5(B7). The MAE of 0.0021, MSE of 0.0015, and RMSE of 0.0039, compared to 0.0066, 0.0092, and 0.0096, respectively, as shown in Figure 6.6(B7). Despite

a slightly longer computation time of 13.98 ms vs. 11.52 ms, as shown in Figure 6.6(a). Overall, LSTM-BiLSTM delivers higher accuracy, while CNN-based models exhibit faster computational efficiency, highlighting a trade-off between precision and speed in SOH estimation. The LSTM-BiLSTM model is found to be more reliable and accurate for SOH estimation, achieving a maximum error of 2.4159, significantly lower than the LSTM-CNN model's 4.2206 are shown in Figure 6.6(b). Although the LSTM-CNN achieved a slightly higher R^2 of 0.9970 compared to LSTM-BiLSTM of 0.9966, as shown in Figure 6.6(c), it demonstrated better generalisation and consistency. Hence, the LSTM-BiLSTM model is recommended for accurate and reliable SOH prediction on the B7 dataset.

For the B18 dataset, the BiGRU-GRU model exhibited superior SOH estimation accuracy and reliability compared to the LSTM-BiGRU model, as shown in Figure 6.5(B18). It achieved lower errors, MAE of 0.0024, MSE of 0.0015, RMSE of 0.0039, than LSTM-BiGRU MAE of 0.0068, MSE of 0.0049, RMSE of 0.0070, respectively, as shown in Figure 6.6(B18). Although LSTM-BiLSTM had a faster computation time, 9.57 ms, than BiGRU-GRU, 14.75 ms, as shown in Figure 6.6(a), it demonstrated a lower maximum error, 2.5113 vs. 5.201, as shown in Figure 6.6(b). Moreover, BiGRU-GRU achieved a higher R^2 of 0.9995 compared to LSTM-BiGRU, 0.9955, as shown in Figure 6.6(c). Overall, the BiGRU-GRU model outperforms others in terms of accuracy and robustness for SOH estimation on the B18 dataset, while maintaining strong computational efficiency.

6.3.5 Performance Validation on Computational Efficiency

One significant challenge of using ML is the high computational efficiency involved. However, computation efficiency needs to be more well-defined and varies depending on the circumstances. In many cases, the model's computational time, i.e., the time it takes to execute, is used as a metric.

This thesis examines computational efficiency in terms of the computational time required by the models, as shown in Figure 6.7(a-b). In this section, performances have been validated based on the computational time required for the model to train a particular battery dataset, as shown in Figures 6.4(e) and 6.6(a). The computational efficiency (CE) is calculated by Equation 6.1. In this case, the maximum computational time (HCT) achieved by a model from all proposed models is considered to be equal to the reference computational time (RCT).

$$\text{Computational Efficiency (\%)} = \frac{\text{RCT} - \text{ACT}}{\text{RCT}} \times 100 \quad (6.1)$$

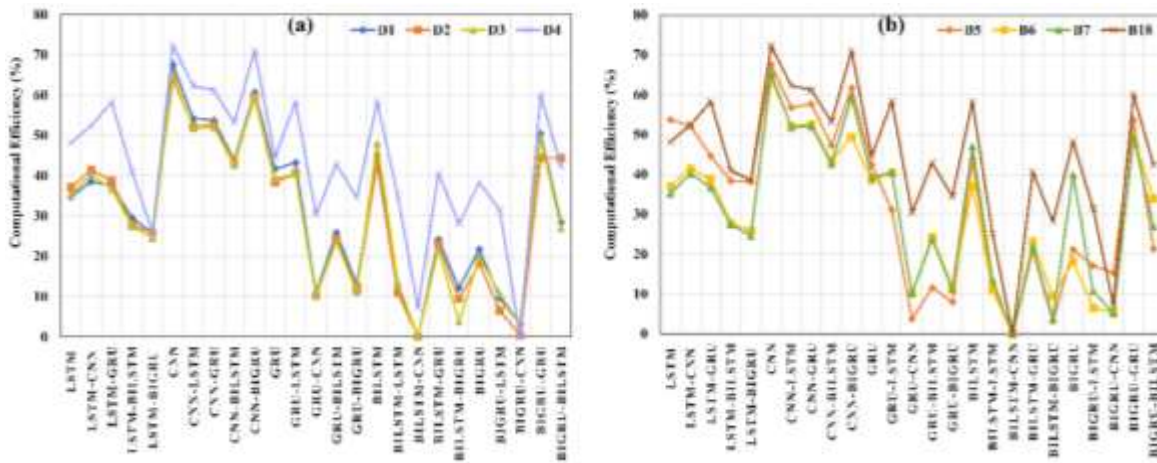


Figure 6.7 Computational efficiency (a) D1, D2, D3, and D4, (b) B5, B6, B7, and B18

Whether all the remaining model computational time is considered actual computational time (ACT). For example, in the D1 battery dataset, the HCT obtained by the BiLSTM-CNN model is 18.1645 ms. However, the LSTM model achieved a CT of 11.84688 ms. According to Equation 6.1, the LSTM model is 32.5% more computationally efficient than the BiLSTM-CNN for the D1 battery dataset. In summary, quantitative results across multiple battery chemistries demonstrated that the proposed ML frameworks deliver accurate, reliable, and generalizable SOH estimation. The hybrid recurrent architecture consistently achieved lower estimation errors and the highest model fitness. However, CNN gives excellent computational efficiency. These results confirm the

proposed approach's ability to balance prediction accuracy and computational speed, making it suitable for real-time condition-aware battery BMS applications.

6.4 IMPACT OF TEMPERATURE VARIATIONS

Temperature is one of the most critical environmental factors influencing LIBs performance, degradation, and state estimation accuracy. Deviations from the optimal thermal window (–20 to 40 °C) lead to kinetic limitations, impedance fluctuations, and accelerated degradation. This section examines the electrochemical impact of temperature variation, AI-based state estimation under different thermal conditions, and experimental validation using drive cycles.

6.4.1 AI-based SOC Estimation Under Different Thermal Profiles

This research aims to understand the impact of temperature variation on SOC and minimise model training time while achieving high accuracy. The LSTM, GRU, and CNN architectures are proposed to capture the nonlinear dynamics of batteries under different thermal profiles. A “multi-time input” approach improves input processing, enhancing stability and accuracy without requiring OCV–SOC lookup tables. The models exhibit low estimation errors while maintaining high computational efficiency.

6.4.2 Proposed Work

The proposed methodology for SOC estimation under different temperature conditions consists of sequential steps, as shown in Figure 6.8. Initially, battery-tested data, including current, voltage, capacity, and temperature measurements, are collected. These data are then preprocessed by removing outliers, smoothing signals, aligning measurements, and applying Min-Max normalization. Relevant features such as maximum and minimum values of voltage, current and temperature are extracted and divided into training datasets.



Figure 6.8 The flow chart of the proposed work

Subsequently, the proposed CNN, GRU, and LSTM models are trained with optimised hyperparameters. Finally, SOC estimation performances are evaluated by the statistical metrics such as MAE, MSE, and RMSE. The experimental simulation platform and working principles of CNN, GRU, and LSTM architectures were described in Chapters 4 and 5.

6.4.2.1 Data Processing

This research was performed using an open-source LIBs dataset: "Turnigy Graphene 5000mAh, 3S LiPo cell [126]. The battery characteristics are illustrated in Table 6.2. The dataset includes measurements collected under six different temperatures i.e., -20, -10, 0, 10, 25, and 40 °C with different C-rates i.e. 0.05C, 0.5C, 1, and 2C on four driving cycles, namely UDDS, HWFET, LA92, and US06 of LIBs. However, the LA92 was used only to perform SOC estimation. To improve data reliability, measured data were normalized to the ranges [0, 1] using the Min-Max scaler, as shown in equation 6.2.

$$x_{norm} = \frac{x - x_{min}}{x_{max} - x_{min}} \quad (6.2)$$

Where, x_{max} and x_{min} are the maximum and minimum data values, x represents the original data, and x_{norm} represents the normalised data. Additionally, a "multi-time input" structure was implemented to capture temporal dependencies by incorporating sequential data within a defined

time window (k), as shown in Figure 6.9. SOC_k applies to all data. This process enhanced SOC estimation and model robustness [127].

Table 6. 2 The technical specifications of the LIBs battery

Battery	Type
Model	Graphene 65C
Format	Pouch
Chemistry	LiPO or NCM
Rated Capacity	5.0 Ah
Normalized Resistance	14 m Ω
Specific Power and Energy	7.3 & 134k W/kg
Energy Density	329 Wh/l

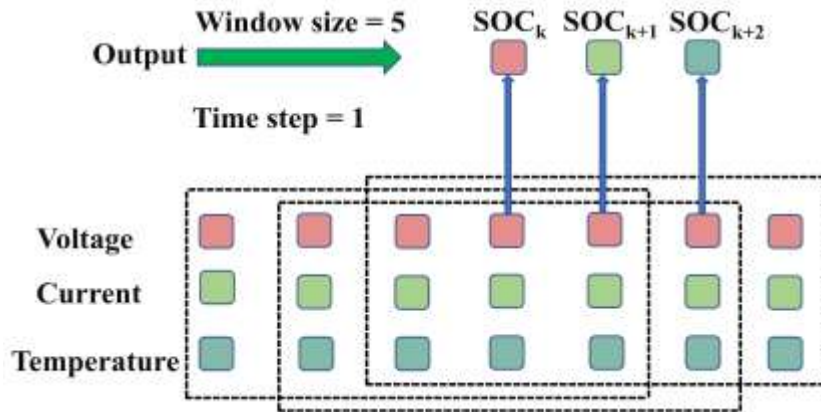


Figure 6.9 The "Multi-time input" structure of the network

6.4.2.1 Model Training and Hyperparameter Tuning

The proposed models were implemented using the Python platform with Keras and TensorFlow library. The Adam optimizer with the learning rate 0.01 was used for network training, and all models were trained for 50 epochs. The loss function is the root mean square error and the mean squared error. Hyperparameter tuning performed by adjusting key parameters such as learning rate, hidden units to achieve estimation accuracy and avoiding overfitting and unnecessary computation time [128], [129]. The evaluation matrices are used to verify the accuracy of each model's estimation, as discussed in the Chapter 4 and 5.

6.4.2.2 Analysis and Discussion on Impact of Temperatures on LIBs Performance

Battery performances are strongly dependent on operating temperature, which must be maintained within an optimal range to ensure safety, efficiency, and long cycle life[130]. The battery temperature high and low both increase degradation process, reduces energy efficiency and shortens the cycle life. However, high temperatures lead to TR event [131]. The variation in the working environment poses significant impact on the estimation of SOC [132]. The effect of dynamic load on SOC estimation, particularly under time-varying temperature conditions, has been addressed. Therefore, temperature-aware modelling and AI-based state estimation techniques are essential to ensure accurate SOC estimation under varying and dynamic drive profile conditions.

The proposed models were validated using LA92 test drive cycle data at -10, 0, 10, 25, and 40 °C to investigate the effect of temperature. Figure 6.10(a-e) shows estimated SOC performances using LSTM at different temperatures. It was found that the LSTM model performed more efficiently at 25, 40, and 10°C, while it was very poor at -10 and 0°C, with maximum errors of 0.4710 and 0.3322, respectively, as shown in Figure 6.11(a-e). The LSTM accuracy outcomes are tabulated in Table 6.3. High accuracy was obtained in both ambient and high temperatures. The fluctuations were observed at 0 °C, as clearly seen in Figure 6.10(b, zoomed inset plot). It might have occurred due to internal battery chemistry, which is very difficult to attribute at low temperatures. It was found that the model worked better with minimal errors, 0.0986 at ambient temperature and about 0.01037 at high temperature, as shown in Figure 6.11(b).

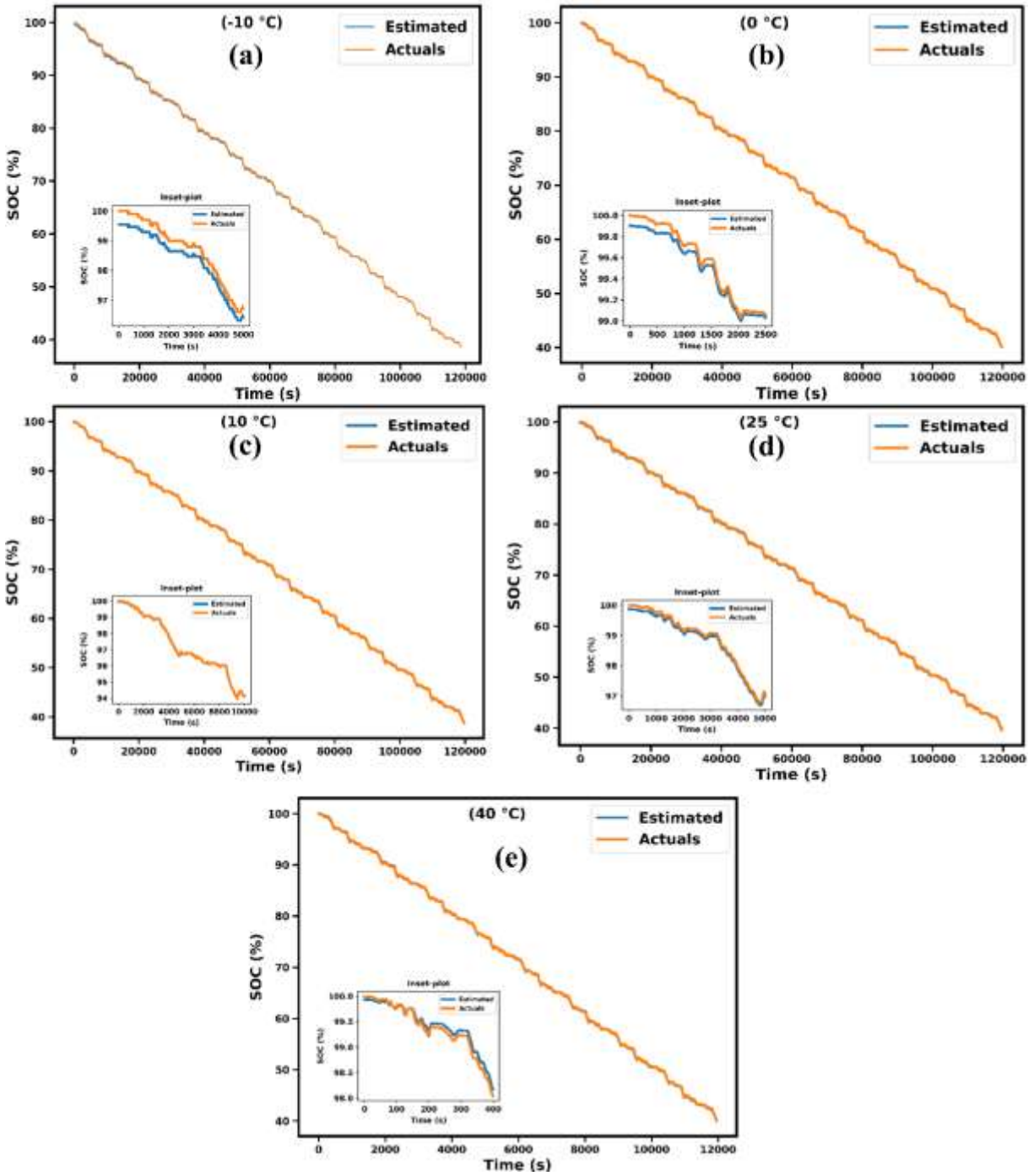


Figure 6.10 Actual and estimated performances and errors with LSTM under different temperatures.

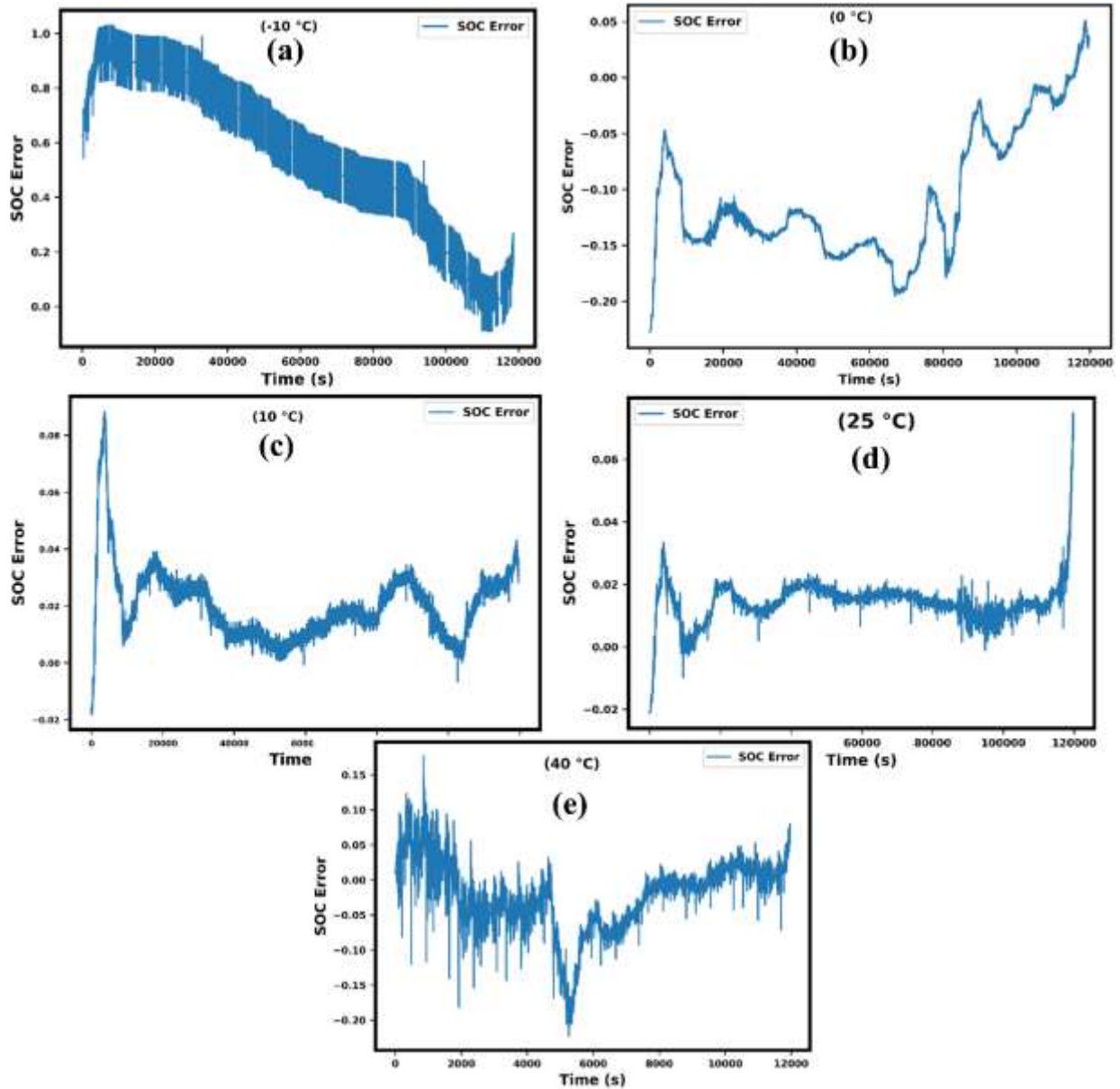


Figure 6.11 Actual and estimated performances and errors with LSTM under different temperatures.

Therefore, based on its maximum error, LSTM was found to be ineffective at low temperatures with this battery data because it is difficult to determine its internal chemistry under these conditions.

Table 6. 3 LSTM estimation accuracy results of the LA92 test driving cycle at different temperatures.

Temperature (°C)	MAE	MSE	RMSE	R ²	MaxError	Time (s)
-10	0.2202	0.0535	0.2314	0.9998	0.4710	425
0	0.1007	0.0169	0.1302	0.9999	0.3322	388
10	0.0279	0.0013	0.0368	0.9999	0.1063	393
25	0.0158	0.0003	0.0173	0.9999	0.0986	456
40	0.0174	0.0004	0.0220	0.9998	0.1037	60

The GRU model trains faster with fewer parameters, making it suitable for system integration. However, at 10 °C, it exhibits notable fluctuations and significant errors between estimated and actual SOC values, as shown in Figure 6.12(a-e) and 6.13(a-e) and Table 6.4. This reduced accuracy is due to the complex temperature-dependent dynamics of the battery, which hinder the extraction of features. The GRU performs best at 0 °C, achieving an RMSE of 0.2569 and a maximum error of 0.4982, while larger errors occur at -10 °C and 40 °C. Overall, GRU accuracy is highly temperature-sensitive, limiting its reliability across varying conditions.

Table 6. 4 GRU Estimation results of the LA92 test driving cycle at different temperatures

Temperature (°C)	MAE	MSE	RMSE	R ²	MaxError	Time (s)
-10	0.2960	0.0934	0.3056	0.9997	0.5465	366
0	0.2328	0.0660	0.2569	0.9997	0.4982	392
10	1.0367	1.3256	1.1513	0.9956	2.0387	306
25	0.2615	0.0901	0.3003	0.9996	0.6111	351
40	0.2892	0.1165	0.3413	0.9995	0.7473	56

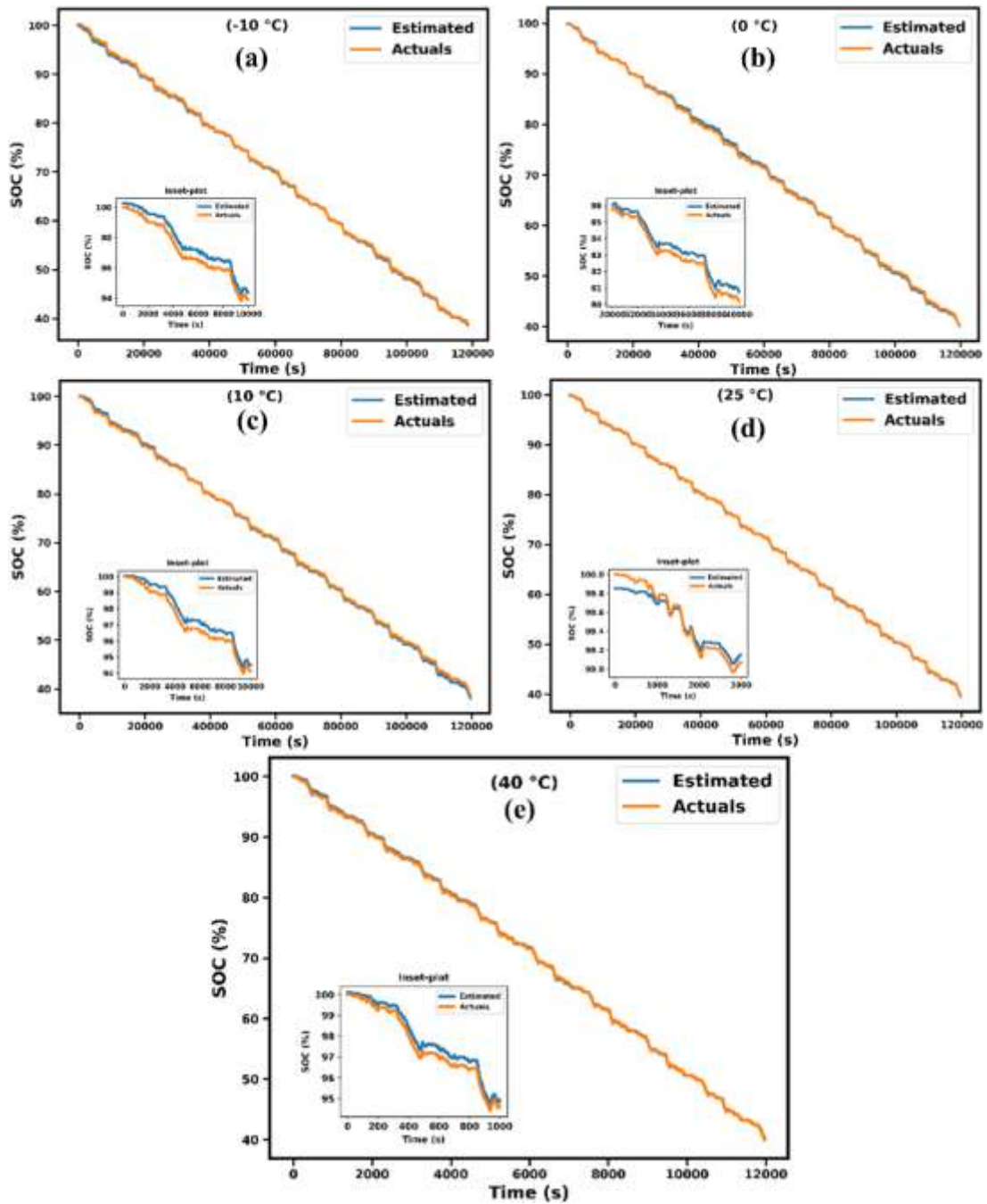


Figure 6.12 Actual and estimated performances and errors with GRU under different temperatures.

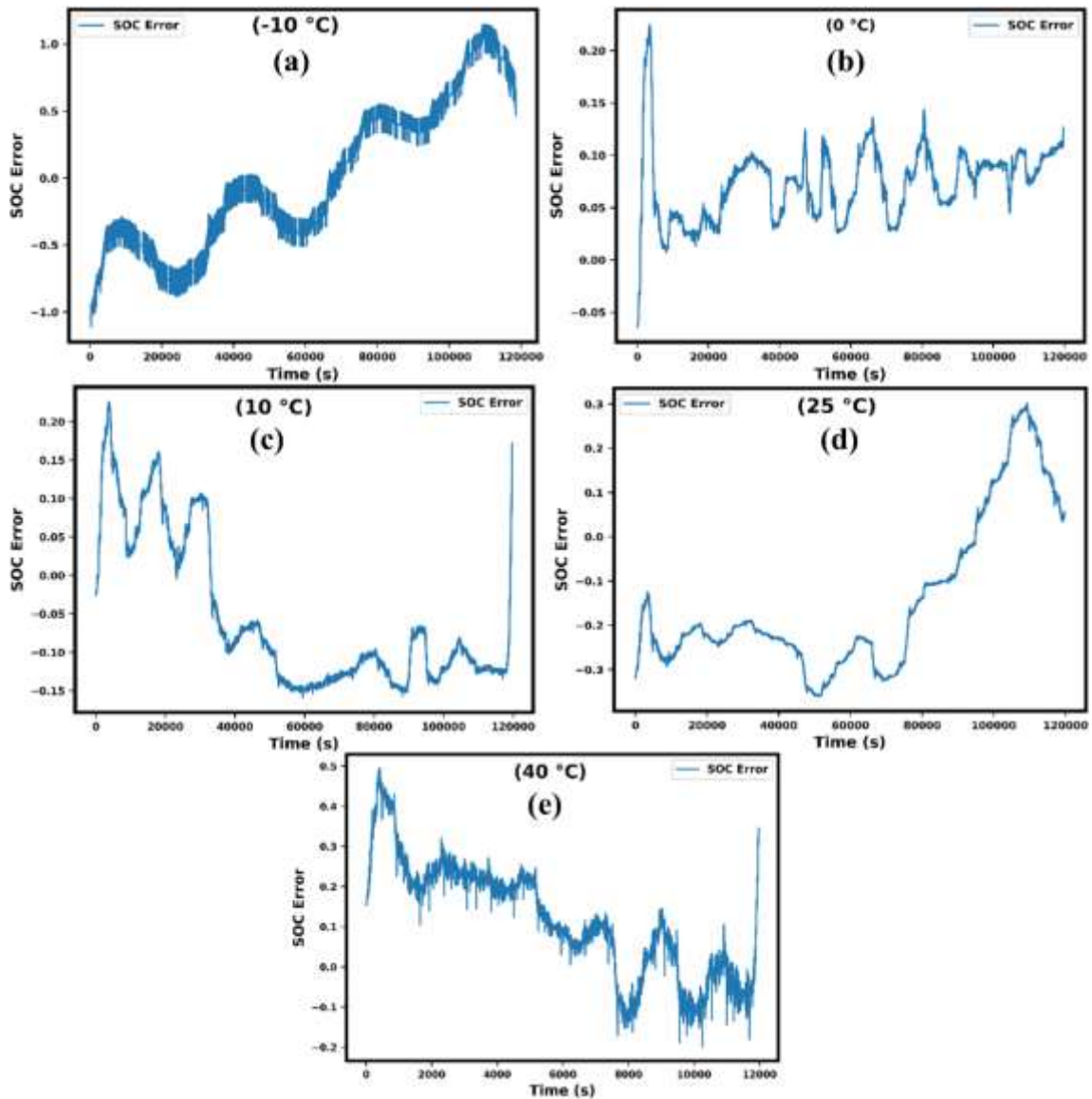


Figure 6.13 Actual and estimated performances and errors with GRU under different temperatures.

The CNN model's SOC estimation results with errors are shown in Figure 6.14(a-e) and Figure 6.15(a-e). The estimated performance under various temperatures is generally satisfactory compared to that of LSTM and GRU. The SOC estimation performances, including MAE, MSE, RMSE, R^2 , and Maximum error, are tabulated in Table 6.5. The superior performance was gained by CNN at 0 °C and 10 °C, while the performance was weakest at 25 °C and 40 °C. The SOC estimate performance at -10°C is satisfactory compared to the ambient and high temperatures. It

is significantly more challenging for the suggested network to acquire relevant characteristics, as lithium-ion batteries exhibit poor performance and more complex internal dynamics at low temperatures. In brief, the proposed network may easily be expanded to consider the impact of ambient temperature on battery SOC estimates by simply adding temperature as a network input. Overall, the suggested approach may provide a reasonable SOC estimate for various temperatures. To validate the effectiveness of the proposed SOC estimation models, LSTM, GRU, and CNN. CNN shows the best results and the worst performance achieved by GRU. Whereas GRU and LSTM require more training time due to their complex structure and the presence of many cell states at each hidden neuron, CNN requires less time to train the model. This research demonstrates that the proposed network completely satisfies the requirements of practical operation and exhibits excellent accuracy and resilience under various working conditions.

Table 6. 5 CNN Estimation results of the LA92 test driving cycle at different temperatures

Temperature (°C)	MAE	MSE	RMSE	R ²	Max Error	Time (s)
-10	0.0033	0.0002	0.0148	0.9999	0.1007	141
0	0.0030	1.85e-5	0.0043	0.9999	0.0215	243
10	0.0035	2.29e-5	0.0047	0.9999	0.0286	218
25	0.0247	0.0006	0.0250	0.9999	0.0608	248
40	0.0310	0.0016	0.0403	0.9999	0.2069	33

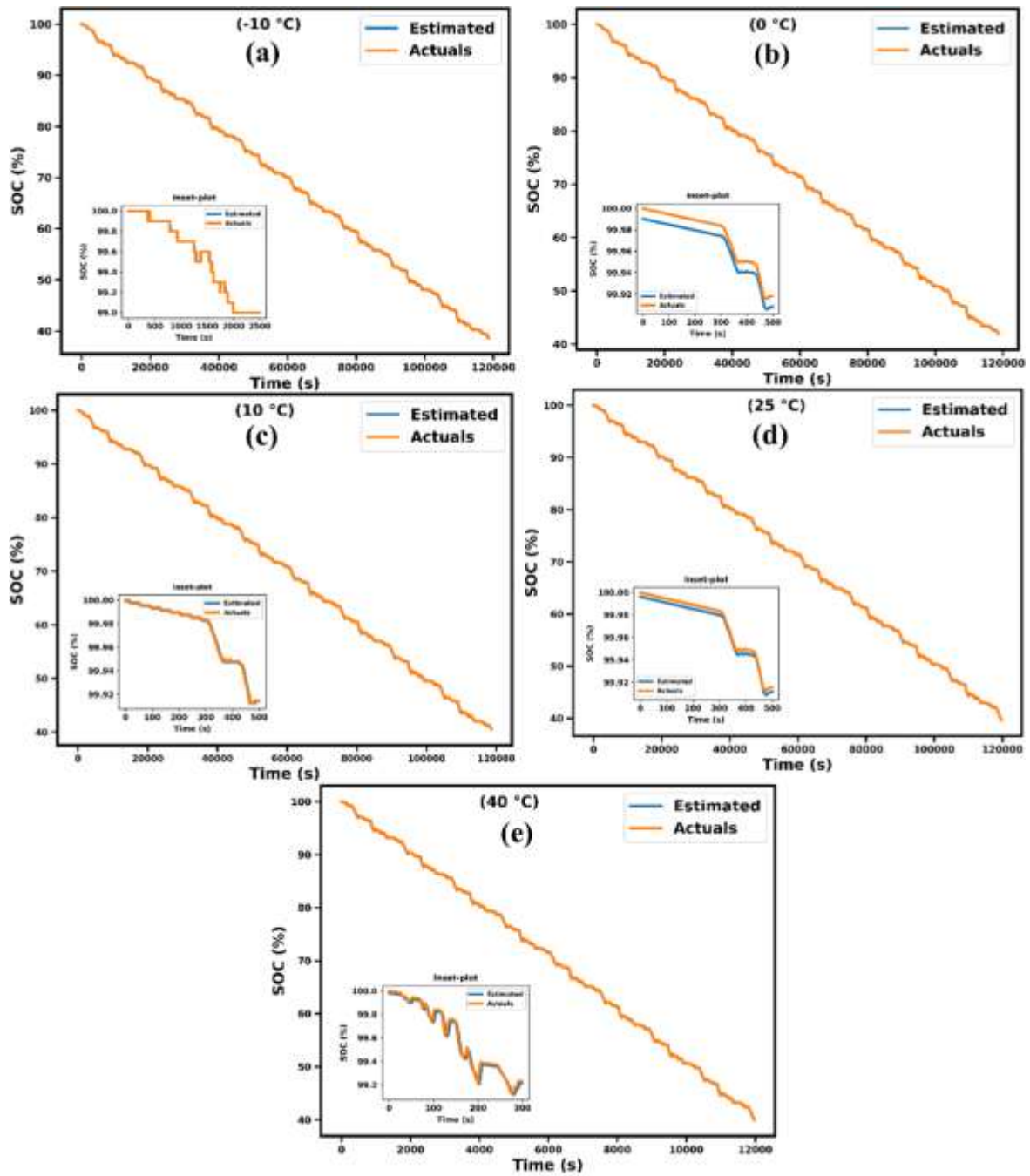


Figure 6.14 Actual and estimated performances and errors with CNN under different temperatures.

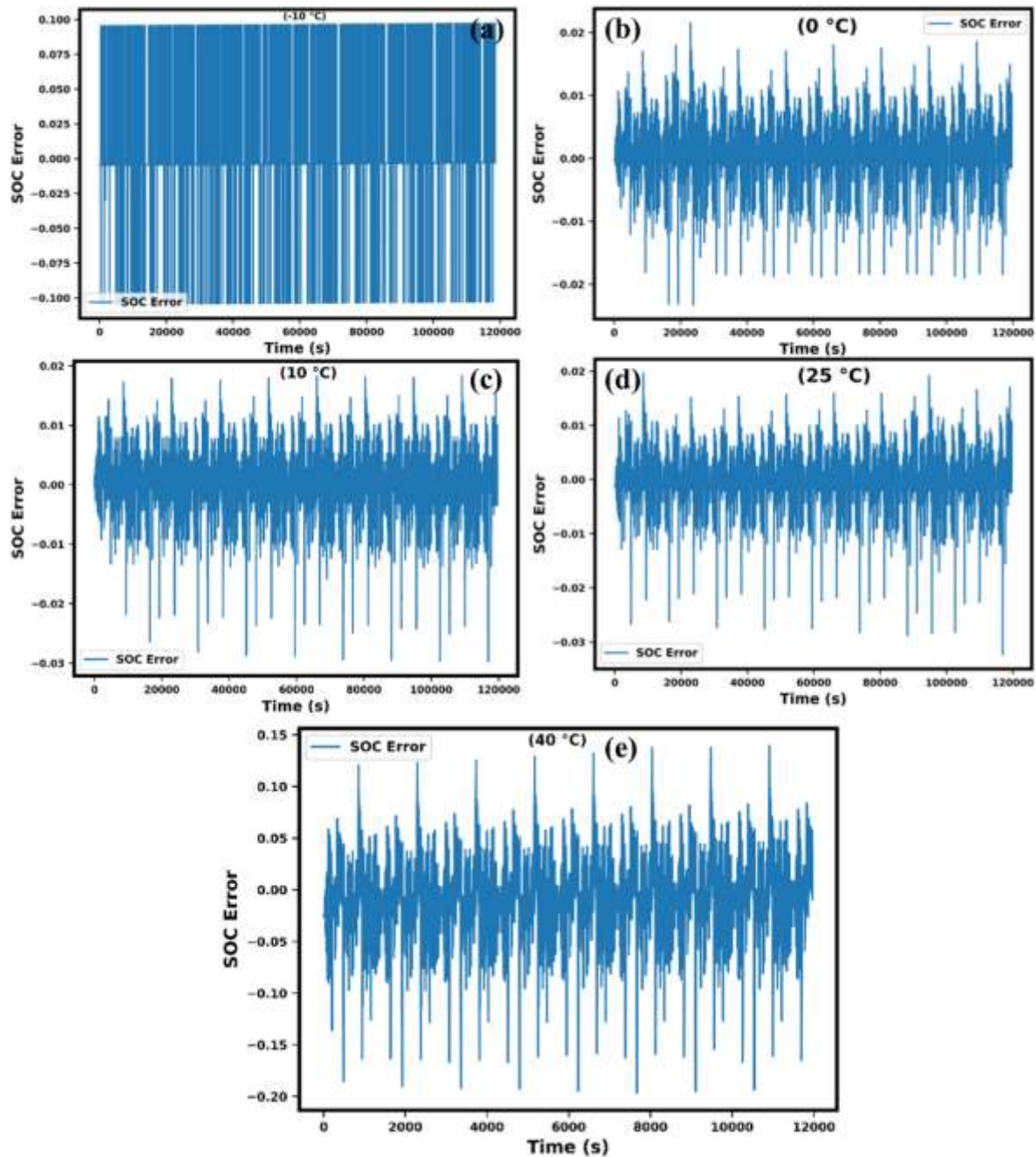


Figure 6.15 Actual and estimated performances and errors with CNN under different temperatures.

A comparison of different reports on AI model performance for SOC estimation is presented in Table 6.7. In this comparison, the present work is more accurate in estimating SOC, demonstrating that the proposed models could be promising for more accurate SOC estimation. The

computational efficiency (CE) of the GRU and CNN methods is calculated using Equation 6.14, with the LSTM's actual computational time serving as a reference, as shown in Table 6.6. The highest CE reported by CNN is 66.82% at -10 °C, while the lowest CE reported by GRU is 1.03% at 0 °C.

$$\text{Computational Efficiency (\%)} = \frac{\text{Reference computational time} - \text{Actual computational time}}{\text{Reference computational time}} \times 100 \quad (6.14)$$

Table 6. 6 CNN Estimation results of the LA92 test driving cycle at different temperatures

Temperature (°C)	Actual Computational Time (s)			Computational Efficiency (%)	
	LSTM	GRU	CNN	GRU	CNN
-10	425	366	141	13.88	66.82
0	392	388	243	1.03	37.36
10	393	306	218	22.14	44.53
25	456	351	248	23.03	45.61
40	60	56	33	6.67	45

Table 6. 7 Comparison of the accuracy performances of different reports for SOC estimation

Algorithm	Input features & output	Configuration	Battery type/ Temperature (°C)	Accuracy	Research gap	Ref.
UKF	OCV-SOC temperature table used	----	LiFePO4 / 0-50	RMSE= 5	The complex calculation time time-consuming	[104]
ANFIS	OCV and temperatures	ANFIS layers- 5 Epochs= 10	Lithium-ion cells / -30 - 55	MSE =5.6	Computational, interpret problems, time-consuming	[105]
PSO-LSTM	Input = [V, I, T] Output = [SOC]	hidden neurons - 150,400 Epochs - 200,700	LiFePO4 / 25	MAE= 0.3493	More hyperparameter randomness	[106]
LSTM	Input = [V, I, T] Output = [SOC]	hidden layers - 1 hidden neurons -500	LiNiCoAlO2 /0, 10, 25	MAE = 1.606	More hyperparameter randomness	[107]
RNN-GRU	Input = [V, I, T] Output = [SOC]	hidden layers - 2 hidden neurons - 200 Epochs - 500	LiMn2O4 /0.5, 2, 5, 25, 45	MSE = 2.99	Time-consuming, the network structure must be enhanced	[108]
ID-CNN	Input = [V, I, T] Output = [SOC]	Convolution layer - 2 Epoch - 50	Turnigy Graphene -10, 0, 10, 25, 40	RMSE = 0.0043		Present works

In summary, the proposed models, LSTM, GRU, and CNN models, for SOC estimation under varying temperatures using LA92 drive cycle data. The CNN model achieved the best accuracy, an RMSE of 0.0043, and faster computational time than LSTM and GRU. Experimental validation

across $-10\text{ }^{\circ}\text{C}$ to $40\text{ }^{\circ}\text{C}$ confirmed CNN's superior accuracy and robustness, while LSTM performed best at moderate to high temperatures ($25\text{--}40\text{ }^{\circ}\text{C}$) and showed higher error at $-10\text{ }^{\circ}\text{C}$ due to electrochemical limitations. From these case studies, it is evident that CNN-based SOC estimation frameworks outperform LSTMs and GRUs in terms of accuracy, resilience, and efficiency across diverse thermal conditions. These findings strongly support that estimation accuracy deteriorates without condition-awareness and confirm the need for AI-driven models that clearly integrate temperature effects.

6.5 CONCLUSION

This chapter explored how operating and environmental conditions affect battery state estimation and assessed AI-driven approaches in practical electric vehicle situations. The findings indicate that aging stress, temperature fluctuations, and dynamic load patterns significantly influence battery performance and state-estimation precision. In aging conditions, hybrid recurrent machine learning models consistently yielded small estimation errors and high model fitness, whereas CNN-based architectures delivered quicker computations with lower resource requirements. Analysis of temperature across a broad spectrum showed that estimation precision deteriorated under extreme conditions, whereas moderate temperatures facilitated reliable predictions. Among the models evaluated, CNN-based architectures demonstrated consistent performance and computational efficiency across different thermal conditions. The results demonstrate that including operating conditions in AI-based estimation models enhances reliability, adaptability, and real-time usability for advanced BMS in EVs.

CHAPTER 7

CONCLUSIONS, FUTURE SCOPE, AND SOCIETAL IMPACT

7.1 CONCLUSION

This research developed an integrated AI framework for advanced ESSs in EVs by integrating cathode material development, AI-based state estimation, analysis of the impact of environmental conditions, and energy-efficient Green AI strategies. This study addresses key challenges in LIB performance, including degradation behaviour, state-estimate accuracy, environmental variability, and computational efficiency.

The Ni-rich NMC811 layered cathode material was synthesised using the solid-state reaction method. XRD confirmed the formation of a layered hexagonal α -NaFeO₂ structure with an average crystallite size of 22 nm. SEM result indicates that a homogeneous particle shape with an average grain size of ~170 nm has been observed. TGA analysis revealed a total weight loss of 60.84%, confirmed through multistage decomposition. EDS results verified and uniform distribution of elements, a good Ni:Mn:Co stoichiometry. It shows a reliable synthesis route and structural validation framework for high-energy EV cathode materials.

A novel FT has been integrated with an AI framework for SOC and SOE estimation. Hence, 80% dataset size reduction, 79-80% memory consumption, 59-66% computational efficiency, and 61-82% energy consumption have been recorded without losing critical LIBs dynamic information. The FT-CNN-BiLSTM model has shown superior estimation accuracy compared to traditional models for SOC and SOE estimation across different dynamic drive cycles, improving RMSE, MSE, and MAE by up to 99.98%, 99.97%, and 99.96%, respectively. However, FT-GRU model

improved SOH estimation accuracy by over 93% in RMSE and maintained R^2 values above 0.999 across multiple aging datasets. These findings verified the proposed energy efficient AI frameworks for battery health monitoring. This research introduced a Green AI framework for accurate, scalable, and efficient battery state estimation and health monitoring under dynamic conditions.

Analyzed the effect of temperature, dynamic load cycles, and ageing stress on battery performances and estimation accuracy. The validation across $-10\text{ }^{\circ}\text{C}$ to $40\text{ }^{\circ}\text{C}$ confirmed CNN superior accuracy achieved RMSE of 0.0043 and 67% faster computation, while LSTM performed best at moderate to high temperatures ($25\text{--}40\text{ }^{\circ}\text{C}$) and showed higher error at $-10\text{ }^{\circ}\text{C}$ due to electrochemical limitations. From these case studies, it is evident that CNN based SOH and SOC estimation frameworks outperform LSTM and GRU in terms of accuracy, flexibility, and efficiency under diverse thermal conditions. These findings strongly support condition-aware, energy-efficient AI frameworks for the adaptive and reliable BMS operation.

Overall, this thesis present, unified framework that integrates cathode material synthesis, Advance AI models-based modelling, Green AI framework, condition-aware battery modelling, and experimental validations. The proposed methodologies significantly improved state estimation accuracy, energy-efficient, and enhance system reliability under real-time operating conditions. These outcomes a significant contribution to increase battery safety, extending operating lifespan, and boosting the sustainability and performance of LIBs for next generation BMS in electric mobility and grid applications.

7.2 FUTURE SCOPE OF RESEARCH

- Implementing lightweight hybrid DL architectures on embedded hardware platforms would allow for continuous monitoring of SOC, SOE, and SOH under dynamic operating

conditions, enhancing reliability, safety, and operational efficiency in real-world electric vehicle applications.

- The research direction involves pack-level state estimation and fault diagnosis by extending the proposed single-cell models to multi-cell battery packs. Considering cell to cell variations, thermal gradients, and imbalance conditions would enable more accurate health predictions and improve system-level battery safety and lifetime managements.
- Further research might focus on digital twin and online learning frameworks for continuous early detection of thermal runaway events, lithium plating, internal short circuits, and aberrant degradation patterns. These intelligent monitoring frameworks could considerably improve EV safety by allowing for proactive intervention and adaptive control measures.
- Future research may focus on the development of multi-physics coupled AI frameworks that combine electrochemical, thermal, and mechanical degradation processes. Integrating physics-based battery models with data-driven learning approaches can enhance prediction robustness, particularly under extreme operating conditions such as high temperature, fast charging, and variable load profiles.

7.3 SOCIETAL IMPACT

- This research contributes to society by significantly advancing of sustainable electric mobility adaptation and intelligent BMS. By improving battery health monitoring accuracy and reducing computational energy consumption through Green AI techniques, the proposed framework supports longer battery lifespan, reduces electronic waste, and lower lifecycle costs of EVs.

- Enhanced state estimation and condition-aware control strategies also improve operational safety, thereby reducing risks associated with battery failures such as thermal runaway and explosions. It promotes sustainable transportation.
- Furthermore, the integration of energy-efficient AI in BMS promotes environmentally responsible computation, lowering carbon emissions associated with large-scale data processing. The developed methodologies are scalable and applicable to future energy storage technologies, supporting renewable energy integration, smart grids, and next-generation sustainable transportation systems.
- Overall, this research aligns with global goals for clean energy, climate change mitigation, and safe electrification of transportation.

7.3.1 Linking Research Objectives with SDGs for Societal Impact

Figure 7.1 illustrates how the key research objectives of this thesis are aligned with the major United Nations Sustainable Development Goals (SDGs). Objective 1: Synthesis and electrochemical analysis of advanced cathode materials directly contribute to SDG 7: Affordable and clean energy by improving battery energy density, efficiency, and lifetime for EVs. Objective 2: AI-based battery state estimation and health monitoring support SDG 9: Industry, Innovation, and Infrastructure by enabling intelligent, reliable, and data-driven battery management systems. Objective 3: The development of Green AI-based energy-efficient algorithms contributes to SDG 7 and SDG 13: Climate Action by reducing computational energy consumption and minimizing environmental impact.



Figure 7.1 Integration of Sustainable Development Goals with the thesis objectives

Objective 4: condition-aware control strategies under environmental and operating stresses, align with SDG 11: Sustainable Cities and Communities by enhancing EV safety, reliability, and sustainable urban mobility. Collectively, these objectives indirectly support SDG 3: Good Health and Well-being by reducing pollution, preventing battery hazards, and promoting cleaner and safer transportation systems.

REFERENCES

- [1] “Vision 2047 - India’s Roadmap for a Self-Reliant Battery Ecosystem.” Accessed: Mar. 24, 2026. [Online]. Available: <https://indiaesa.info/resources/industry-reports/5014-vision-2047-indias-roadmap-for-a-self-reliant-battery-ecosystem>
- [2] “Lithium-ion battery deployment by application, 2015-2025 – Charts – Data & Statistics - IEA.” Accessed: Feb. 17, 2026. [Online]. Available: <https://www.iea.org/data-and-statistics/charts/lithium-ion-battery-deployment-by-application-2015-2025>
- [3] M. M. Hasan *et al.*, “Advancing energy storage: The future trajectory of lithium-ion battery technologies,” *J. Energy Storage*, vol. 120, p. 116511, Jun. 2025, doi: 10.1016/J.EST.2025.116511.
- [4] A. Satya Veerendra, M. Rusllim Bin Mohamed, F. M. Pedro García arquez, M. Pahang, and C. Arigela Satya Veerendra, “Energy management control strategies for energy storage systems of hybrid electric vehicle: A review,” *Energy Storage*, vol. 6, no. 1, p. e573, Feb. 2024, doi: 10.1002/EST2.573.
- [5] A. M. Bernardes, D. C. R. Espinosa, and J. A. S. Tenório, “Recycling of batteries: a review of current processes and technologies,” *J. Power Sources*, vol. 130, no. 1–2, pp. 291–298, May 2004, doi: 10.1016/J.JPOWSOUR.2003.12.026.
- [6] J. L. Popien, C. Thies, A. Barke, and T. S. Spengler, “Comparative sustainability assessment of lithium-ion, lithium-sulfur, and all-solid-state traction batteries,” *International Journal of Life Cycle Assessment*, vol. 28, no. 4, pp. 462–477, Apr. 2023, doi: 10.1007/S11367-023-02134-4/FIGURES/1.
- [7] M. Mathew, Q. H. Kong, J. McGrory, and M. Fowler, “Simulation of lithium ion battery replacement in a battery pack for application in electric vehicles,” *J. Power Sources*, vol. 349, pp. 94–104, May 2017, doi: 10.1016/J.JPOWSOUR.2017.03.010.
- [8] Z. Tong, J. Miao, S. Tong, and Y. Lu, “Early prediction of remaining useful life for Lithium-ion batteries based on a hybrid machine learning method,” *J. Clean. Prod.*, vol. 317, p. 128265, Oct. 2021, doi: 10.1016/J.JCLEPRO.2021.128265.
- [9] M. Alkhedher, A. B. Al Tahhan, J. Yousaf, M. Ghazal, R. Shahbazian-Yassar, and M. Ramadan, “Electrochemical and thermal modeling of lithium-ion batteries: A review of coupled approaches for improved thermal performance and safety lithium-ion batteries,” *J. Energy Storage*, vol. 86, p. 111172, May 2024, doi: 10.1016/J.EST.2024.111172.
- [10] W. Zhou, Y. Zheng, Z. Pan, and Q. Lu, “Review on the Battery Model and SOC Estimation Method,” *Processes 2021, Vol. 9, Page 1685*, vol. 9, no. 9, p. 1685, Sep. 2021, doi: 10.3390/PR9091685.

- [11] Y. Mazzi, H. Ben Sassi, and F. Errahimi, "Lithium-ion battery state of health estimation using a hybrid model based on a convolutional neural network and bidirectional gated recurrent unit," *Eng. Appl. Artif. Intell.*, vol. 127, p. 107199, Jan. 2024, doi: 10.1016/J.ENGAPPAI.2023.107199.
- [12] A. S. Wijareni, H. Widiyandari, A. Purwanto, A. F. Arif, and M. Z. Mubarak, "Morphology and Particle Size of a Synthesized NMC 811 Cathode Precursor with Mixed Hydroxide Precipitate and Nickel Sulfate as Nickel Sources and Comparison of Their Electrochemical Performances in an NMC 811 Lithium-Ion Battery," *Energies* 2022, *Vol. 15*, Page 5794, vol. 15, no. 16, p. 5794, Aug. 2022, doi: 10.3390/EN15165794.
- [13] M. Colalongo *et al.*, "Operando Investigation of Zr Doping in NMC811 Cathode for High Energy Density Lithium Ion Batteries," *ChemSusChem*, vol. 18, no. 8, p. e202401796, Apr. 2025, doi: 10.1002/CSSC.202401796.
- [14] L. Wu, C. Chen, Z. Li, Z. Chen, and H. Li, "The Joint Estimation of SOC-SOH for Lithium-Ion Batteries Based on BiLSTM-SA," *Electronics* 2025, *Vol. 14*, Page 97, vol. 14, no. 1, p. 97, Dec. 2024, doi: 10.3390/ELECTRONICS14010097.
- [15] P. Dini, A. Colicelli, and S. Saponara, "Review on Modeling and SOC/SOH Estimation of Batteries for Automotive Applications," *Batteries* 2024, *Vol. 10*, Page 34, vol. 10, no. 1, p. 34, Jan. 2024, doi: 10.3390/BATTERIES10010034.
- [16] S. Chavan *et al.*, "Thermal management strategies for lithium-ion batteries in electric vehicles: Fundamentals, recent advances, thermal models, and cooling techniques," *Int. J. Heat Mass Transf.*, vol. 232, p. 125918, Nov. 2024, doi: 10.1016/J.IJHEATMASSTRANSFER.2024.125918.
- [17] C. Huber and R. Kuhn, "Thermal management of batteries for electric vehicles," *Advances in Battery Technologies for Electric Vehicles*, pp. 327–358, Jan. 2015, doi: 10.1016/B978-1-78242-377-5.00013-3.
- [18] R. Schwartz, J. Dodge, N. A. Smith, and O. Etzioni, "Green AI," *Commun. ACM*, vol. 63, no. 12, pp. 54–63, Jul. 2019, doi: 10.1145/3381831.
- [19] J. Xu, W. Zhou, Z. Fu, H. Zhou, and L. Li, "A Survey on Green Deep Learning," Nov. 2021, Accessed: May 13, 2025. [Online]. Available: <https://arxiv.org/pdf/2111.05193>
- [20] Y. Sun, X. Yue, G. Zhuang, Y. Pan, W. Pei, and X. Tang, "Life cycle capacity evaluation for battery energy storage systems," *Electrical Engineering*, pp. 1–11, May 2024, doi: 10.1007/S00202-024-02431-7/TABLES/12.
- [21] W. Koszela, P. Pawlus, R. Reizer, and T. Liskiewicz, "Energy storage technology and its impact in electric vehicle: Current progress and future outlook," *Next Energy*, vol. 6, p. 100202, Jan. 2025, doi: 10.1016/j.triboint.2018.06.034.

- [22] A. Kermansaravi, S. S. Refaat, M. Trabelsi, and H. Vahedi, "AI-based energy management strategies for electric vehicles: Challenges and future directions," *Energy Reports*, vol. 13, pp. 5535–5550, Jun. 2025, doi: 10.1016/J.EGYR.2025.04.053.
- [23] F. Maisel, C. Neef, F. Marscheider-Weidemann, and N. F. Nissen, "A forecast on future raw material demand and recycling potential of lithium-ion batteries in electric vehicles," *Resour. Conserv. Recycl.*, vol. 192, p. 106920, May 2023, doi: 10.1016/j.resconrec.2023.106920.
- [24] O. J. Oladunni, K. Mpofo, and O. A. Olanrewaju, "Advancements, challenges, and prospects of cost-effective electric vehicles: A review," *Alexandria Engineering Journal*, vol. 128, pp. 437–456, Sep. 2025, doi: 10.1016/j.egy.2022.01.123.
- [25] M. V. Reddy, A. Mauger, C. M. Julien, A. Paoletta, and K. Zaghbi, "Brief History of Early Lithium-Battery Development," *Materials 2020, Vol. 13, Page 1884*, vol. 13, no. 8, p. 1884, Apr. 2020, doi: 10.3390/MA13081884.
- [26] R. Martínez-Sánchez, A. Molina-García, A. Mateo-Aroca, and A. P. Ramallo-González, "Evaluating a Nickel–Metal Hydride (NiMH) Battery Regeneration Patent Based on a Non-Intrusive and Unsupervised Prototype," *Batteries 2024, Vol. 10, Page 402*, vol. 10, no. 11, p. 402, Nov. 2024, doi: 10.3390/batteries10110402.
- [27] K. Chayambuka *et al.*, "From Li-Ion Batteries toward Na-Ion Chemistries: Challenges and Opportunities," *Adv. Energy Mater.*, vol. 10, no. 38, p. 2001310, Oct. 2020, doi: 10.1002/aenm.202001310.
- [28] X. Zhang, Z. Li, L. Luo, Y. Fan, and Z. Du, "A review on thermal management of lithium-ion batteries for electric vehicles," *Energy*, vol. 238, p. 121652, Jan. 2022, doi: 10.1016/j.energy.2021.121652.
- [29] R. El Kassar, A. Al Takash, J. Faraj, M. Hammoud, M. Khaled, and H. S. Ramadan, "Recent advances in lithium-ion battery integration with thermal management systems for electric vehicles: A summary review," *J. Energy Storage*, vol. 91, p. 112061, Jun. 2024, doi: 10.1016/J.EST.2024.112061.
- [30] Z. Zhu *et al.*, "Review of integrated thermal management system research for battery electrical vehicles," *J. Energy Storage*, vol. 106, p. 114662, Jan. 2025, doi: 10.1016/J.EST.2024.114662.
- [31] A. I. Kamisan *et al.*, "Recent advances on graphene-based materials as cathode materials in lithium-sulfur batteries," *Int. J. Hydrogen Energy*, vol. 47, no. 13, pp. 8630–8657, Feb. 2022, doi: 10.1016/J.IJHYDENE.2021.12.166.
- [32] Y. Huang *et al.*, "Lithium Manganese Spinel Cathodes for Lithium-Ion Batteries," *Adv. Energy Mater.*, vol. 11, no. 2, p. 2000997, Jan. 2021, doi: 10.1002/aenm.202000997.

- [33] Q. Yang, Z. Yao, C. Lai, and C. Li, “Pre-pulverizing Ni-rich layered oxide cathodes via ‘liquid explosive’ infiltration toward highly durable 4.5 V lithium batteries,” *Energy Storage Mater.*, vol. 50, pp. 819–828, Sep. 2022, doi: 10.1016/J.ENSMS.2022.06.002.
- [34] Y. S. Chen, R. Dominko, M. Marczewski, and W. Wieczorek, “Optimizing high-energy lithium-ion batteries: a review of single crystalline and polycrystalline nickel-rich layered cathode materials: performance, synthesis and modification,” *Appl. Phys. A Mater. Sci. Process.*, vol. 130, no. 10, pp. 1–21, Oct. 2024, doi: 10.1007/S00339-024-07897-7/FIGURES/16.
- [35] Y. Huang, “The discovery of cathode materials for lithium-ion batteries from the view of interdisciplinarity,” *Interdisciplinary Materials*, vol. 1, no. 3, pp. 323–329, Jul. 2022, doi: 10.1002/idm2.12048.
- [36] C. W. Kim, M. H. Lee, W. T. Jeong, and K. S. Lee, “Synthesis of olivine LiFePO₄ cathode materials by mechanical alloying using iron(III) raw material,” *J. Power Sources*, vol. 146, no. 1–2, pp. 534–538, Aug. 2005, doi: 10.1016/j.jpowsour.2005.03.058.
- [37] M. S. Whittingham, “Lithium batteries and cathode materials,” *Chem. Rev.*, vol. 104, no. 10, pp. 4271–4301, Oct. 2004, doi: 10.1021/CR020731C.
- [38] J. Jayaprabakar, J. A. Kumar, J. Parthipan, A. Karthikeyan, M. Anish, and N. Joy, “Review on hybrid electro chemical energy storage techniques for electrical vehicles: Technical insights on design, performance, energy management, operating issues & challenges,” *J. Energy Storage*, vol. 72, p. 108689, Nov. 2023, doi: 10.1016/J.EST.2023.108689.
- [39] A. D. A. Bin Abu Sofian *et al.*, “Nickel-rich nickel–cobalt–manganese and nickel–cobalt–aluminum cathodes in lithium-ion batteries: Pathways for performance optimization,” *J. Clean. Prod.*, vol. 435, p. 140324, Jan. 2024, doi: 10.1016/J.JCLEPRO.2023.140324.
- [40] M. Li, J. Lu, Z. Chen, and K. Amine, “30 Years of Lithium-Ion Batteries,” *Advanced Materials*, vol. 30, no. 33, p. 1800561, Aug. 2018, doi: 10.1002/ADMA.201800561;PAGE:STRING:ARTICLE/CHAPTER.
- [41] Y. Wang *et al.*, “A comprehensive review of battery modeling and state estimation approaches for advanced battery management systems,” *Renewable and Sustainable Energy Reviews*, vol. 131, p. 110015, Oct. 2020, doi: 10.1016/J.RSER.2020.110015.
- [42] T. Raoofi and M. Yildiz, “Comprehensive review of battery state estimation strategies using machine learning for battery Management Systems of Aircraft Propulsion Batteries,” *J. Energy Storage*, vol. 59, p. 106486, Mar. 2023, doi: 10.1016/J.EST.2022.106486.
- [43] S. Nyamathulla and C. Dhanamjayulu, “A review of battery energy storage systems and advanced battery management system for different applications: Challenges and

- recommendations,” *J. Energy Storage*, vol. 86, p. 111179, May 2024, doi: 10.1016/J.EST.2024.111179.
- [44] S. Karmakar, A. K. Bohre, and T. K. Bera, “Recent Advancements in Cell Balancing Techniques of BMS for EVs: A Critical Review,” *IEEE Trans. Ind. Appl.*, vol. 61, no. 2, pp. 3468–3484, 2025, doi: 10.1109/TIA.2025.3531822.
- [45] N. G. Panwar, S. Singh, A. Garg, A. K. Gupta, and L. Gao, “Recent Advancements in Battery Management System for Li-Ion Batteries of Electric Vehicles: Future Role of Digital Twin, Cyber-Physical Systems, Battery Swapping Technology, and Nondestructive Testing,” *Energy Technology*, vol. 9, no. 8, p. 2000984, Aug. 2021, doi: 10.1002/ENTE.202000984.
- [46] M. Waseem, M. Ahmad, A. Parveen, and M. Suhaib, “Battery technologies and functionality of battery management system for EVs: Current status, key challenges, and future perspectives,” *J. Power Sources*, vol. 580, p. 233349, Oct. 2023, doi: 10.1016/J.JPOWSOUR.2023.233349.
- [47] V. Antonucci *et al.*, “Li-ion Battery Modeling and State of Charge Estimation Method Including the Hysteresis Effect,” *Electronics 2019, Vol. 8, Page 1324*, vol. 8, no. 11, p. 1324, Nov. 2019, doi: 10.3390/ELECTRONICS8111324.
- [48] M. A. Hannan *et al.*, “SOC Estimation of Li-ion Batteries with Learning Rate-Optimized Deep Fully Convolutional Network,” *IEEE Trans. Power Electron.*, vol. 36, no. 7, pp. 7349–7353, Jul. 2021, doi: 10.1109/TPEL.2020.3041876.
- [49] R. Swarnkar, H. Ramachandran, S. H. M. Ali, and R. Jabbar, “A Systematic Literature Review of State of Health and State of Charge Estimation Methods for Batteries Used in Electric Vehicle Applications,” *World Electric Vehicle Journal 2023, Vol. 14, Page 247*, vol. 14, no. 9, p. 247, Sep. 2023, doi: 10.3390/WEVJ14090247.
- [50] D. Roman, S. Saxena, V. Robu, M. Pecht, and D. Flynn, “Machine learning pipeline for battery state of health estimation,” *Nat. Mach. Intell.*, vol. 3, no. 5, pp. 447–456, Feb. 2021, doi: 10.1038/s42256-021-00312-3.
- [51] X. Renxin, Y. Yi, J. Xianguang, and P. Nan, “Collaborative estimations of state of energy and maximum available energy of lithium-ion batteries with optimized time windows considering instantaneous energy efficiencies,” *Energy*, vol. 274, p. 127305, Jul. 2023, doi: 10.1016/J.ENERGY.2023.127305.
- [52] L. Chen, Y. Song, A. M. Lopes, X. Bao, Z. Zhang, and Y. Lin, “Joint Estimation of State of Charge and State of Energy of Lithium-Ion Batteries Based on Optimized Bidirectional Gated Recurrent Neural Network,” *IEEE Transactions on Transportation Electrification*, vol. 10, no. 1, pp. 1605–1616, Mar. 2024, doi: 10.1109/TTE.2023.3291501.

- [53] A. Ayob, S. Ansari, M. S. H. Lipu, A. Hussain, and M. H. M. Saad, "SOC, SOH and RUL Estimation for Supercapacitor Management System: Methods, Implementation Factors, Limitations and Future Research Improvements," *Batteries 2022*, Vol. 8, Page 189, vol. 8, no. 10, p. 189, Oct. 2022, doi: 10.3390/BATTERIES8100189.
- [54] S. Ma *et al.*, "Temperature effect and thermal impact in lithium-ion batteries: A review," *Progress in Natural Science: Materials International*, vol. 28, no. 6, pp. 653–666, Dec. 2018, doi: 10.1016/j.pnsc.2018.11.002.
- [55] L. Wu, Z. Lyu, Z. Huang, C. Zhang, and C. Wei, "Physics-based battery SOC estimation methods: Recent advances and future perspectives," *Journal of Energy Chemistry*, vol. 89, pp. 27–40, Feb. 2024, doi: 10.1016/J.JECHEM.2023.09.045.
- [56] C. Weng, J. Sun, and H. Peng, "A unified open-circuit-voltage model of lithium-ion batteries for state-of-charge estimation and state-of-health monitoring," *J. Power Sources*, vol. 258, pp. 228–237, Jul. 2014, doi: 10.1016/J.JPOWSOUR.2014.02.026.
- [57] T. Ouyang, C. Wang, P. Xu, J. Ye, and B. Liu, "Prognostics and health management of lithium-ion batteries based on modeling techniques and Bayesian approaches: A review," *Sustainable Energy Technologies and Assessments*, vol. 55, Feb. 2023, doi: 10.1016/j.seta.2022.102915.
- [58] T. Kim *et al.*, "An On-Board Model-Based Condition Monitoring for Lithium-Ion Batteries," *IEEE Trans. Ind. Appl.*, vol. 55, no. 2, pp. 1835–1843, Mar. 2019, doi: 10.1109/TIA.2018.2881183.
- [59] P. Shrivastava, T. K. Soon, M. Y. I. Bin Idris, and S. Mekhilef, "Overview of model-based online state-of-charge estimation using Kalman filter family for lithium-ion batteries," *Renewable and Sustainable Energy Reviews*, vol. 113, p. 109233, Oct. 2019, doi: 10.1016/J.RSER.2019.06.040.
- [60] K. Khodadadi Sadabadi, P. Ramesh, P. Tulpule, Y. Guezennec, and G. Rizzoni, "Model-based state of health estimation of a lead-acid battery using step-response and emulated in-situ vehicle data," *J. Energy Storage*, vol. 36, p. 102353, Apr. 2021, doi: 10.1016/J.EST.2021.102353.
- [61] K. Laadjal and A. J. Marques Cardoso, "A review of supercapacitors modeling, SoH, and SoE estimation methods: Issues and challenges," *Int. J. Energy Res.*, vol. 45, no. 13, pp. 18424–18440, Oct. 2021, doi: 10.1002/ER.7121.
- [62] K. Y. Liu, T. T. Wang, X. Liu, and H. J. Peng, "Data-Driven Online Prognosis of Rechargeable Batteries: Prospect and Perspective," *Batter. Supercaps*, vol. 7, no. 3, p. e202300596, Mar. 2024, doi: 10.1002/BATT.202300596.

- [63] Z. Song, H. Zhang, and J. Jia, "Data-Driven State of Health Interval Prediction for Lithium-Ion Batteries," *Electronics* 2024, Vol. 13, Page 3991, vol. 13, no. 20, p. 3991, Oct. 2024, doi: 10.3390/ELECTRONICS13203991.
- [64] M. Zhang *et al.*, "A Review of SOH Prediction of Li-Ion Batteries Based on Data-Driven Algorithms," *Energies* 2023, Vol. 16, Page 3167, vol. 16, no. 7, p. 3167, Mar. 2023, doi: 10.3390/EN16073167.
- [65] S. G. Padder *et al.*, "Data-Driven Approaches for Estimation of EV Battery SoC and SoH: A Review," *IEEE Access*, pp. 1–1, 2025, doi: 10.1109/ACCESS.2025.3539528.
- [66] Y. Yin, X. Zhu, and X. Zhao, "A deep reinforcement learning approach for state of charge and state of health estimation in lithium-ion batteries," *AIP Adv.*, vol. 13, no. 10, p. 105207, Oct. 2023, doi: 10.1063/5.0172683/2914691.
- [67] D. N. T. How, M. A. Hannan, M. S. Hossain Lipu, and P. J. Ker, "State of Charge Estimation for Lithium-Ion Batteries Using Model-Based and Data-Driven Methods: A Review," *IEEE Access*, vol. 7, pp. 136116–136136, 2019, doi: 10.1109/ACCESS.2019.2942213.
- [68] X. Li and S. Y. Choe, "State-of-charge (SOC) estimation based on a reduced order electrochemical thermal model and extended Kalman filter," *Proceedings of the American Control Conference*, pp. 1100–1105, 2013, doi: 10.1109/acc.2013.6579983.
- [69] M. Charkhgard and M. Farrokhi, "State-of-charge estimation for lithium-ion batteries using neural networks and EKF," *IEEE Transactions on Industrial Electronics*, vol. 57, no. 12, pp. 4178–4187, Dec. 2010, doi: 10.1109/TIE.2010.2043035.
- [70] A. Moreira, B. Fanzeres, P. Silva, M. Heleno, and A. L. M. Marcato, "On the role of Battery Energy Storage Systems in the day-ahead Contingency-Constrained Unit Commitment problem under renewable penetration," *Electric Power Systems Research*, vol. 235, p. 100147, Oct. 2024, doi: 10.1016/j.epsr.2024.110856.
- [71] D. ; Zhao *et al.*, "Research Progress on Data-Driven Methods for Battery States Estimation of Electric Buses," *World Electric Vehicle Journal* 2023, Vol. 14, Page 145, vol. 14, no. 6, p. 145, Jun. 2023, doi: 10.3390/wevj14060145.
- [72] J. Mou *et al.*, "A data-driven SOE estimation framework for lithium-ion batteries under drive cycle conditions over wide temperature range," *Energy*, vol. 318, no. 8, p. 134658, Mar. 2025, doi: 10.1016/j.energy.2025.134658.
- [73] D. Kumar, M. Rizwan, and A. K. Panwar, "Towards Green AI: A Novel Hybrid Filter Based AI Approach for Energy Efficient State of Charge and Energy Estimation in Li-Ion Batteries under Various Drive Cycles," *IEEE Trans. Ind. Appl.*, pp. 1–12, 2025, doi: 10.1109/TIA.2025.3550108.

- [74] Y. I. Alzoubi and A. Mishra, “Green artificial intelligence initiatives: Potentials and challenges,” *J. Clean. Prod.*, vol. 468, p. 143090, Aug. 2024, doi: 10.1016/J.JCLEPRO.2024.143090.
- [75] Y. Xiong *et al.*, “Artificial intelligence in rechargeable battery: Advancements and prospects,” *Energy Storage Mater.*, vol. 73, p. 103860, Nov. 2024, doi: 10.1016/J.ENSM.2024.103860.
- [76] N. Botteghi, M. Poel, and C. Brune, “Unsupervised Representation Learning in Deep Reinforcement Learning: A Review,” *IEEE Control Syst.*, vol. 45, no. 2, pp. 26–68, 2025, doi: 10.1109/MCS.2025.3534477.
- [77] P. Cheng, Z. Wu, W. Du, H. Zhao, W. Lu, and G. Liu, “Backdoor Attacks and Countermeasures in Natural Language Processing Models: A Comprehensive Security Review,” *IEEE Trans. Neural Netw. Learn. Syst.*, 2025, doi: 10.1109/TNNLS.2025.3540303.
- [78] B. Olivier, F. Guo, Y. Qian, and D. P. Connolly, “A Review of Computer Vision for Railways,” *IEEE Transactions on Intelligent Transportation Systems*, 2025, doi: 10.1109/TITS.2025.3552011.
- [79] X. Han *et al.*, “Multimodal Fusion and Vision-Language Models: A Survey for Robot Vision,” Apr. 2025, Accessed: Jul. 06, 2025. [Online]. Available: <https://arxiv.org/pdf/2504.02477>
- [80] E. Hoque and M. S. Islam, “Natural Language Generation for Visualizations: State of the Art, Challenges and Future Directions,” *Computer Graphics Forum*, vol. 44, no. 1, p. e15266, Feb. 2025, doi: 10.1111/CGF.15266;JOURNAL:JOURNAL:14678659;WGROU:STRING:PUBLICATION.
- [81] H. Wang, J. Song, and X. Li, “A Survey of Electric Vehicles in Sustainable Systems: Environmental Benefits, Pattern Analysis, and AI-Driven Operation Methodologies,” *CHAIN*, vol. 1, no. 3, pp. 177–202, Jan. 2025, doi: 10.23919/CHAIN.2024.000009.
- [82] D. Mirindi, A. Khang, and F. Mirindi, “Artificial Intelligence (AI) and Automation for Driving Green Transportation Systems: A Comprehensive Review,” *Lecture Notes in Intelligent Transportation and Infrastructure*, vol. Part F64, pp. 1–19, 2025, doi: 10.1007/978-3-031-72617-0_1.
- [83] G. Kumar and A. Altalbe, “Artificial intelligence (AI) advancements for transportation security: in-depth insights into electric and aerial vehicle systems,” *Environ. Dev. Sustain.*, pp. 1–51, Apr. 2024, doi: 10.1007/S10668-024-04790-4/TABLES/9.

- [84] R. Schwartz, J. Dodge, N. A. Smith, and O. Etzioni, “Green AI,” *Commun. ACM*, vol. 63, no. 12, pp. 54–63, Jul. 2019, doi: 10.1145/3381831.
- [85] M. Ye, H. Guo, and B. Cao, “A model-based adaptive state of charge estimator for a lithium-ion battery using an improved adaptive particle filter,” *Appl. Energy*, vol. 190, pp. 740–748, Mar. 2017, doi: 10.1016/J.APENERGY.2016.12.133.
- [86] R. Raman, D. Pattnaik, H. H. Lathabai, C. Kumar, K. Govindan, and P. Nedungadi, “Green and sustainable AI research: an integrated thematic and topic modeling analysis,” *J. Big Data*, vol. 11, no. 1, pp. 1–28, Dec. 2024, doi: 10.1186/S40537-024-00920-X/FIGURES/5.
- [87] P. Phogat, S. Dey, and M. Wan, “Powering the sustainable future: a review of emerging battery technologies and their environmental impact,” *RSC Sustainability*, vol. 3, no. 8, pp. 3266–3306, Jul. 2025, doi: 10.1039/D5SU00127G.
- [88] B. Zhang *et al.*, “Lithium-ion battery recycling relieves the threat to material scarcity amid China’s electric vehicle ambitions,” *Nature Communications*, vol. 16, no. 1, pp. 1–15, Dec. 2025, doi: 10.1038/S41467-025-61481-Y;SUBJMETA.
- [89] K. R. Ngoy *et al.*, “Lithium-ion batteries and the future of sustainable energy: A comprehensive review,” *Renewable and Sustainable Energy Reviews*, vol. 223, p. 115971, Nov. 2025, doi: 10.1016/J.RSER.2025.115971.
- [90] S. Ma *et al.*, “Temperature effect and thermal impact in lithium-ion batteries: A review,” *Progress in Natural Science: Materials International*, vol. 28, no. 6, pp. 653–666, Dec. 2018, doi: 10.1016/J.PNSC.2018.11.002.
- [91] F. Leng, C. M. Tan, and M. Pecht, “Effect of Temperature on the Aging rate of Li Ion Battery Operating above Room Temperature,” *Sci. Rep.*, vol. 5, no. 1, pp. 1–12, Aug. 2015, doi: 10.1038/SREP12967;TECHMETA.
- [92] S. Wang *et al.*, “Effects of Current and Ambient Temperature on Thermal Response of Lithium Ion Battery,” *Batteries 2022, Vol. 8, Page 203*, vol. 8, no. 11, p. 203, Nov. 2022, doi: 10.3390/BATTERIES8110203.
- [93] Y. ; ; Wang *et al.*, “Lithium-Ion Batteries under Low-Temperature Environment: Challenges and Prospects,” *Materials 2022, Vol. 15, Page 8166*, vol. 15, no. 22, p. 8166, Nov. 2022, doi: 10.3390/MA15228166.
- [94] M. Schinagl, M. Fasching, P. Höschle, and C. Ellersdorfer, “Impact of temperature on Li-ion battery impedance and compensation strategies,” *J. Power Sources*, vol. 649, p. 237478, Sep. 2025, doi: 10.1016/J.JPOWSOUR.2025.237478.
- [95] A. Geslin, L. Xu, D. Ganapathi, K. Moy, W. C. Chueh, and S. Onori, “Dynamic cycling enhances battery lifetime,” *Nat. Energy*, vol. 10, no. 2, pp. 172–180, Feb. 2025, doi: 10.1038/S41560-024-01675-8;SUBJMETA.

- [96] C. Yang, T. Sun, W. Wang, Y. Li, Y. Zhang, and M. Zha, “Regenerative braking system development and perspectives for electric vehicles: An overview,” *Renewable and Sustainable Energy Reviews*, vol. 198, p. 114389, Jul. 2024, doi: 10.1016/J.RSER.2024.114389.
- [97] H. Faghihian and A. Sargolzaei, “A novel energy-efficient automated regenerative braking system,” *Appl. Energy*, vol. 390, p. 125746, Jul. 2025, doi: 10.1016/J.APENERGY.2025.125746.
- [98] A. Soto, A. Berrueta, M. Mateos, P. Sanchis, and A. Ursúa, “Impact of micro-cycles on the lifetime of lithium-ion batteries: An experimental study,” *J. Energy Storage*, vol. 55, p. 105343, Nov. 2022, doi: 10.1016/J.EST.2022.105343.
- [99] P. Keil and A. Jossen, “Aging of Lithium-Ion Batteries in Electric Vehicles: Impact of Regenerative Braking,” *World Electric Vehicle Journal 2015, Vol. 7, Pages 41-51*, vol. 7, no. 1, pp. 41–51, Mar. 2015, doi: 10.3390/WEVJ7010041.
- [100] X. Han, M. Ouyang, L. Lu, and J. Li, “Cycle Life of Commercial Lithium-Ion Batteries with Lithium Titanium Oxide Anodes in Electric Vehicles,” *Energies 2014, Vol. 7, Pages 4895-4909*, vol. 7, no. 8, pp. 4895–4909, Jul. 2014, doi: 10.3390/EN7084895.
- [101] M. Bercibar, I. Gandiaga, I. Villarreal, N. Omar, J. Van Mierlo, and P. Van Den Bossche, “Critical review of state of health estimation methods of Li-ion batteries for real applications,” *Renewable and Sustainable Energy Reviews*, vol. 56, pp. 572–587, Apr. 2016, doi: 10.1016/J.RSER.2015.11.042.
- [102] E. Chemali, P. J. Kollmeyer, M. Preindl, and A. Emadi, “State-of-charge estimation of Li-ion batteries using deep neural networks: A machine learning approach,” *J. Power Sources*, vol. 400, pp. 242–255, Oct. 2018, doi: 10.1016/J.JPOWSOUR.2018.06.104.
- [103] Y. Tan, Y. Tan, G. Zhao, and G. Zhao, “Transfer learning with long short-term memory network for state-of-health prediction of lithium-ion batteries,” *IEEE Transactions on Industrial Electronics*, vol. 67, no. 10, pp. 8723–8731, Oct. 2020, doi: 10.1109/TIE.2019.2946551.
- [104] K. A. Severson *et al.*, “Data-driven prediction of battery cycle life before capacity degradation,” *Nat. Energy*, vol. 4, no. 5, pp. 383–391, May 2019, doi: 10.1038/S41560-019-0356-8;SUBJMETA.
- [105] J. Zeng, D. Yang, Z. Chen, and F. Tang, “Lightweight deep learning framework for real-time fault diagnosis in EV lithium-ion batteries,” *Journal of Computational Methods in Sciences and Engineering*, Sep. 2025, doi: 10.1177/14727978251380831.

- [106] X. Wang *et al.*, “High-performance LiNi_{0.8}Mn_{0.1}Co_{0.1}O₂ cathode by nanoscale lithium sulfide coating via atomic layer deposition,” *Journal of Energy Chemistry*, vol. 69, pp. 531–540, Jun. 2022, doi: 10.1016/J.JECHEM.2022.02.015.
- [107] E. Laakso *et al.*, “Aging mechanisms of NMC811/Si-Graphite Li-ion batteries,” *J. Power Sources*, vol. 599, p. 234159, Apr. 2024, doi: 10.1016/J.JPOWSOUR.2024.234159.
- [108] J. Qu *et al.*, “Insights into Fast-Charge-Induced Cracking and Bulk Structural Deterioration of Ni-Rich Layered Cathodes for Lithium-Ion Batteries,” *ACS Nano*, vol. 19, no. 37, pp. 33202–33211, Sep. 2025, doi: 10.1021/ACSNANO.5C07347.
- [109] Q. Si, S. Matsuda, Y. Yamaji, T. Momma, and Y. Tateyama, “Data-Driven Cycle Life Prediction of Lithium Metal-Based Rechargeable Battery Based on Discharge/Charge Capacity and Relaxation Features,” *Advanced Science*, vol. 11, no. 33, p. 2402608, Sep. 2024, doi: 10.1002/ADVS.202402608.
- [110] Y. Lecun, Y. Bengio, and G. Hinton, “Deep learning,” *Nature 2015 521:7553*, vol. 521, no. 7553, pp. 436–444, May 2015, doi: 10.1038/nature14539.
- [111] M. Lin, L. Ke, W. Wang, J. Meng, Y. Guan, and J. Wu, “Health prognosis via feature optimization and convolutional neural network for lithium-ion batteries,” *Eng. Appl. Artif. Intell.*, vol. 133, p. 108666, Jul. 2024, doi: 10.1016/J.ENGAPPAI.2024.108666.
- [112] B. Zraibi, C. Okar, H. Chaoui, and M. Mansouri, “Remaining Useful Life Assessment for Lithium-Ion Batteries Using CNN-LSTM-DNN Hybrid Method,” *IEEE Trans. Veh. Technol.*, vol. 70, no. 5, pp. 4252–4261, May 2021, doi: 10.1109/TVT.2021.3071622.
- [113] M. Schuster and K. K. Paliwal, “Bidirectional recurrent neural networks,” *IEEE Transactions on Signal Processing*, vol. 45, no. 11, pp. 2673–2681, 1997, doi: 10.1109/78.650093.
- [114] N. Qi *et al.*, “Machine learning and neural network supported state of health simulation and forecasting model for lithium-ion battery,” *Frontiers in Energy 2023 18:2*, vol. 18, no. 2, pp. 223–240, Nov. 2023, doi: 10.1007/S11708-023-0891-7.
- [115] Z. Cui, R. Ke, Z. Pu, and Y. Wang, “Stacked bidirectional and unidirectional LSTM recurrent neural network for forecasting network-wide traffic state with missing values,” *Transp. Res. Part C Emerg. Technol.*, vol. 118, p. 102674, Sep. 2020, doi: 10.1016/J.TRC.2020.102674.
- [116] D. N. T. How, M. A. Hannan, M. S. H. Lipu, K. S. M. Sahari, P. J. Ker, and K. M. Muttaqi, “State-of-Charge Estimation of Li-Ion Battery in Electric Vehicles: A Deep Neural Network Approach,” *IEEE Trans. Ind. Appl.*, vol. 56, no. 5, pp. 5565–5574, Sep. 2020, doi: 10.1109/TIA.2020.3004294.

- [117] D. Kumar, M. Rizwan, and A. K. Panwar, “Advanced Intelligent Hybrid Approach for State of Charge Estimation of Li-Ion Batteries in Electric Vehicles under Various Drive Cycles,” *2023 IEEE International Conference on Power Electronics, Smart Grid, and Renewable Energy: Power Electronics, Smart Grid, and Renewable Energy for Sustainable Development, PESGRE 2023*, 2023, doi: 10.1109/PESGRE58662.2023.10404810.
- [118] T. Rahman *et al.*, “Deep learning-based battery health prediction for enhancing electric vehicle performance,” *Scientific Reports 2026 16:1*, vol. 16, no. 1, pp. 9871-, Feb. 2026, doi: 10.1038/s41598-026-39911-8.
- [119] X. Liu, Z. Gao, J. Tian, Z. Wei, C. Fang, and P. Wang, “State of Health Estimation for Lithium-ion Batteries Using Voltage Curves Reconstruction by Conditional Generative Adversarial Network,” *IEEE Transactions on Transportation Electrification*, 2024, doi: 10.1109/TTE.2024.3386212.
- [120] J. Lu, R. Xiong, J. Tian, C. Wang, and F. Sun, “Deep learning to estimate lithium-ion battery state of health without additional degradation experiments,” *Nat. Commun.*, vol. 14, no. 1, Dec. 2023, doi: 10.1038/s41467-023-38458-w.
- [121] X. Tang, F. Gao, K. Liu, Q. Liu, and A. M. Foley, “A Balancing Current Ratio Based State-of-Health Estimation Solution for Lithium-Ion Battery Pack,” *IEEE Transactions on Industrial Electronics*, vol. 69, no. 8, pp. 8055–8065, Aug. 2022, doi: 10.1109/TIE.2021.3108715.
- [122] P. De Falco, L. P. Di Noia, and R. Rizzo, “State of Health Prediction of Lithium-Ion Batteries Using Accelerated Degradation Test Data,” *IEEE Trans. Ind. Appl.*, vol. 57, no. 6, pp. 6483–6493, 2021, doi: 10.1109/TIA.2021.3112392.
- [123] Q. Fan, G. He, D. Ruan, and C. Gühmann, “Multi-expert fusion for state-of-health estimation of lithium-ion batteries,” *Scientific Reports 2025 15:1*, vol. 15, no. 1, pp. 42058-, Nov. 2025, doi: 10.1038/s41598-025-26163-1.
- [124] P. Liu, X. Qiu, and H. Xuanjing, “Recurrent Neural Network for Text Classification with Multi-Task Learning,” *IJCAI International Joint Conference on Artificial Intelligence*, vol. 2016-January, pp. 2873–2879, May 2016, Accessed: Feb. 26, 2024. [Online]. Available: <https://arxiv.org/abs/1605.05101v1>
- [125] “NASA Ames Intelligent Systems Division home.” Accessed: Oct. 22, 2023. [Online]. Available: <https://www.nasa.gov/intelligent-systems-division/>
- [126] P. Kollmeyer and M. Skells, “Turnigy Graphene 5000mAh 65C Li-ion Battery Data,” vol. 1, 2020, doi: 10.17632/4FX8CJPRXM.1.
- [127] M. Naguib, P. Kollmeyer, C. Vidal, and A. Emadi, “Accurate surface temperature estimation of lithium-ion batteries using feedforward and recurrent artificial neural networks,” *2021*

- IEEE Transportation Electrification Conference and Expo, ITEC 2021*, pp. 52–57, Jun. 2021, doi: 10.1109/ITEC51675.2021.9490043.
- [128] Z. Ren and C. Du, “A review of machine learning state-of-charge and state-of-health estimation algorithms for lithium-ion batteries,” *Energy Reports*, vol. 9, pp. 2993–3021, Dec. 2023, doi: 10.1016/J.EGYR.2023.01.108.
- [129] Y. Xie, S. Wang, G. Zhang, Y. Fan, C. Fernandez, and F. Blaabjerg, “Optimized multi-hidden layer long short-term memory modeling and suboptimal fading extended Kalman filtering strategies for the synthetic state of charge estimation of lithium-ion batteries,” *Appl. Energy*, vol. 336, p. 120866, Apr. 2023, doi: 10.1016/J.APENERGY.2023.120866.
- [130] L. Jin *et al.*, “A novel hybrid thermal management approach towards high-voltage battery pack for electric vehicles,” *Energy Convers. Manag.*, vol. 247, p. 114676, Nov. 2021, doi: 10.1016/J.ENCONMAN.2021.114676.
- [131] A. M. Divakaran, D. Hamilton, K. N. Manjunatha, and M. Minakshi, “Design, Development and Thermal Analysis of Reusable Li-Ion Battery Module for Future Mobile and Stationary Applications,” *Energies 2020, Vol. 13, Page 1477*, vol. 13, no. 6, p. 1477, Mar. 2020, doi: 10.3390/EN13061477.
- [132] L. Li, C. Wang, S. Yan, and W. Zhao, “A combination state of charge estimation method for ternary polymer lithium battery considering temperature influence,” *J. Power Sources*, vol. 484, p. 229204, Feb. 2021, doi: 10.1016/J.JPOWSOUR.2020.229204.

LIST OF PUBLICATION

- **List of papers (s) published in Peer Reviewed Referred International Journals**

1. D. Kumar, M. Rizwan, and A. K. Panwar, “Towards Green AI: A Novel Hybrid Filter Based AI Approach for Energy-Efficient State of Charge and Energy Estimation in Li-Ion Batteries Under Various Drive Cycles,” *IEEE Trans Ind Appl*, vol. 61, no. 5, pp. 7633–7645, 2025, doi: 10.1109/TIA.2025.3550108. IF- 4.5, (SCIE-Q1)
2. D. Kumar, M. Rizwan, and A. K. Panwar, “Advanced Intelligent approach for state of charge estimation of lithium-ion battery,” *Energy Sources, Part A: Recovery, Utilization, and Environmental Effects*, vol. 45, no. 4, pp. 10661–10681, Oct. 2023, doi: 10.1080/15567036.2023.2249427. IF- 2.4, (SCIE-Q1)
3. D. Kumar, M. Rizwan, and A. K. Panwar, “Recent Advancements, Challenges, and Future Directions of Lithium-Sulfur Battery,” *Ionic*, pp. 1–24, Feb. 2026, doi: 10.1007/s11581-026-06993-3. IF. 2.6 (SCIE-Q2)
4. D. Kumar, M. Rizwan, and A. K. Panwar, “Robust state of health estimation of commercial lithium-ion batteries based on enhanced hybrid machine learning model for electrified transportation,” *Electrical Engineering*, vol. 107, no. 4, pp. 5053–5070, Apr. 2025, <https://doi.org/10.1007/s00202-024-02808-8>. IF- 1.7, (SCIE-Q2)

- **List of Paper(s) Published in Peer Reviewed International Conference**

5. D. Kumar, M. Rizwan, and A. K. Panwar, “Advanced Intelligent Hybrid Approach for State of Charge Estimation of Li-Ion Batteries in Electric Vehicles under Various Drive Cycles,” 2023 IEEE International Conference on Power Electronics, Smart Grid, and Renewable Energy (PESGRE-2023), pp. 1–6, Dec. 2023, doi: 10.1109/PESGRE58662.2023.10404810.
6. M. Rizwan, D. Kumar, and A. K. Panwar, “New Filter-based Supervised Learning Approach for State of Charge Estimation of Li-Ion Battery for EV Applications,” 2023 International Conference on Modeling, Simulation & Intelligent Computing (MoSICom-2023), pp. 213–218, Dec. 2023, doi: 10.1109/MOSICOM59118.2023.10458745.
7. D. Kumar, M. Rizwan, and A. K. Panwar, “A Mini Review on Recent Developments, Limitations, and Future Scenarios of Lithium-Sulfur Battery,” *International Meeting on*

Energy Storage Devices 2023 (IMESD-2023) at Department of Physics, Indian Institute of Technology Roorkee, India during 07-10 December-2023.

8. D. Kumar, M. Rizwan, and A. K. Panwar, "Synthesis, Structural and Electrochemical Analysis of Li-rich NMC Cathode for Lithium-ion Batteries." International Meeting on Energy Storage Devices 2023 (IMESD-2023) at the Department of Physics, Indian Institute of Technology Roorkee, India, during 07-10 December 2023.

- **List of other publications**

9. D. Kumar, M. Ahmed, M. Jamil, M. Rizwan, and A. K. Panwar, "Towards Green AI: Energy-Efficient State of Health Estimation and Degradation Analysis of Commercial Lithium-Ion Batteries Based on Deep Learning and Filter Technique Approach," IEEE Trans Ind Appl, 2025, <https://doi.org/10.1109/TIA.2025.3604739>. IF- 4.5 (SCIE-Q1)
10. D. Kumar, R. Nasimov, A. Singh, A. Jha, A. Jha, and M. Rizwan, "Artificial Intelligence Approaches for SOH Estimation in Lithium-Ion Batteries: A Comprehensive Review of Progress, Critical Evaluations, Challenges, and Toward Future Outlooks," Applied Computational Intelligence and Soft Computing, vol. 2025, no. 1, p. 5516151, Jan. 2025, doi: 10.1155/ACIS/5516151. IF-2.9 (ESCI-Q1)
11. R. Nasimov, D. Kumar et al., "A Novel Approach for State of Health Estimation of Lithium-Ion Batteries Based on Improved PSO Neural Network Model," Processes 2024, vol. 12, no. 9, p. 1806, 2024, doi: 10.3390/PR12091806. IF- 2.8 (SCIE-Q2)
12. D. Kumar, H. Raj, A. Kumar, A. Ranjan, M. Rizwan, and A. K. Panwar, "Novel Hybrid Deep Learning based Framework for Real-Time State of Charge Estimation Considering User-Defined Drive Cycle for Electric Vehicles," IEEE Transactions on Transportation Electrification, 2025 (Under Review)
13. D. Kumar, H. Raj, A. Kumar, M. Rizwan, and A. K. Panwar, "Exploration of Range Estimation and Energy Consumption of Electric Vehicle for Different Real-Time Drive Modes," IEEE Trans Ind Appl, 2025 (Under Review)
14. D. Kumar et. al. "Advancing Electric Vehicle Energy Storage and Management: Standards, Challenges, and Environmental Interactions for Smart Cities and Sustainable Mobility", Sustainable Energy, Grids & Networks, 2025 (Under Review).
15. D. Kumar et. al. "A Novel SSA-CNN-BiLSTM Framework for Accurate State of Health Estimation of Lithium-Ion Batteries", Mathematics, 2025 (Under Review)

16. R. Aman, A. Azeem, D. Kumar, A. Kumar and M. Rizwan, “An IoT Integrated Novel Self-Cleaning Strategy for Enhancing Efficiency of Solar Photovoltaic Modules”, IEEE Transactions on Industrial Informatics, 2025 (Under Review)
17. A. Jha, A. Jha, A. Singh, D. Kumar, M. Rizwan, “EV Battery Thermal Management System Simulation Modelling and Analysis,” 2nd International Conference on Sustainable Power and Energy Research (ICSPER), (11-12, July-2025), (Accepted)
18. D. Kumar, A. K. Ranjan, H. Raj, A. Kumar, M. Rizwan, and S.A. Khan, “A Comprehensive Review on Thermal Runaway in Lithium-Ion Batteries: Triggers, Gas Emissions, and Safety Implications,” 2nd International Conference on Sustainable Power and Energy Research (ICSPER), (11-12- July – 2025), (Accepted)
19. D. Kumar, H. Raj, A. Kumar, A. Ranjan, M. Rizwan, and A. K. Panwar, "Exploration of Range Estimation and Energy Consumption of Electric Vehicle for Different Real-Time Drive Modes," IEEE 5th International Conference on Sustainable Energy and Future Electric Transportation (SEFET), (09-12July-2025)
<https://doi.org/10.1109/SEFET65155.2025.11254979>
20. D. Kumar, H. Raj, A. Kumar, A. Kumar Ranjan, M. Rizwan, and A. K. Panwar, “Robust State of Charge Estimation of Lithium-Ion Batteries Based on Hybrid Deep Learning Approach,” Conference Record - IAS Annual Meeting (IEEE Industry Applications Society), 2025, doi: 10.1109/IAS62731.2025.11061708.
21. M. Ahmed, D. Kumar, and M. Jamil, “Deep Learning Based Modelling for Degradation Analysis and SOH Estimation of Commercial Lithium-Ion Batteries,” Proceedings of the 3rd IEEE International Conference on Power Electronics, Intelligent Control and Energy Systems, (ICPEICES-2024), pp. 1139–1144, 2024, doi: 10.1109/ICPEICES62430.2024.10719198.

LIST OF PATENTS

1. Deepak Kumar, et al. (2025) Design of a Thermal Runaway Chamber for Testing and Investigation of Hazardous Gases and Safety of Li-ion Batteries, Status: Application No. 202611009870
2. Deepak Kumar, et al. (2025) Energy-Efficient State of Health Estimation of Lithium-Ion Batteries Using Green AI and Data Filtering Technique, Status: Application No. 202611050980
3. Deepak Kumar, et al. (2025) Method for Energy-Efficient State of Charge (SOC) and State of Energy (SOE) Estimation of Lithium-Ion Batteries based on Green Artificial Intelligence (Green-AI), Status: Under Examination
4. Deepak Kumar, et al. (2025) Novel and Energy-Efficient IoT-based Self-Dust Cleaning Mechanisms for Solar PV Module, Status: Under Examination

Curriculum Vitae/Brief Profile

Name- Deepak Kumar

Date of Birth:12/07/1994 | **Nationality:** Indian

E-mail: deepakvns163@gmail.com

Mob: +91-9015650051,

[!\[\]\(d9fe643615bb204fb65a4ac8ea28b213_img.jpg\) Google Scholar](#) [!\[\]\(2d4e8336c3a06ac9f0995cb9c0905422_img.jpg\) LinkedIn](#)



About Me

PhD in Electrical Engineering, focused on lithium-ion batteries, degradation mechanism, fast charging, and developed Green-AI/ML/DL-based SOC/SOH/SOE estimation for EV and energy storage applications. PhD-trained researcher with expertise in experimental battery testing/characterization, AI-based data-driven modelling, and safety-focused diagnostics, translating advanced research into industry-ready battery EV/ESS solutions. Strong interest in unsupervised/supervised learning, dynamic data analysis, physics-informed modeling, battery health diagnostics and interdisciplinary battery research.

Education

Program	Department	Institution/Board
Ph.D.	Electrical Engineering	Delhi Technological University, Delhi, India
V. R. F	NSTC-IIPP	Ming Chi University of Technology, Taiwan
M.Tech.	Applied Physics	Delhi Technological University, Delhi, India
	Nano Science & Technology	
M.Tech.	Electrical Engineering	National Institute of Technology Sikkim, India
B.Tech.	Electrical & Electronics Engg.	Dr. A. P. J. Abdul Kalam Technical University, Lucknow, U.P., India

International Research Experience

- ❖ *Presented Research Paper* at the IEEE IAS Annual Meeting, **Hilton Taipei Sinban, Taiwan** *June 15–20, 2025*
- ❖ *Visiting Research Fellow*, **NSTC-IIPP**, Ming Chi University of Technology, Taiwan

July-Sept. 2024

- Designed experimental protocols for lithium-ion cell degradation analysis under varying thermal and electrical stress conditions, and synthesis and characterization of Ni-rich cathode materials.
- Development of green superabsorbent hydrogel nanocomposites with electrical conductivity for environmental remediation and 3D printing.

Technical Skills

❖ *Battery Systems & Ev Energy Storage*

- Lithium-ion batteries (commercial cells)
- Ni-rich NMC-811 cathode material synthesis
- EV battery systems & cell-to-pack fundamentals
- Investigation of fast-charging behaviour
- Battery lifecycle analysis

❖ *AI, ML & Data-Driven Modeling*

- Algorithm validation Machine Learning & Deep Learning
- Hybrid physics–AI models
- Green AI (energy-efficient models)
- Time-series analysis & modeling
- Filter-based learning, model reduction & optimization

❖ *Experimental Testing & Characterization*

- Battery pack tester (Chroma 17020)
- Bidirectional power supply & fast-charging experiments
- Electrochemical & thermal stress testing
- Materials characterization: SEM, XRD, UV–PL

❖ *Safety, Standards & Reliability*

- Thermal runaway analysis
- Battery safety assessment & failure-mode investigation
- Safety guidelines for EV & portable batteries
- Environmental & temperature stress analysis

❖ *Battery State Estimation & Diagnostics*

- Battery states, i.e. SOC, SOH, SOP and SOE
- Battery degradation analysis
- Real-time drive-cycle evaluation
- Temperature-dependent performance analysis
- Degradation mechanisms

❖ *Modeling, Simulation & Analysis*

- Python-based battery modeling
- PyBaMM battery modeling framework
- Numerical & statistical analysis
- Data preprocessing & result interpretation
- MATLAB & Simulink

❖ *Programming & Tools*

- Python, TensorFlow, PyTorch
- SciPy, NumPy, Matplotlib
- MATLAB, OriginLab, Anaconda
- LaTeX, MS Office

❖ *Professional Skills*

- Analytical problem-solving
- Technical documentation
- Teamwork & cross-disciplinary collaboration
- Effective technical communication

Research Articles

1. *D. Kumar*, M. Ahmed, M. Jamil, M. Rizwan, and A. K. Panwar, “Towards Green AI: Energy-

- Efficient State of Health Estimation and Degradation Analysis of Commercial Lithium-Ion Batteries Based on Deep Learning and Filter Technique Approach,” *IEEE Trans Ind Appl*, **2025**, <https://doi.org/10.1109/TIA.2025.3604739>. IF- 4.5, Publisher-IEEE (SCIE-Q1)
2. D. Kumar, M. Rizwan, and A. K. Panwar, “Towards Green AI: A Novel Hybrid Filter Based AI Approach for Energy-Efficient State of Charge and Energy Estimation in Li-Ion Batteries Under Various Drive Cycles,” *IEEE Trans Ind Appl*, vol. 61, no. 5, pp. 7633–7645, **2025**, doi: 10.1109/TIA.2025.3550108. IF- 4.5, Publisher-IEEE (SCIE-Q1)
 3. D. Kumar, M. Rizwan, and A. K. Panwar, “Robust state of health estimation of commercial lithium-ion batteries based on enhanced hybrid machine learning model for electrified transportation,” *Electrical Engineering*, vol. 107, no. 4, pp. 5053–5070, **Apr. 2025**, <https://doi.org/10.1007/s00202-024-02808-8>. IF- 1.7, Publisher-Springer (SCIE-Q2)
 4. D. Kumar, R. Nasimov, A. Singh, A. Jha, A. Jha, and M. Rizwan, “Artificial Intelligence Approaches for SOH Estimation in Lithium-Ion Batteries: A Comprehensive Review of Progress, Critical Evaluations, Challenges, and Toward Future Outlooks,” *Applied Computational Intelligence and Soft Computing*, vol. 2025, no. 1, p. 5516151, Jan. **2025**, doi: 10.1155/ACIS/5516151. IF-2.9, Publisher-Wiley (ESCI-Q1)
 5. V. Sharma, D. Kumar et al., “Advancing photocatalytic efficiency of Mn²⁺-doped ZnSe nanoparticles for sustainable water treatment: removal of toxic organic pollutants,” *Materials Science and Engineering: B*, vol. 321, p. 118542, Nov. **2025**, doi: 10.1016/J.MSEB.2025.118542. IF- 4.6, Publisher-Elsevier (SCIE-Q1)
 6. R. Nasimov, D. Kumar et al., “A Novel Approach for State of Health Estimation of Lithium-Ion Batteries Based on Improved PSO Neural Network Model,” *Processes* **2024**, Vol. 12, Page 1806, vol. 12, no. 9, p. 1806, Aug. **2024**, doi: 10.3390/PR12091806. IF- 2.8, Publisher-MDPI (SCIE-Q2)
 7. D. Kumar, M. Rizwan, and A. K. Panwar, “Advanced Intelligent approach for state of charge estimation of lithium-ion battery,” *Energy Sources, Part A: Recovery, Utilization, and Environmental Effects*, vol. 45, no. 4, pp. 10661–10681, Oct. **2023**, doi: 10.1080/15567036.2023.2249427. IF- 2.4, Publisher-Taylor & Francis (SCIE-Q1)
 8. D. Kumar and M. S. Mehata, “Synthesis of diamagnetic ZnO nano-crystallites via sol-gel method and their photocatalytic activity,” *Indian Journal of Engineering and Materials Sciences*, vol. 29, no. 4, pp. 437–444, Aug. **2022**, doi: 10.56042/IJEMS.V29I4.48695. IF-0.9, Publisher-CSIR-NIScPR (SCIE-Q3)
 9. D. Kumar, M. K. Singh, and M. S. Mehata, “Exploration of grown cobalt-doped zinc oxide nanoparticles and photodegradation of industrial dye,” *Materials Research Bulletin*, vol. 150, Jun. **2022**, doi: 10.1016/J.MATERRESBULL.2022.111795. IF- 5.7, Publisher-Elsevier (SCIE-Q1)
 10. D. Kumar, and S. Dahiya, et al., “A novel eco-friendly MoS₂/PAM composite-based photodegradation of the industrial dye under visible-light irradiation,” *Micro and Nanostructures* 210 (2026) 208466. <https://doi.org/10.1016/J.MICRNAS.2025.208466>. IF-3.0, Publisher-Elsevier (SCIE-Q2)
 11. D. Kumar, M. Rizwan, and A. K. Panwar, “Recent Advancements, Challenges, and Future Directions of Lithium-Sulfur Battery,” *Ionic*, pp. 1–24, Feb. 2026, doi: 10.1007/s11581-026-06993-3. IF-2.6, Publisher-Springer-Nature (SCIE-Q2)
 12. D. Kumar, H. Raj, A. Kumar, A. Ranjan, M. Rizwan, and A. K. Panwar, “Novel Hybrid Deep Learning based Framework for Real-Time State of Charge Estimation Considering User-

- Defined Drive Cycle for Electric Vehicles," *IEEE Transactions on Transportation Electrification*, **2025 (Under Review)**.
13. D. Kumar, H. Raj, A. Kumar, M. Rizwan, and A. K. Panwar, "Exploration of Range Estimation and Energy Consumption of Electric Vehicle for Different Real-Time Drive Modes," *IEEE Trans Ind Appl*, **2025 (Under Review)**.
 14. D. Kumar et. al. "Advancing Electric Vehicle Energy Storage and Management: Standards, Challenges, and Environmental Interactions for Smart Cities and Sustainable Mobility", *Sustainable Energy, Grids and Networks*, **2025 (Revision)**.
 15. D. Kumar et. al. "A Novel SSA-CNN-BiLSTM Framework for Accurate State of Health Estimation of Lithium-Ion Batteries", *Mathematics*, **2025 (Communicated)**.
 16. R. Aman, A. Azeem, D. Kumar, A. Kumar and M. Rizwan, "An IoT Integrated Novel Self-Cleaning Strategy for Enhancing Efficiency of Solar Photovoltaic Modules", *IEEE Transactions on Industrial Informatics*, **2025 (Commun)**.

Conferences (National/International)

1. Amritanshu Jha, Anand Jha, Akshat Singh, D. Kumar, Prof. M. Rizwan, "EV Battery Thermal Management System Simulation Modelling and Analysis," *2nd International Conference on Sustainable Power and Energy Research (ICSPER)*, (11-12- July – **2025**), (**Accepted**).
2. D. Kumar, A. K. Ranjan, H. Raj, A. Kumar, M. Rizwan, and S.A. Khan, "A Comprehensive Review on Thermal Runaway in Lithium-Ion Batteries: Triggers, Gas Emissions, and Safety Implications," *2nd International Conference on Sustainable Power and Energy Research (ICSPER)*, (11-12- July – **2025**), (**Accepted**).
3. D. Kumar, H. Raj, A. Kumar, A. Ranjan, M. Rizwan, and A. K. Panwar, "Exploration of Range Estimation and Energy Consumption of Electric Vehicle for Different Real-Time Drive Modes," *IEEE 5th International Conference on Sustainable Energy and Future Electric Transportation (SEFET)*, (09 - 12 July-**2025**) <https://doi.org/10.1109/SEFET65155.2025.11254979>.
4. D. Kumar, H. Raj, A. Kumar, A. Kumar Ranjan, M. Rizwan, and A. K. Panwar, "Robust State of Charge Estimation of Lithium-Ion Batteries Based on Hybrid Deep Learning Approach," *Conference Record - IAS Annual Meeting (IEEE Industry Applications Society)*, **2025**, doi: 10.1109/IAS62731.2025.11061708.
5. D. Kumar, M. Rizwan, and A. K. Panwar, "Advanced Intelligent Hybrid Approach for State of Charge Estimation of Li-Ion Batteries in Electric Vehicles under Various Drive Cycles," *2023 IEEE International Conference on Power Electronics, Smart Grid, and Renewable Energy (PESGRE-2023)*, pp. 1–6, Dec. 2023, doi: 10.1109/PESGRE58662.2023.10404810.
6. M. Rizwan, D. Kumar, and A. K. Panwar, "New Filter-based Supervised Learning Approach for State of Charge Estimation of Li-Ion Battery for EV Applications," *2023 International Conference on Modeling, Simulation & Intelligent Computing (MoSICom-2023)*, pp. 213–218, Dec. 2023, doi: 10.1109/MOSICOM59118.2023.10458745.
7. M. Ahmed, D. Kumar, and M. Jamil, "Deep Learning Based Modelling for Degradation Analysis and SOH Estimation of Commercial Lithium-Ion Batteries," *Proceedings of the 3rd IEEE International Conference on Power Electronics, Intelligent Control and Energy Systems, (ICPEICES-2024)*, pp. 1139–1144, **2024**, doi: 10.1109/ICPEICES62430.2024.10719198.

8. *D. Kumar*, M. Rizwan, and A. K. Panwar, “A Mini Review on Recent Developments, Limitations, and Future Scenarios of Lithium-Sulfur Battery,” *International Meeting on Energy Storage Devices 2023 (IMESD-2023)* at Department of Physics, Indian Institute of Technology Roorkee, India during 07-10 December-2023.
9. *D. Kumar*, M. Rizwan, and A. K. Panwar, “Synthesis, Structural and Electrochemical Analysis of Li-rich NMC Cathode for Lithium-ion Batteries.” *International Meeting on Energy Storage Devices 2023 (IMESD-2023)* at the Department of Physics, Indian Institute of Technology Roorkee, India, during 07-10 December 2023,

Declaration

I do hereby declare that all the details furnished above are true to the best of my knowledge and belief.

Deepak Kumar